LOCALIZED SURFACE FUNCTIONALIZATION WITH ATMOSPHERIC-

PRESSURE MICROPLASMA JET FOR CELL-ON-A-CHIP APPLICATIONS

A Thesis

Submitted to the Faculty

of

Drexel University

by

Chengyang Wang

in partial fulfillment of the

requirements for the degree of

Ph.D. in Mechanical Engineering

September 2016

DEDICATIONS

To the magnificent universe, with love.

ACKNOWLEGEMENTS

First and foremost, I would like to express my gratitude and appreciation to my research advisor Dr. Wei Sun for his constant guidance throughout the tenure of my PhD research. Dr. Sun is not only a great researcher but also a life-changing teacher to me. I would also like to thank my doctoral advisory committee members Dr. MinJun Kim, Dr. Antonios Kontsos, Dr. Alan Lau, Dr. Hongseok (Moses) Noh, and Dr. Yinghui Zhong for their time and effort to evaluate and improve my dissertation.

I would like to extend my thanks to the wonderful faculty, staff, and students of the Department of Mechanical Engineering and Mechanics for their help during my graduate studies, especially, Kathie Donahue, Dr. Halim Ayan, U Kei Cheang, Steven Leist, Paul Kim, Hoyeon Kim, and Ryan Robinson. My current and past group members, including Dr. Eda Yildirim, Dr. Qudus Hamid, Dr. Jessica Snyder, Yigong Liu, and Mi Thant Mon Soe, have made my journey at Biofabrication Lab exciting and enjoyable. I would also like to thank my colleagues William Brownlowe, Dr. Gayathri Moorthy, and H. Thomas Tucker Jr. at Montgomery County Community College for their support. I have made many good friends during my years in Philadelphia. I always enjoy their friendship and company: Dama Group, The Neighbors, and Zhe Chong Fu, just to name a few of my cliques.

Last but not the least, I am extremely grateful to my parents and my significant other who offered me unconditional love, understanding, and encouragement. Thank you so much for leading me to reach this significant milestone of my life.

CONTENTS

LIST OF TABLES

LIST OF FIGURES

ABSTRACT

**Localized Surface Functionalization with Atmospheric-Pressure
Microplasma Jet for Cell-on-a-chip Applications
Chengyang Wang
Wei Sun, Ph.D.**

Surface properties of biopolymers are crucial for providing topographical and chemical cues to affect cellular behaviors, such as attachment, spreading, viability, proliferation, and differentiation. As an effective surface modification technique, plasma treatment is often applied to enhance surface wettability, adhesion, and biocompatibility of polymers. This study concentrates on developing technical platforms, experimental procedures, and computational-statistical models to manipulate and control the cellular functions on specifically modified polymer surfaces. A novel freeform microplasma-generated maskless surface patterning process was developed to create spatially defined topological and chemical features on biopolymer surface. Global and localized plasma functionalization was performed on polycaprolactone (PCL) samples to introduce biophysical, biochemical, biological and structural cues to enhance cellular response including attachment, proliferation and differentiation. A plasma computational-statistical model was developed to predict the changes in biopolymer surface physicochemical properties following the oxygen based plasma surface functionalization. Furthermore, an integrated system including localized plasma functionalization was specifically designed for the development of biologically inspired devices. The capabilities, benefits, and challenges of the integrated multifunctional biofabrication system to develop cell-on-a-chip device were also

illustrated. The objective of this thesis is to contribute scientific and engineering knowledge to the utilization of plasma chemistry to enhance surface functionalization, development of an engineering model for local plasma treatment, and integration of biofabrication processes to assemble cell-on-a-chip devices.

CHAPTER 1: INTRODUCTION

Part of this work first appeared in [1] and was done in collaboration with Zhenyu Tang, Yu Zhao, Rui Yao, Lingsong Li, and Wei Sun.

1.1   Surface Modification for Fabrication of 3D Cell Model

The US Food and Drug Administration (FDA) has reported that there is a high percentage (92%) of new drug candidates failing between the pre-clinical and clinical development phases [2]. Animals like the Wistar lab rats are candidates utilized in conventional drug investigations. The results from these rats are analyzed warily since rodents' metabolism behaviors to drugs are considerably different compared to human beings. An *in vitro* cell model (human cells) has the potential to be a drug testing platform to investigate absorption, distribution, metabolism, elimination, and toxicity. For example, Shuler et al., developed a microscale *in vitro* system that simulates a human surrogate for drug analysis in which different organs are united in sequence by channels with a fluid circuit inside [3]. Powers et al. conceived a micro-fabricated array bioreactor for a perfused 3D liver culture. This has been used to simulate the *in vivo* environment at certain perfusate flow rates and studies fluid shear stresses. After being cultured for two weeks within the etched channels, the primary (rat) liver cells relocated themselves and then began to form tissue-like structures [4]. This methodology is used to simulate the efficacy of drugs *in vivo*.

2D monolayer was once widely utilized as a useful *in vitro* model because of its feasibility to set up with a relatively good viability in culture. However, 2D

monolayers lack structural architecture. Due to the non-physiological environment, cells become distinct from the original human tissue. E.g. Bissell reported that normal epithelial cells grown in monolayers are highly plastic and show many characteristics as tumor cells [5]. Pampaloni et al. found that primary hepatocytes cultured in 2D environment become undifferentiated after several passages and lose particular functions as synthesis of drug metabolizing enzymes, which are crucial to drug testing [6]. A 3D cell model is a conclusively better platform to simulate a substitute to real tissue. An advantage of 3D cell models, is their regulated microenvironment that mimics geometrical, chemical, and mechanical aspects of real tissues. Moreover, a 3D cell model can be enabled to mimic cell morphology and its environment directly, which can determine the both external cell behavior and internal gene expression [7]. E.g. Mostov et al. showed functional spheres with similar spherical shape, compared to a real tissue that was produced by culturing Mardin-Darby Canine Kidney (MDCK) cells in 3D collagen, while, only undifferentiated monolayers were generated by MDCK cells in 2D generate [8]. Another advantage of 3D cell models is that it can eliminate ethical issues based on animal testing. Various kinds of techniques and devices with the idea of building 3D cell model have been developed, such as; cell culture in 3D hydrogels, cellular spheroids, cultures on microstructured materials, cell-on-a-chip devices, etc. (Figure 1) [9].
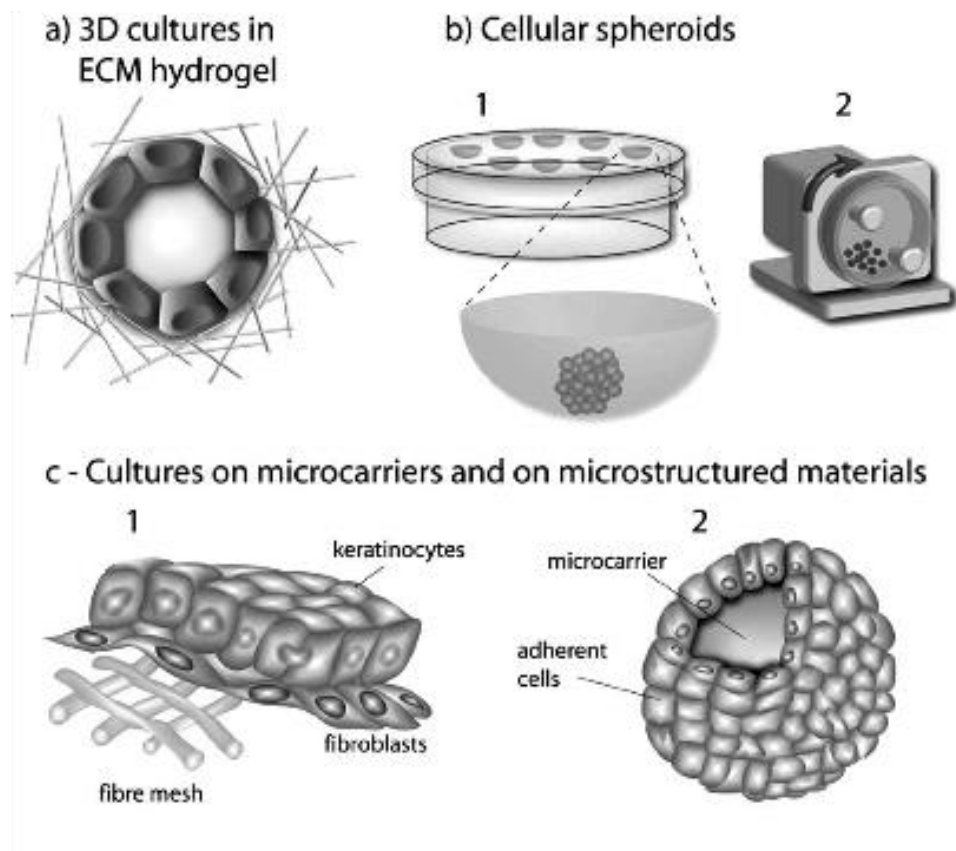
Figure 1. Examples of 3D cell models fabricated with various techniques [9].

Cell-substrate interaction is critical to affect the validity of any cell model. Physical, chemical, and biological modifications of a substrate's surface impacts the quality of cell-substrate interaction in any cell platform. Studies with different cells and polymers have indicated that cellular functions are predictable and controllable through proper surface modifications. Wang et al. have showed that positively charged functional groups incorporated in poly(D,L-lactide) (PDLLA) surface could enhance the interaction between the PDLLA surface and the negatively charged cells [10]. Lee et al. discovered that the existence of an aromatic

ring close to the ionizable group in sodium p-styrene sulphonate (NaSS) attracts more cells onto the plasma surface [11]. Yildirim et al. proved that the increased surface roughness on the biomaterial surface increases the cellular attachment and proliferation [12]. It can be concluded that physicochemical and biological properties of a substrate's surface directly controls critical cellular functions, including but not limited to, attachment, migration, proliferation, differentiation, and apoptosis. Biomaterial functionalization techniques allow physicochemical and biological properties of a biopolymer to be adapted to mimic an *in vivo* microenvironments for cells on an *in vitro* platform, such as a cell-on-a-chip device.

1.2   Plasma Surface Functionalization

Plasma surface modification has been constantly developed to functionalize many biomedical instruments and devices wholly or partly made from biomaterials, including but not limited to, bioactive scaffolds, artificial heart valves, vascular grafts, catheters, stents, membranes for hemodialysis, filters for blood cell separation, and prosthetic devices [13]. There many unique benefits of using plasma treatment for surface modification, compared to other physical, chemical, and photochemical modification techniques. Firstly, the unit of thickness on a plasma-modified surface ranges from ångström to nanometer [14]. Therefore, it is possible to modify the target material's surface uniformly without changing the bulk properties of the material using plasma treatment. Secondly, plasma treatment can avoid the challenges encountered in wet chemical techniques such as residual solvent on the surface, as well as swelling of the substrate [15]. Thirdly, low

temperature and high temperature plasma can be applied to either minimize heat damages or initial drastic reactions respectively, depending on different treating purposes [16].

Free charge carriers in an electrically neutral plasma permit conductivity, which depends on several parameters including the number, the mass, and the collision frequency of the charge carrier, as well as the electron charge. Therefore, it is feasible to control the surface physical properties and chemical functional species on a biopolymer by selecting feeding gases with different chemical elements and compounds. Common feeding gas includes argon, helium, nitrogen, oxygen, fluorine, carbon dioxide, etc. Oxygen-based plasma discharge is often used to modify and functionalize the surface of a biopolymer by introducing oxygen functional groups including hydroxyl (-C-OH), carbonyl (-C=O), carboxyl (-OH-C=O) groups, further to improve cell attachment and promote cellular functions. [17].

1.3　　Engineering Models of Plasma Process

Industrial plasma sources have been developed and researched for a long time, but understanding the fundamental processes for an application like plasma treatment, is generally guided by repetitive testing instead of analytical or computational modeling. Modeling of plasma gas discharges provides researchers with a cost-effective tool to investigate plasma formation mechanisms as well as optimization of process parameters for targeted treatment. As early as 2000, Held

published an analytical model of a dielectric barrier discharge (DBD) cylindrical ozonizer to investigate the optimized ozone concentration as functions of the ozonizer geometry, the electric power, the fluid flow, the temperature and the pressure [18]. Later, Castellanos et al. developed an axial symmetrical plasma chemical and electrical model of a wire-to-cylinder corona discharge to predict ozone concentration [19]. Such developments in this ozone modeling field contribute to the knowledge base of plasma discharge, and eventually lead to the modeling of atmospheric-pressure discharges.

Modeling of atmospheric-pressure discharges depends on several elements: the physical processes, the range of time scales, and the spatial scales. Many models focus either on the discharge formation mechanisms at atmospheric pressure, or on chemical change inside discharge as well as on surfaces. For example, Golubovskii et al. performed numerical calculations of spatio-temporal characteristics, such as the amplitude and frequency of the applied voltage, discharge gap width, and thickness of dielectric barriers by using a one-dimensional fluid model for homogeneous barrier discharge in helium [20]. Yurgelenas and Wagner composed a two-dimensional computational model of dielectric barrier charge for short gaps (1-2 mm) in air to find residual surface charge distribution [21]. A detailed global model of Helium and Water plasmas was reported by Kong et al. to verify Penning processes as the main ionization mechanism [22]. Gas heating was included to shape electric field profiles in a numerical simulation of a DC microplasma discharge in Helium, developed by Donnelly et al. [23]. Much relevant to the topic

of this thesis, He and Zhang explored a one-dimensional radio-frequency fluid plasma model of Helium and Oxygen, to study generation of reactive oxygen species [24]. As mentioned previously, modeling of atmospheric-plasma sources often includes tracing physical processes such as discharge breakdown, fluid dynamics, radical chemistry and surface kinetics occurring over vastly different scales in space and time [25].

1.4   Fabrication of *in vitro* Cancer Models

According to recent reports, cancer(s) in human is becoming a leading cause of death worldwide. This accounts for 7.9 million deaths in 2007, and 12 million deaths in 2030 as estimated [26]. The lack of a thorough understanding of cancer biology is currently a key barrier to investigate the formation, to recognize the invasion, and to track metastasis of malignant tumor [27]. Although much effort has been carried on to cancer-related studies, the long duration of cancer development restricts the feasibility and reproducibility of cancer studies *in situ* [28]. There is an urgent need for *in vitro* cancer models that are sufficient and efficient in mimicking the microenvironment where the cancerous cells reside and the tumor develops. Such *in vitro* cancer models have been proved effective in studying cancer pathogenesis, anti-cancer mechanism and drug testing [29]–[31], as well as in studying cancer development for bladder [30]–[34], breast [5], [35]–[46], kidney [6], [47]–[49], lung [50]–[57], ovarian [58]–[66], pancreatic [67]–[70], and prostate [71]–[82]. On the mechanism side, the use of a 3D cancer model(s) along with microarray technologies could accelerate study on different causes and

modes of cancer cell motility in the metastasis process, as 3D environment resembles *in vivo* situation of cancer cell invasion [83]. Possible mechanism of cell death could also be revealed in an *in vitro* model, particularly to identify the way a cell alters its apoptotic behavior when reacting to exogenous stimuli from matrix microenvironment of surrounding tissue architecture [84]. On the application side, a microscale *in vitro* physiological model was applied to discover cell-drug interactions, to evaluate target organ toxicity arising from exposure to drugs or other external agents, and to study cancer metastasis in disease model [85]. Additionally, application(s) of a cancer model system(s) in biology may help to reduce the use of animal models in many research laboratories and pharmaceutical companies for various drug toxicity testing. A few research groups have noticed and traced the trend of 3D *in vitro* models, from an engineering view [86], [87], an oncology perspective [88], [89], or a mixed approach [90], [91]. These reviews covered different aspects of a 3D cancer model system, such as cell and biomaterial selection [86], [92], culture method selection [87], microenvironment and morphogenesis in 3D model [89], the role of tissue engineering in cancer modeling [90], [91]. This chapter focuses on these reports and discuss some recent developments on a novel 3D *in vitro* cancer model used in cancer studies, along with the modeling design and fabrication techniques and the potential applications to biology, pathogenesis study and drug testing.

Survey on open literatures have shown that most cancer and tumor biological studies are based on two-dimensional (2D) cell models (i.e., 2D

monolayer cell models cultured on tissue culture plates). Traditional 2D biology studies have been proven effective in a certain degree for explaining cancerous cell behaviors and interpreting hypotheses of possible mechanisms. However, the interactions between cells-cells and cells-extracellular matrices in true physiological tissues are difficult to be mimicked by 2D models due to insufficiency on structural, mechanical and biochemical cues. For example, the limit of 2D breast cancer model was that its 2D flat monolayer culture was unable to provide mammary gland stroma, which accounts for over 80% volume of the resting breast volume [93]. In most cases, cells in 3D environment are able to expose to other cells or extracellular matrices, but in 2D model are often limited to expose to fluid, intermediate and flat culture substrate.

Biological studies suggest that cells in a 3D modeling environment may have different behaviors, including cell function [32], differentiation [6], drug metabolism [64], gene expression and protein synthesis [94], morphology [95], proliferation [96], and viability [95].. Early in 1994, Boxberger and Mayer reported that 3D multicellular spheroids induced favorable cell-cell contacts, organized cell pattern, a distinct endoplasmic reticulum, and a marked Golgi apparatus in human bladder carcinoma cell line RT112 cells [32]. At that time the studies focused on feasibility of 3D cell culture, and effects of growth factors on it [97], [98]. With the development of advanced techniques in cell culture and microfabrication field, more results in favor of 3D models were reported. In a comparison study of 3D spheroids vs. monolayers of human hepatoma cell line HepG2, 3D culture not only

increased cellular organization and cell-cell adhesions but also decreased cell apoptosis [95]. It was also discovered that after exposure to the anti-cancer drug paclitaxel, ovarian cancer cell lines (OV-MZ-6 and SKOV-3) survival rates were observed highly increased in cell spheroids grown in 3D hydrogels [64]. In the case of gene expression, oncogenic signals in organotypic neoplasia resembled gene expression profiles of orthotopic *in vivo* model and spontaneous clinical human cancers in 3D tissue, but not in 2D culture [94]. Then from gene to phenotype, Madin-Darby canine kidney (MDCK) cell culture in 3D collagen developed a differentiated polarized epithelium while collagen-coated 2D substrates induced a tumor-like phenotype with increased glycolysis and small up-regulation of proteins [6]. To the contrary, 3D culture of tumor cells usually results in the formation of hollow necrotic cores which recall observations in clinical tumor specimens, as suggested by Ghosh et al [99]. Today, the use of physiologically relevant *in vitro* 3D model system seems to be a trend for its efficient biological resemblance in modern cancer research.

Another approach to studying cancer is to use animal models to replicate the biological and physiological environment of cancer cells. Up to now, most commonly used animal models in drug screening and efficacy study is subcutaneous tumor xenograft, which allows for complex tumor-stromal cell interaction contributing to tumor formation and progression [72]. In this type of model, xenografts are established in immunodeficient mice on which tumor cells are injected beneath the skin [100]. The deficiency of a complete functional

immune system, however, may also affect tumor development [101]. Certain drug tests using xenografts have showed that many promising drugs were found irrelevant to suppressing of spontaneous tumor growth [102]–[104]. Other animal models include chemical carcinogenesis mouse model, radiation carcinogenesis mouse model, and murine genetic mouse model. However, *in vivo* studies by using mouse/animal models are also known for complexities, unpredictability and controversial ethical issues. Also, those animal models are not currently available to all cancer types [105]. For example, Khavari et al. reported a new platform on immune-deficient mice with regenerated human tissue, which could recapitulate many important features of an intact human skin *in vivo* [106]. But this general approach cannot be widely applied to other types of cancers because many visceral tissues do not have tissue regenerative characteristic like skin. In a recent study, Zheng et al. developed a novel orthotopic and metastatic mouse model for gastric cancer with human gastric microenvironment by injecting human gastric cancer cells [107]. Although this model could resemble tumor proliferation and metastases under the manipulated gastric microenvironment, the implanted human gastric tissues were difficult to survive perform normal function in mouse. Here the animal model is still considered insufficient for immune research. It is certain that animal models have contributed to some key aspects of cancer biology, but their inherent xenograft immune characteristics often limit its applicability. It is also arguable that 3D *in vitro* model could fully replace animal model in the future. Currently an animal model still serves as a useful validation benchmark. Still, the techniques in developing a 3D *in vitro* model can often be associated with an animal model [56],

e.g., 3D co-cultured cells introduced in mouse xenografts [108]. Therefore the 3D *in vitro* model is beneficial to cancer research as a fundamental structure, more than merely an evaluation tool.

As previously mentioned, the recreation of tumor microenvironment including tumor-stromal interactions, cell-cell adhesion and cellular signaling is essential in cancer-related studies. Traditional two-dimensional cell culture and animal models have been proven to be valid in some area of explaining cancerous cell behaviors and interpreting hypotheses of possible mechanisms. However, a well-defined *in vitro* cancer model, which mimics tumor structures found *in vivo* and allows cell-cell and cell-matrix interactions, has gained strong interests for a wide variety of diagnostic and therapeutic applications. This section attempts to provide a representative overview of applying *in vitro* biological model systems for cancer related studies. Recent technologies to construct and develop *in vitro* cancer models are summarized in aspects of modeling design, fabrication technique and potential application to biology, pathogenesis study and drug testing. With the help of advanced engineering techniques, the development of a novel cancer cell-on-a chip device as an *in vitro* cancer model will provide a better opportunity to understand crucial cancer mechanisms and to develop new clinical therapies.

1.5   Research Objective and Activities

The objective of this thesis is to develop scientific and engineering knowledge in surface functionalization of substrate surface through global and local

plasma treatment to understand how cellular functions respond to multiple cues from their microenvironment. This thesis presents; the utilization of plasma chemistry to enhance surface functionalization, development of an engineering model for local plasma treatment, integration of biofabrication processes to assemble cell-on-a-chip device.

The specific activities presented in thesis are:

1)   Integration of a dual-function freeform microplasma surface patterning and bioprinting process to produce maskless micro-size patterns and print biomolecules or living cells;

2)   Study of the enhancement of cell attachment, proliferation, and differentiation by modification of the surface properties with microplasma surface treatment;

3)   Development of an engineering model to quantify the degree of surface functionalization generated by microplasma patterning process as a function of key process parameters;

4)   Fabrication and validation of a cell-on-a-chip device for cancer research with an integrated multifunctional biofabrication system

1.6   Thesis Outline

This thesis is outlined as follows:

Chapter 2 discussed the effect of oxygen-based global plasma surface modification of polycaprolactone (PCL) samples on cellular functions. This chapter

illustrated the manufacturing and oxygen-based plasma modification processes of PCL samples. The methods in surface and biological characterization of plasma modified PCL sample were described in details. Changes in surface physicochemical properties by oxygen-based plasma modification improved cell-surface interaction.

Chapter 3 presented an atmospheric-pressure microplasma jet based on dielectric barrier discharge (DBD) was installed on an automated arm of a patented cell printer which allows movement in the x-y-z directions at various trajectory presets. PCL samples were functionalized with helium-oxygen plasma generated by this system and characterized via water contact angle (WCA), X-ray photoelectron spectroscopy (XPS), and scanning electron microscopy (SEM). The surface and biological characterization results indicate that microplasma treatment improved surface hydrophilicity, as well as cell viability and proliferation.

Chapter 4 presented a two-dimensional (2D) plasma simulation-statistical model of the atmospheric-pressure microplasma jet described in Chapter 3. The effect of mass species transport to polymer surface was investigated by coupling an incompressible fluid dynamics model to a plasma kinetics model. The modeling results involve tracking the different physical processes such as discharge breakdown, radical chemistry and surface kinetics occurring at and after ignition of gas discharge.

Chapter 5 investigated the integration of maskless fabrication techniques to develop cell-on-a-chip devices. The integrated multifunctional fabrication system eliminates the limitations of conventional photo-lithography and provides its end-users with the capabilities to develop advantageous cell-on-a-chip, organ-on-a-chip, and body-on-a-chip platforms. This chapter also illustrated the capabilities, benefits, and challenges of the integrated multifunctional biofabrication system to develop biological microfluidics. Several biological investigations were presented to demonstrate the system's capabilities to produce an advanced cancer cell-on-a-chip device.

CHAPTER 2: GLOBAL PLASMA TREATMENT FOR BIOPOLYMER SURFACE MODIFICATION

2.1   Categories of Plasmas

In 1927, Nobel Laureate Irving Langmuir named ionized gas, plasma. Since the later 1920s, numerous efforts have been made to generate, sustain, and utilize this special type of matter (referred to as the fourth state of matter). Plasma have been used in versatile applications, such as lasers, light sources, etching of surfaces, and deposition of chemicals [109]–[113]. Plasma raises countless new challenges in the principles of physics, chemistry, engineering, biology, and medicine. The plasma state of any matter is obtained when gas is excited into energetic states by radio-frequency (RF), microwave (MW) or electrons from a high-temperature filament discharge [16]. Plasma can be categorized into two main groups; high temperature and low temperature (or gas discharge). High temperature plasma specifies that all the species including electrons, ions, and neutral species are in a thermal equilibrium state. Low temperature plasma includes thermal plasma known as quasi-equilibrium plasma, and non-thermal plasma, known as non-equilibrium plasma or cold plasma [112]. Figure 2 shows a typical cold plasma dielectric barrier discharge (DBD). DBD plasma can be generated in various working dielectric mediums through ionization by high frequency and high voltage electric discharges [114]. The existence of dielectric barrier reduced temperature and scales of plasma filaments. DBD plasma is widely used in biological applications for surface functionalization.
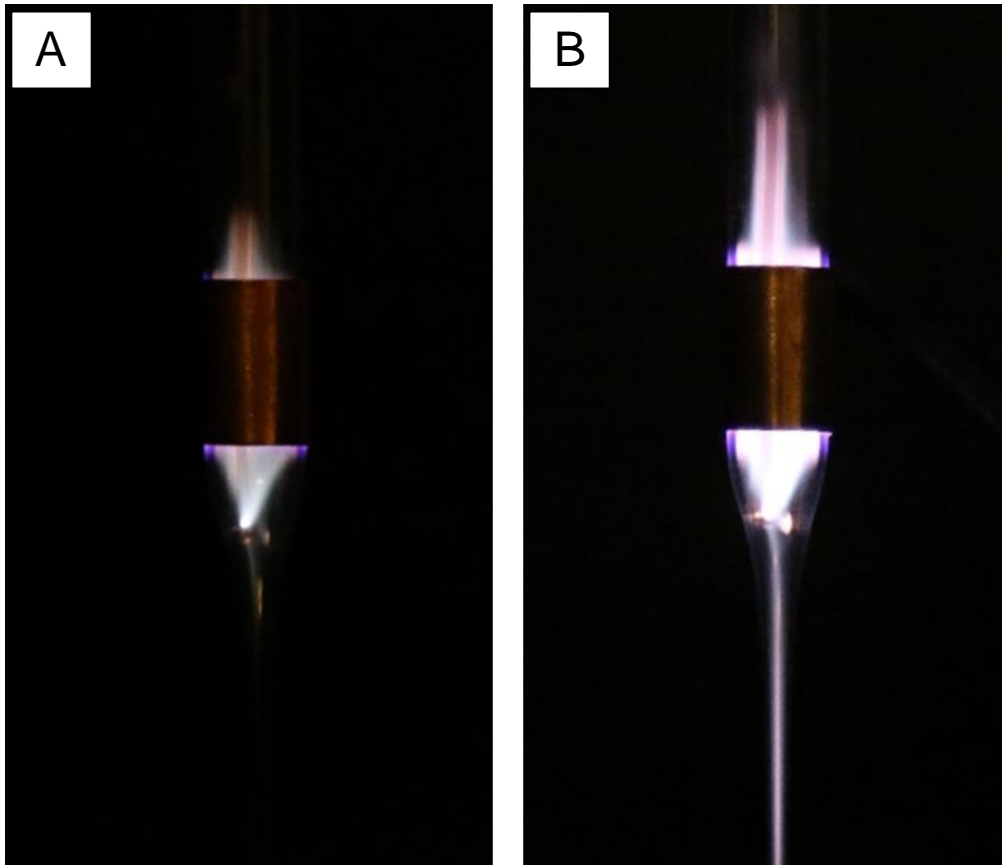
Figure 2. Images of DBD plasma ignition under different process parameters (A: 4kV; B: 6kV).

2.2   Polycaprolactone Sample Preparation

Polycaprolactone (PCL) is a biodegradable thermoplastic polymer widely used in the field of tissue engineering. It has a low melting point of 60 °C and is often used as a feedstock for prototyping systems. PCL was approved and regulated by the U.S. Food and Drug Administration (FDA). It is frequently investigated as a scaffold material for use in bone regeneration due to its biocompatibility.

A glass mold was manufactured to fabricate the PCL samples for experimental use. The height of the empty mold space is 0.75 mm. The glass mold

base was first placed on a hotplate and preheated up to 100 °C. A batch of PCL (Sigma-Aldrich, St. Louis, MO) beads was then distributed at designated spots on the glass mold base. After the PCL beads were fully melted, a new batch of beads was added. The final step was repeated until a total of four batches of beads were melted. A glass cover was placed over the glass mold base, both ends clipped subsequently. The set was removed from the hotplate and passively cooled to room temperature. The PCL samples were collected after the glass cover was removed. Each fabricated PCL sample had a smooth surface with a diameter of 12.5 mm and a thickness of 0.75 mm, allowing it to fit 24-well cell culture plates for the use of future biology studies (Figure 3). At the preparation stage, two cuts were made at the edges on each PCL sample to indicate its centerline. The PCL samples were rinsed in 95% alcohol for 30 minutes. They were collected and later placed under microplasma nozzle for plasma treatment (Figure 4).
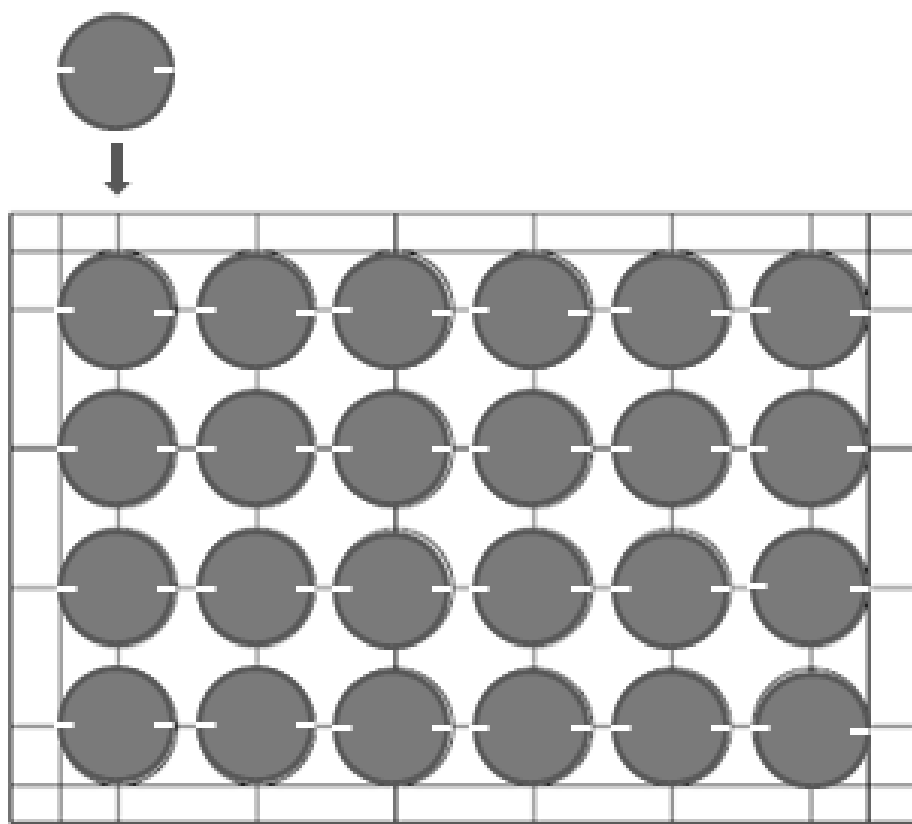
Figure 3. Preparation of PCL samples in a 24-well cell culture plates for plasma treatment.

Figure 4. Fabricated PCL samples stored in a petri dish.

2.3   Plasma Surface Modification and Characterization

To investigate the effects of global plasma modification, sterile polycaprolactone (PCL) samples were modified with a plasma reactor (PDC 32G, Harrick Plasma, New York). The plasma reactor consists of radio-frenquency (RF 13.56 MHz) powered coils around the shell of plasma chamber with gas feeding inlet and vacuum pumping outlet. The PCL samples were placed in the plasma chamber and oxygen (O2) was purged to the chamber at flow rate of 1 slpm by an integrated gas feeding system. During the global plasma treatment, the plasma chamber was maintained at a low pressure (~200 mTorr) through vacuum pump

with a pumping speed of 6 m^3/hr. Generally a 100 W of RF power was applied to create high-frequency magnetic field to breakdown the gas and sustain the plasma. The plasma generated modified the PCL sample surface globally therefore a uniformly can be expected. After the plasma modification, the samples were transferred to a laminar air flow biological safety cabinet for further characterizations.

The corresponding contact angles were measured to evaluate the effect of the applied global plasma surface modification techniques. This study quantifies PCL's degree of hydrophilicty and surface wettability. The water contact angle (WCA) of probe liquids on modified and unmodified PCL sample surfaces were measured by a sessile drop technique. In this technique, once the probe liquid is dropped to the surface, the image of the droplet is taken using a video-camera mounted on a microscope. Ultrapure water was provided from Agilent Technologies (Germany). Before starting contact angle measurement, a drop of probe liquid (2µL) was placed on modified and unmodified PCL sample surfaces at room temperature. Once the liquid had settled (become sessile), droplet images were taken then transferred to ImageJ software (NIH, Bethesda, Maryland). Figure 5 shows a plugin in ImageJ for measuring the actual contact angles [115].
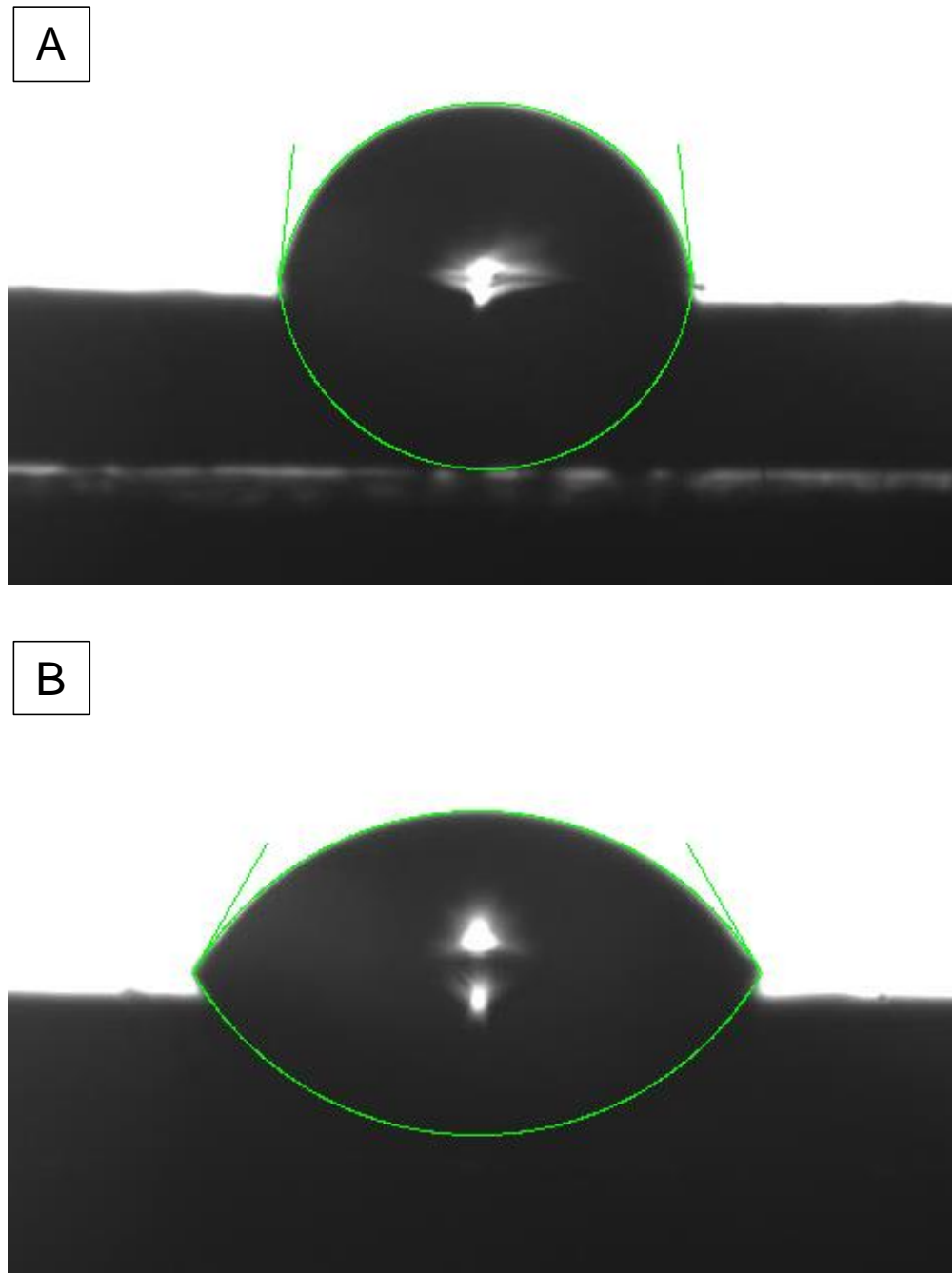
Figure 5. Drop shape analyses using ImageJ with contact angle measurement plugin (A: drop on native PCL sample; B: drop on plasma-treated PCL sample).

The effect of plasma modification on surface hydrophilicity was measured by the contact angle on unmodified and plasma modified PCL surfaces, and the

results are shown in Figure 6. After fabrication, the contact angles of the native PCL samples were around 80°. The results of the contact angle measurement indicated showed that the contact angles decreased significantly after the plasma modification, which means that the surface hydrophilicity increases as a result of the plasma surface treatment.
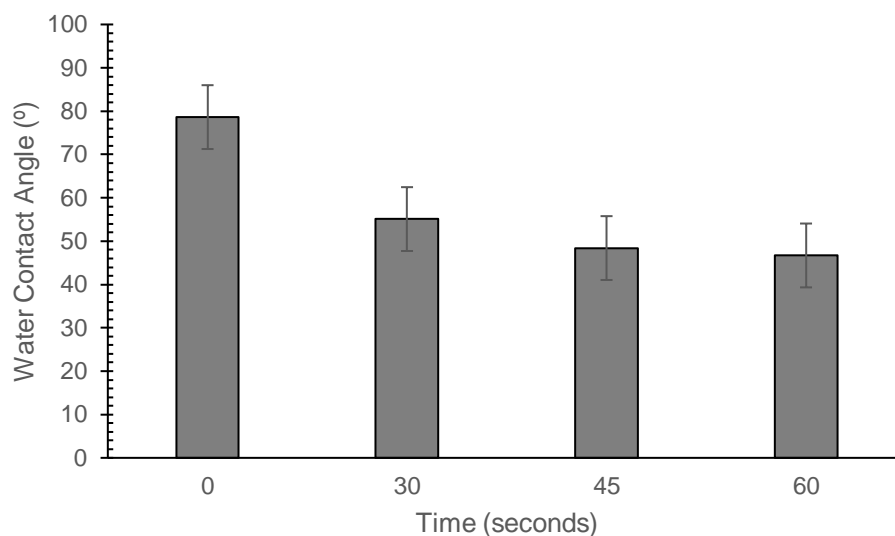
Figure 6. Effect of changing plasma treatment time on WCA for PCL (sample size: n=3).

2.4   Biological Investigations

7F2 cells are acquired from American Type Culture Collection (ATCC, Manassas, VA). The cells were cultured in 90% alpha minimum essential medium with 2 mM l-glutamine and 1 mM sodium pyruvate (Sigma-Aldrich, St. Louis, MO), and with 10% fetal bovine serum (Gibco, Grand Island, NY). Cells were maintained in incubator equilibrated with 5% carbon dioxide (CO_2) at 37 °C. At confluency, cells were trypsinized, counted and re-suspended to a cell density of

1×106 cells/mL. Culture medium was changed every 2 to 3 days. The cell-polymer constructs were maintained in an incubator (37°C and 5% CO2) for further analysis.

A MarkerGene™ Live:Dead/Cytoxicity assay kit was used to analyze the cell viability and cytotoxicity. A Live:Dead solution was created using propidium iodide with carboxyfluorescein diacetate according to the manufacturer's protocols. The damaged cells were marked fluorescently red and the intact cells were marked green by carboxyfluorescein dye. Red fluorescence could be observed with excitation and emission at 493 nm and 630 nm, respectively. Green fluorescence could be observed with excitation and emission at 475 nm and 517 nm, respectively. Figure 7 shows a comparison of Live:Dead fluorescent images of 7F2 cells attached to treated and native PCL samples. An alamarBlue® Kit (AbD Serotec, Raleigh, NC) was used to determine cell proliferation rates. The excitation and emission wavelengths for alamarBlue® assay were 535 and 590 nm, respectively. Quantitative data for cell viability and proliferation were collected using the microplate reader (GENios, Tecan Systems, San Jose, CA).
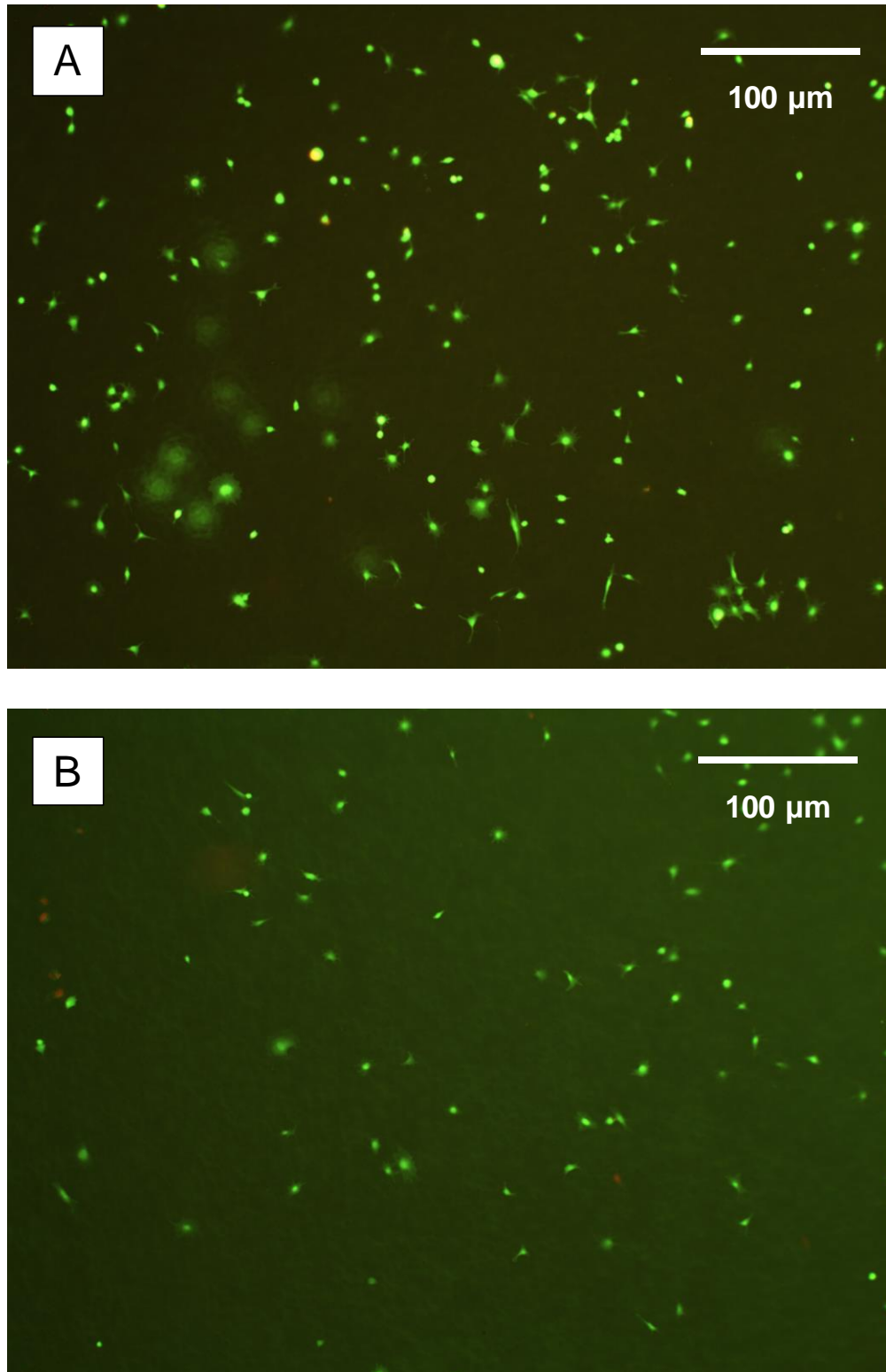
Figure 7. Live:Dead fluorescent images of 7F2 cells attached to (A) plasma-treated and (B) control PCL samples.

The studies of cellular response aim to identify the effects of a microplasma-functionalized area on cell activities including attachment, proliferation, and differentiation. After being plasma treated for 1 minute, the functionalized area of the biopolymer was seeded with cells. AlamarBlue® assay, which incorporates a fluorometric indicator directly based on proportional relationship between fluorescence intensity and cell viability, was used to quantify cell proliferation. Live:Dead assay was used to measure the metabolic activity of cells. The 7F2 cells were later seeded on both treated and native PCL samples following standard cell culture protocol described previously. Figure 8 shows that the microplasma treatment improved both cell viability and proliferation at 6 hour, 12 hour, 18 hour, and 24 hour time points (n = 3). The peak of fluorescence intensity for both plasma treated and control group appears at 24 hour time point.
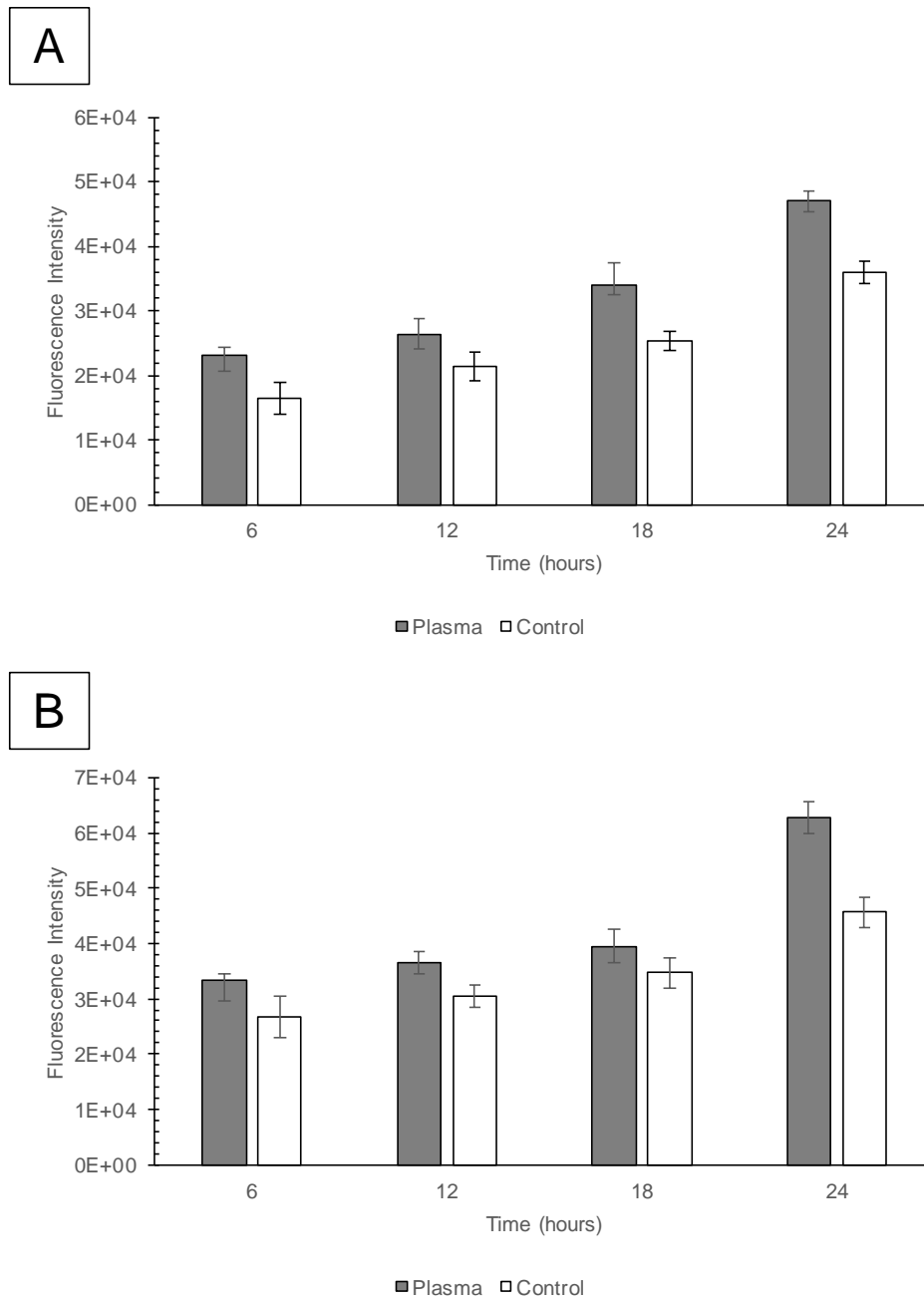
Figure 8. 7F2 cell viability and proliferation on PCL samples (A: cell viability results from Live:Dead assays; B: cell proliferation results from alamarBlue® assays; sample size: n=3).

CHAPTER 3: DEVELOPMENT OF A LOCALIZED FREEFORM MASKLESS MICROPLASMA PATTERNING SYSTEM

This work first appeared in [116] *and was done in collaboration with Qudus Hamid, Jessica Snyder, Halim Ayan, and Wei Sun.*

3.1   Surface Treatment Techniques

The ability to manipulate structural and biochemical cues plays an important role in regulating cell behavior during the biofabrication process for a wide range of diagnostic and therapeutic applications [117], [118]. In a living tissue environment, cells and proteins are surrounded by topographic and biochemical cues, which assist with cell attachment and provide guidance for cell-cell and cell-substrate interactions [119], [120]. In nature, these cues are inherent to the native biological system [121], [122]. However, most biopolymers that are currently utilized in tissue engineering often lack adequate surface structural or biochemical cues. To enhance the surface functionality of biopolymers, a variety of techniques have been used. For example, conventional photolithography [123]–[129], soft lithography [130], [131], microcontact printing [132], [133], self-assembled monolayers (SAMs) [134]–[136], direct writing [137], and laser ablation [138]. These surface treatment techniques can provide additional structural, chemical, and biological cues that regulate cell morphologies as well as subsequent cellular function [139]–[141]. In most of the aforementioned techniques, surface functionalization is achieved by applying cell-adhesive and cell-repellant biomolecules to the surface through patterned masks or master stamps. Though effective, the preparation of patterned masks and/or master stamps is often a costly

process in terms of both time and resources (e.g., the need to use special clean room instrumentation) [142]–[145]. The harsh chemicals and solvents used in these processes can damage the patterned bio-organic layers [145], [146]. Additionally, the use of patterned masks or master stamps is very difficult to achieve a controlled surface gradient, especially on surfaces with complex geometries [147], [148].

Due to these limitations, maskless plasma-based surface treatment has recently gained considerable interest [149]–[154]. Assisted plasma polymerization and coating could benefit photolithographic processes in fabricating biosensors [155]. Plasma-induced biopolymer surface functionalization has been reported to improve the biocompatibility of biomaterials for nerve repair by enhancing cellular responses [156]. Microplasma discharges technologies (miniaturization of the plasma down to characteristic micro feature size) have a broad range of applications in display panels [157], materials processing [158], [159], analytical instruments [160], decontamination of living human tissue [161], [162], and "plasma needles" for surgery [163], [164]. Though versatile and efficient, most enabling plasma technologies use "hot" plasma dischargers and operate under low pressure (below atmospheric pressure), which makes them a difficult tool for treatment of heat-sensitive biopolymers and biological substrates. Additionally, conventional plasma needle discharges are on the order of millimeters in size [163]–[165] and are incapable of producing the micro-scale surface patterning suitable to cell and biomolecule patterns. This chapter presents a localized atmospheric-pressure and non-thermal microplasma surface functionalization technique to produce maskless

and chemical-free (non-hazardous) surface patterning. The freeform microplasma surface patterning process is able to produce the desired structural and chemical cues simultaneously to enhance the surface properties of biopolymers for tissue engineering applications.

3.2   Freeform Maskless Microplasma System

DBDs are non-equilibrium plasma that operates under atmospheric pressure [166]. Due to a non-equilibrium nature, DBD plasmas can generate high energy electrons at cool background gas temperatures (heavy particles). This unique character (selective high electron temperature, and low background temperature) enables a rich plasma chemistry in many plasma chemical processes [167].

In this chapter, an employed microplasma was generated by a variable frequency power supply with the DBD technique. The microplasma system is integrated with a freeform fabrication-based biomolecule printing system to perform the dual functions of freeform generation of microplasma surface patterns and printing biomolecules and cells. The microplasma first functionalizes the biopolymer surface based on the designed pattern and then bioprinting system prints cells or biomolecules on the generated pattern surfaces.

The plasma electrode system is composed of a high voltage metal electrode (copper, 1 mm in diameter) coaxially inserted in a dielectric tube (borosilicate glass, 6.5 mm in outer diameter, 0.2 mm in thickness), with a ground metal electrode

(copper, 0.4 mm in thickness) wrapped around the tube from the outside. The process gas (or gas mixture) is purged through the annular gap between the coaxial electrode and the dielectric tube. When the high voltage electrode is powered, plasma ignited between the electrodes and a micron-scale plasma appears at the tip of the nozzle. Once the microplasma contacts the surface of the biopolymer, it changes the topography and chemistry of the plasma-exposed area. The voltage and current data were acquired through a 100MHz digital oscilloscope (Tektronix TDS2014C, Tektronix Inc., Beaverton, OR) with a $1000\times$ high voltage probe (Tektronix P6015A, Tektronix Inc., Beaverton, OR) and a 1 V/A current monitor (Pearson 4100, Pearson Electronics Inc., Palo Alto, CA). Figure 9 shows a schematic view of the microplasma system and its components. Depending on the microplasma operation parameters such as plasma power, gas flowrate, gas composition, and nozzle tip diameter, a certain level of control on the chemical composition and topological features of the biopolymer surface can be obtained (Figure 10).
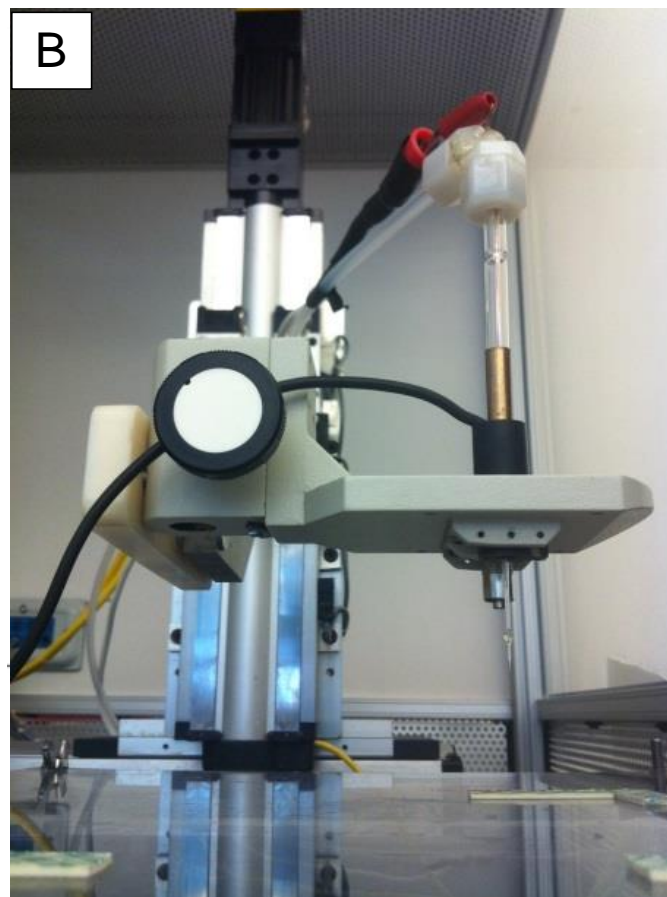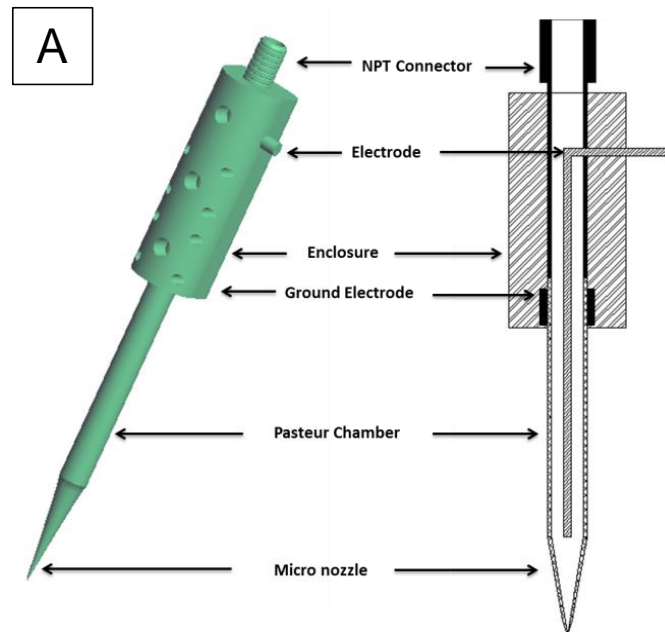
Figure 9 Structure of microplasma jet. (A: schematic; B: photography).
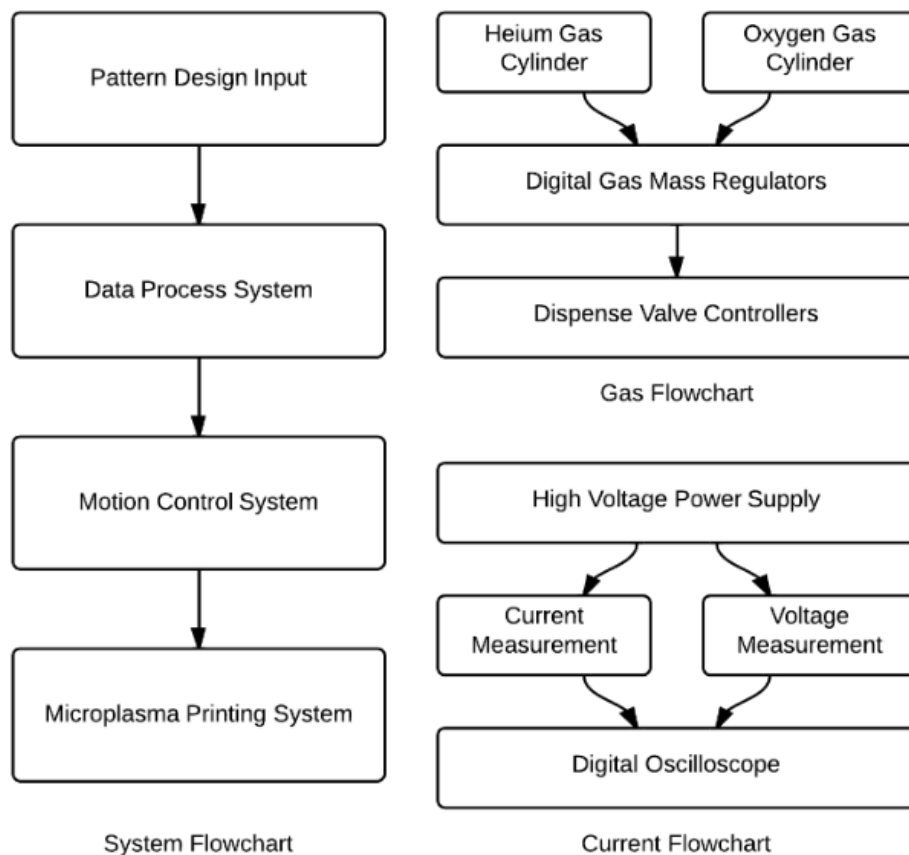
Figure 10. The flow chart of the microplasma system.

The micro-scale plasma nozzle tips were manufactured using a P-2000 Micropipette Puller following a preset of parameters for repeatability. Micro-nozzle tips with inner diameters at the tip ranging from 50 µm to 500 µm were fabricated and latter connected to the borosilicate glass Pasteur pipettes; the joints were sealed by light cure adhesive (Loctite 35241 352, Henkel Corp., Rocky Hill, CT). Two microscopic images are presented in Figure 11 to demonstrate various sized plasma

nozzle tips. It should be noted that the cracks around the nozzle tip are common and is due to the manufacturing process of pulling.
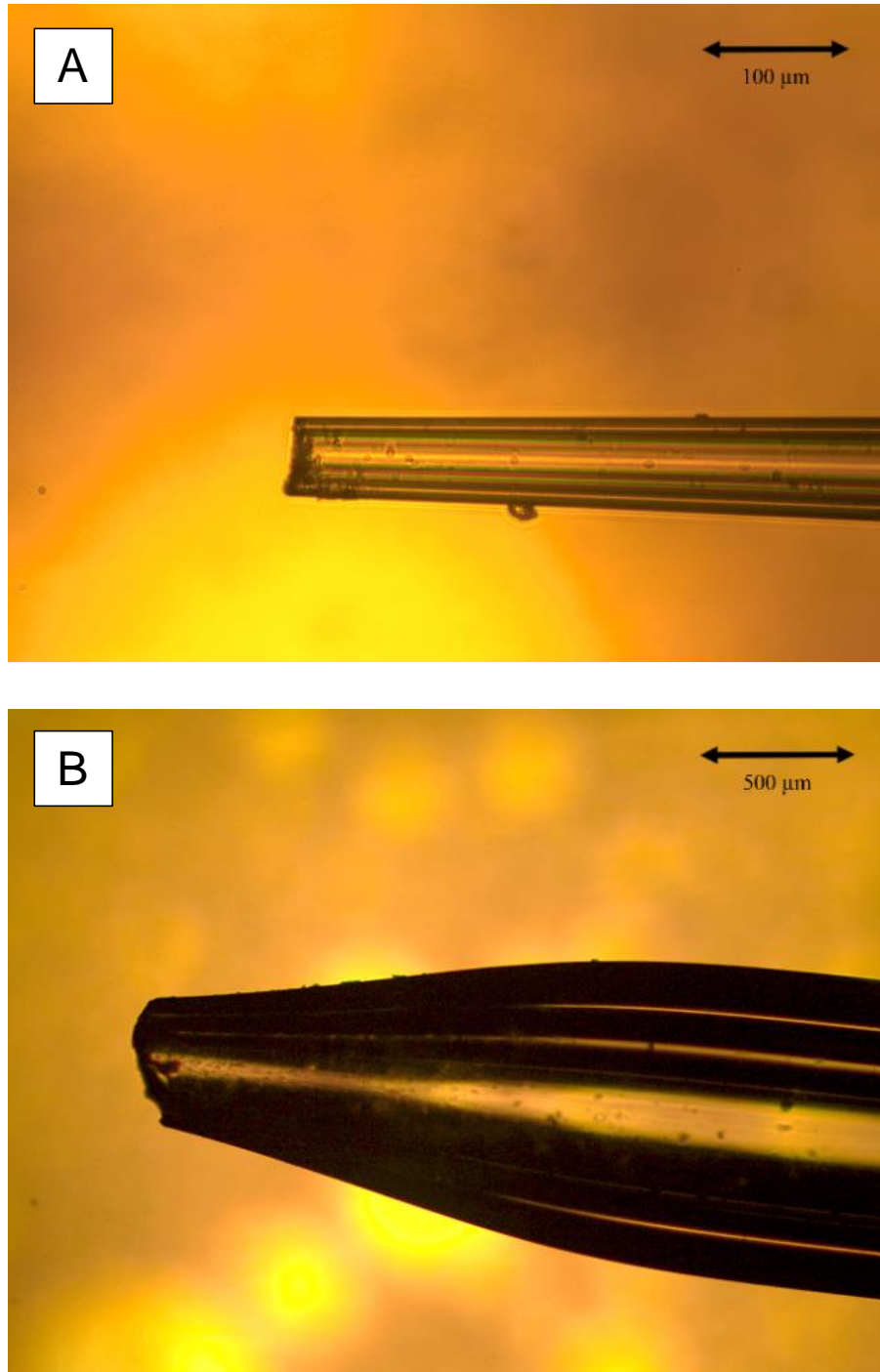
Figure 11. Microscopic images of plasma nozzle tips with different nozzle diameters (A: 50 µm; B: 250 µm).

In order to create a pattern and control the shape of the pattern over the biopolymer surface, the microplasma system is operated by a data processing and motion control system. The data processing system converts the CAD model or designed pattern into a layered process tool path. The 3D motion system consists of x-, y-, and z-axes, which were actuated by AC servo motors driven by servo drivers (Parker Hannifin Corp, Cleveland, OH). Through the data processing and 3D motion system, users are able to define the path for the microplasma nozzle such that it follows the path of the surface patterning without using any mask or master stamps.

To study the effect of gas composition on surface change, oxygen (O_2) is required to produce active oxygen species for the functionalization of the biopolymer surface. However, oxygen is a highly electronegative gas and causes excessive attachment and eventually quenching of the discharge if it is not accompanied by another gas that can sustain stable non-thermal plasma, such as helium (He). Figure 12 shows the effect of changing gas composition on the appearance of microplasma discharge. Other tunable parameters includes; voltage, frequency, traveling speed, nozzle size, and displacement from nozzle tip to sample surface. A line/curve pattern of plasma treatment on each sample can be performed via the automation platform following a set of predefined working parameters (Table 1). The microplasma jet operates at room temperature (~300K). At higher power settings arcing would occur (temperature would increase).
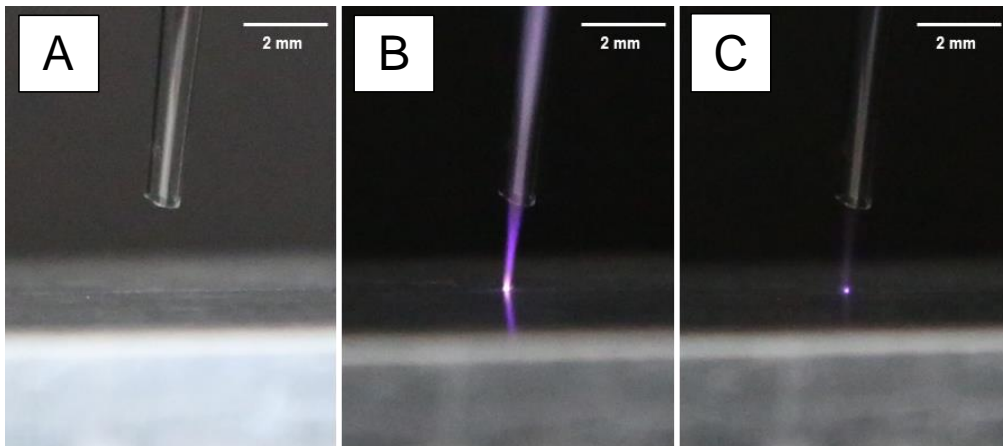
Figure 12. Photographs of microplasma jet (A: no discharge; B: discharge from 100% helium; C: discharge from 99% helium.and 1% oxygen; exposure time: 12.5 ms).

Table 1. Typical working parameters for microplasma surface functionalization.

Working Parameters	Value	Unit
Voltage	3	kV
Frequency	20	kHz
Helium flowrate	0.5	slpm
Oxygen flowrate	5	sccm
Traveling speed	0.5	mm/s
Nozzle size	150	μm
Distance from nozzle tip to sample surface	1	mm

Two separate voltage-current waveforms of the microplasma discharge (operating in the helium/oxygen gas mixture) demonstrating the plasma system's capabilities are shown in Figure 13. The voltage is 6 kV peak-peak with frequency

set to be 25 kHz. The numerous current spikes in every half cycle of the voltage waveform, represent microdischarges occurring in the atmospheric microplasma jet.
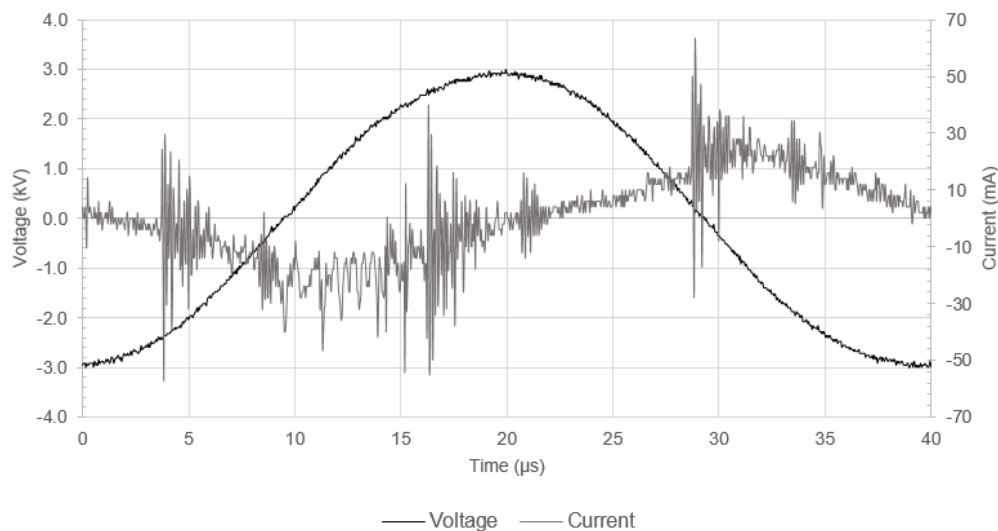
Figure 13. Voltage-Current waveforms of microplasma discharges in helium-oxygen gas mixture (1% O2, 99% He) with voltage of 6 kV peak to peak.

3.3   Surface Modification of Polycaprolactone

PCL samples were fabricated following the same procedures detailed in section 2.2. To analyze the modifications on a microplasma patterned surface, water contact angle (WCA) and X-ray photoelectron spectroscopy (XPS) served as quantitative methods; the study of surface topography using scanning electron microscopy (SEM) and atomic force microscopy (AFM) as qualitative methods provides more intuitive results. WCA images were captured via a Basler A601f camera (Basler Vision Technologies, Exton, PA) and a Fiber-Lite MI-150 light source (Dolan-Jenner Industries, Boxborough, MA). XPS data were acquired using

VersaProbe 5000 (Physical Electronics, Chanhassen, MN) with a monochromatic Al Kα X-ray source. SEM images were obtained using an FEI/Philips XL-30 Field Emission Environmental Scanning Electron Microscope (FEI, Hillsboro, OR). AFM images and data were obtained using Asylum MFP-3D Classic (Asylum Research, Santa Barbara, CA).

3.3.1   Water Contact Angle Measurements

Local plasma treatment of PCL samples were completed following the parameters from Table 1 unless stated otherwise. The plasma-treated and native samples of PCL were examined by the water contact angle technique. 2 µL of deionized water was dispensed from pipette tips (describe the technique of "placement") to the center of each sample and its profile was examined by a goniometer. WCA measurements were characterized via a drop shape analysis plug-in on ImageJ software (NIH), using the fitting of the Young-Laplace equation to the image data (Figure 14).
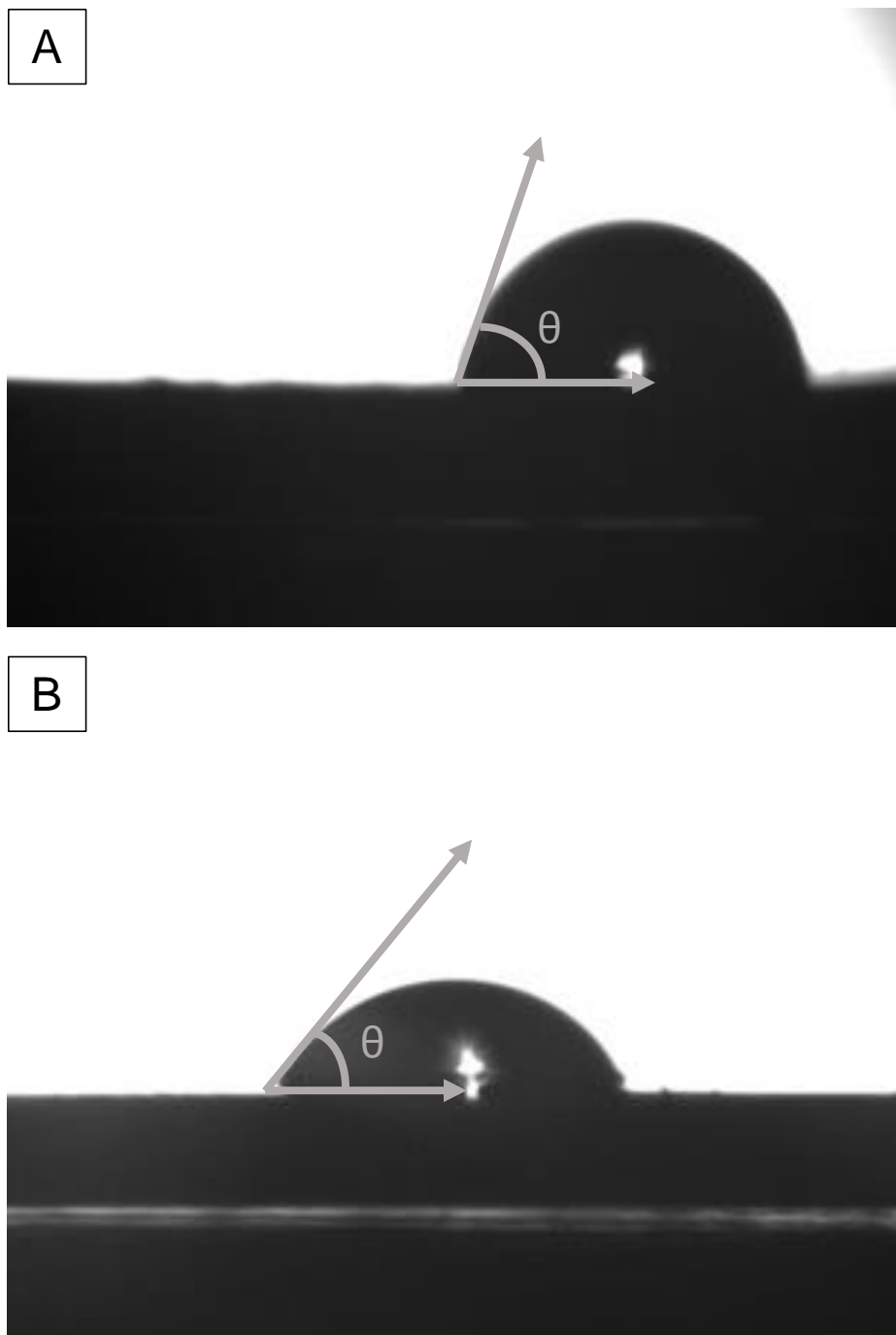
Figure 14. Comparison of water contact angles on PCL samples (A: native, θ = 82.92°; B: plasma-treated, θ = 61.18°).

The WCA values directly correlate with the surface wettability and

hydrophilicity in a reverse ratio. After fabrication, the contact angles of the native PCL samples are around 80°. Figure 15 represents the effect of changing the distance between the nozzle tip and the sample surface (sample size: n = 3). As the traveling speed and the distance increased, the effect of the plasma treatment weakened as higher WCA values were observed. Figure 16 presents the effect of power frequency on WCA at a distance of 1 mm from nozzle tip to sample surface for PCL. This figure indicates that as the traveling speed increased, the effect of plasma treatment weakened as higher WCA values were observed, which follows the same trend in Figure 15 (n = 3). However, the effect of changing power frequency is not linear with the increase in WCA value. The lowest values are observed at 20 kHz, indicating that this frequency is an optimal setting for current experiments to pursue better wettability and hydrophilicity (crucial for cell attachment). Compared to literature results [168], the WCAs in this study are higher due to a few factors that include different system configuration, lower power settings, shorter treatment time, etc.
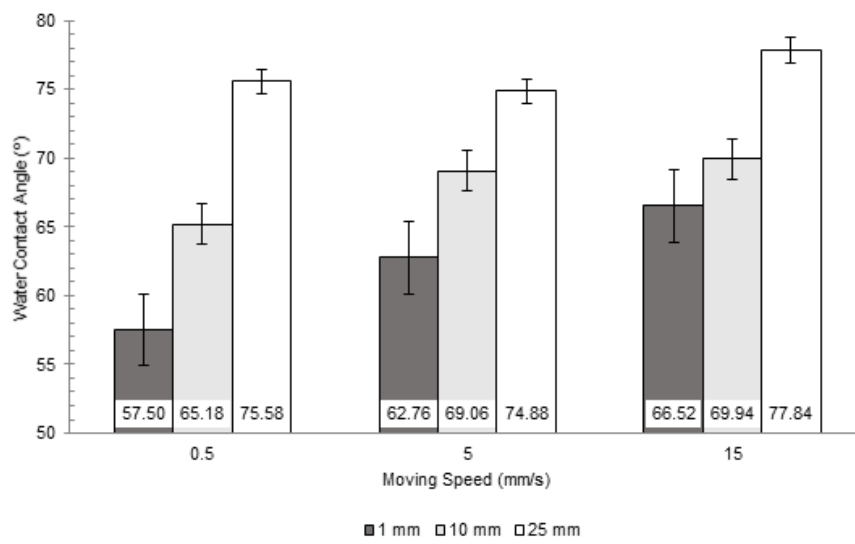
Figure 15. Effect of changing distances from nozzle tip to sample surface on WCA for PCL (power frequency: 30 kHz; sample size: n=3).
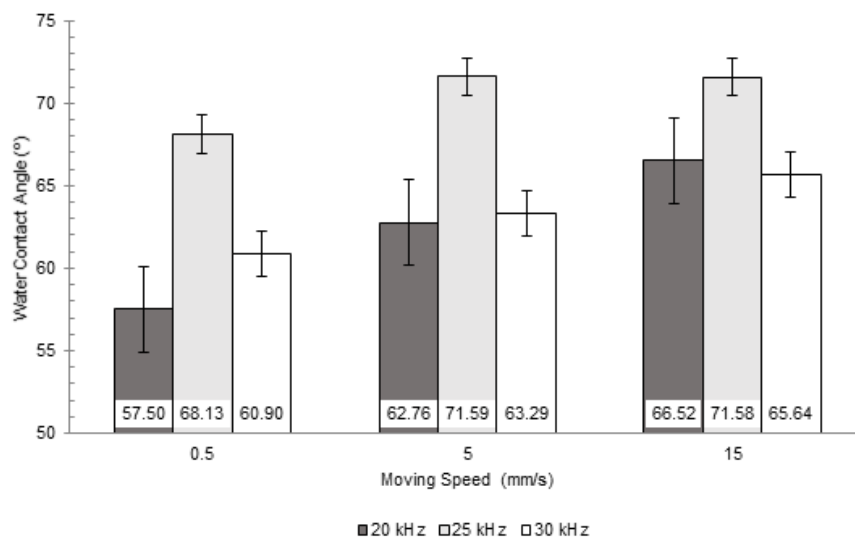
Figure 16. Effect of changing power frequencies on WCA for PCL (distances from nozzle tip to sample surface: 1 mm; sample size: n=3).

3.3.2 Surface Morphology

To visualize the surface change on the PCL samples, surface morphology images were taken via a scanning electron microscope (Zeiss Supra 50VP, Carl Zeiss Microscopy, Thornwood, NY). A single line path was programmed to be performed across the center of the round sample of PCL. The PCL samples were functionalized following the parameters from Table I and then transferred for SEM imaging.

In the SEM images shown in Figure 17, the line pattern produced by the microplasma is visible. The line pattern can be easily differentiated from an untreated 'background', as a result of change in surface morphology. The nozzle size was 150 µm, and the visible line pattern's width was approximately 55 µm.
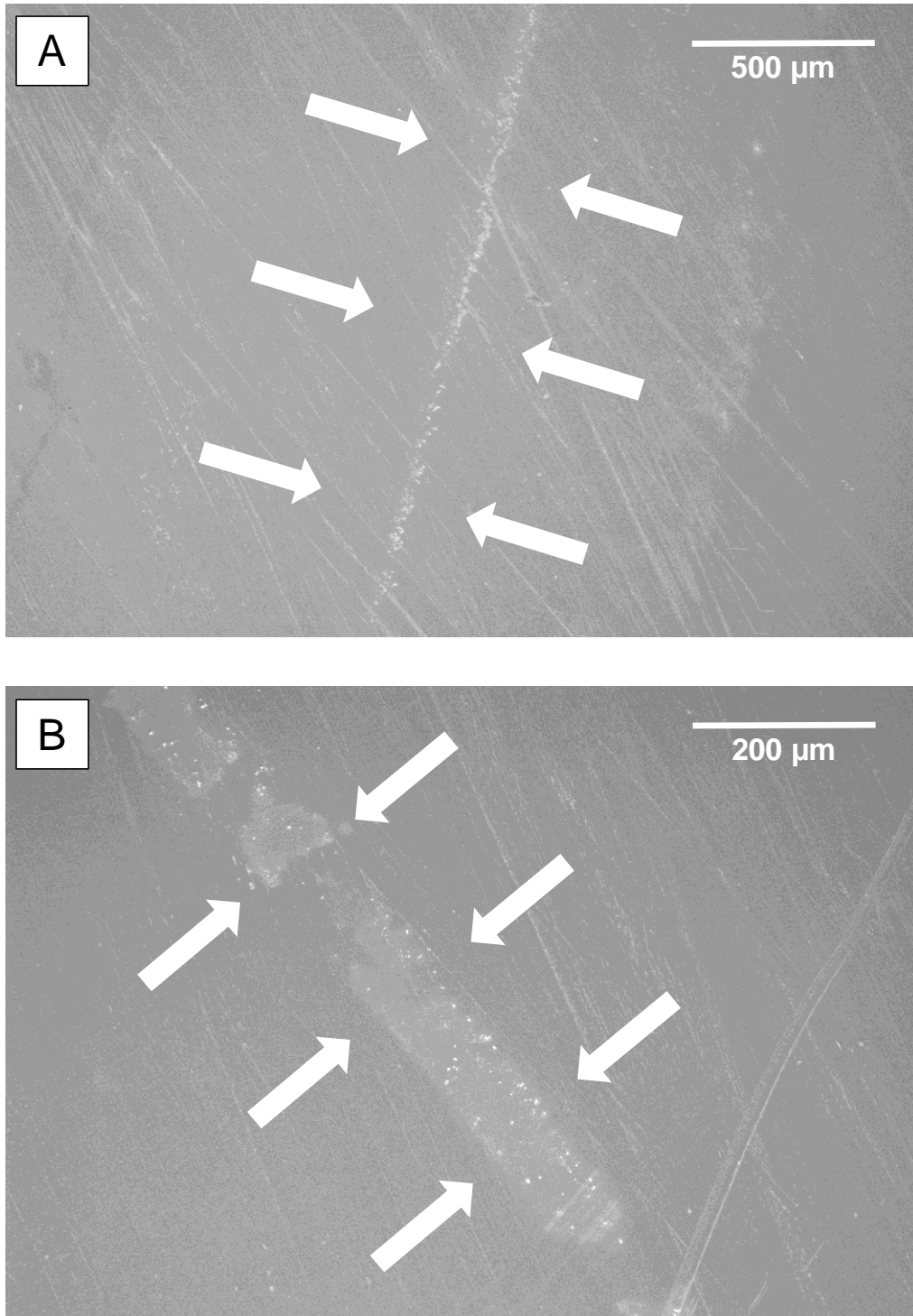
Figure 17. SEM images of the microplasma pattern: (A: general view; B: closed-up view).

The topology change was further validated by AFM images. The results of the root-mean-square-roughness (RMSR) for unmodified and plasma modified PCL are given in Table 2, with the ± representing the standard deviation of roughness for each modification measurement (sample size: n=3). After a quick microplasma treatment, surface root mean square roughness increased approximately 20%.

Wenzel's theory relates the water contact angle for a surface to that of a smooth surface through a roughness factor r (r>1):

$$r = \frac{cos\theta_{rough}}{cos\theta_{smooth}}$$

This equation indicates that if the surface has a contact angle of less than 90°, the angle will be decreased by an increase in surface roughness. PCL has a native contact angle less than 90°, therefore the more aggressive the plasma treatment, the rougher the surface, and the smaller value of contact angle [169].
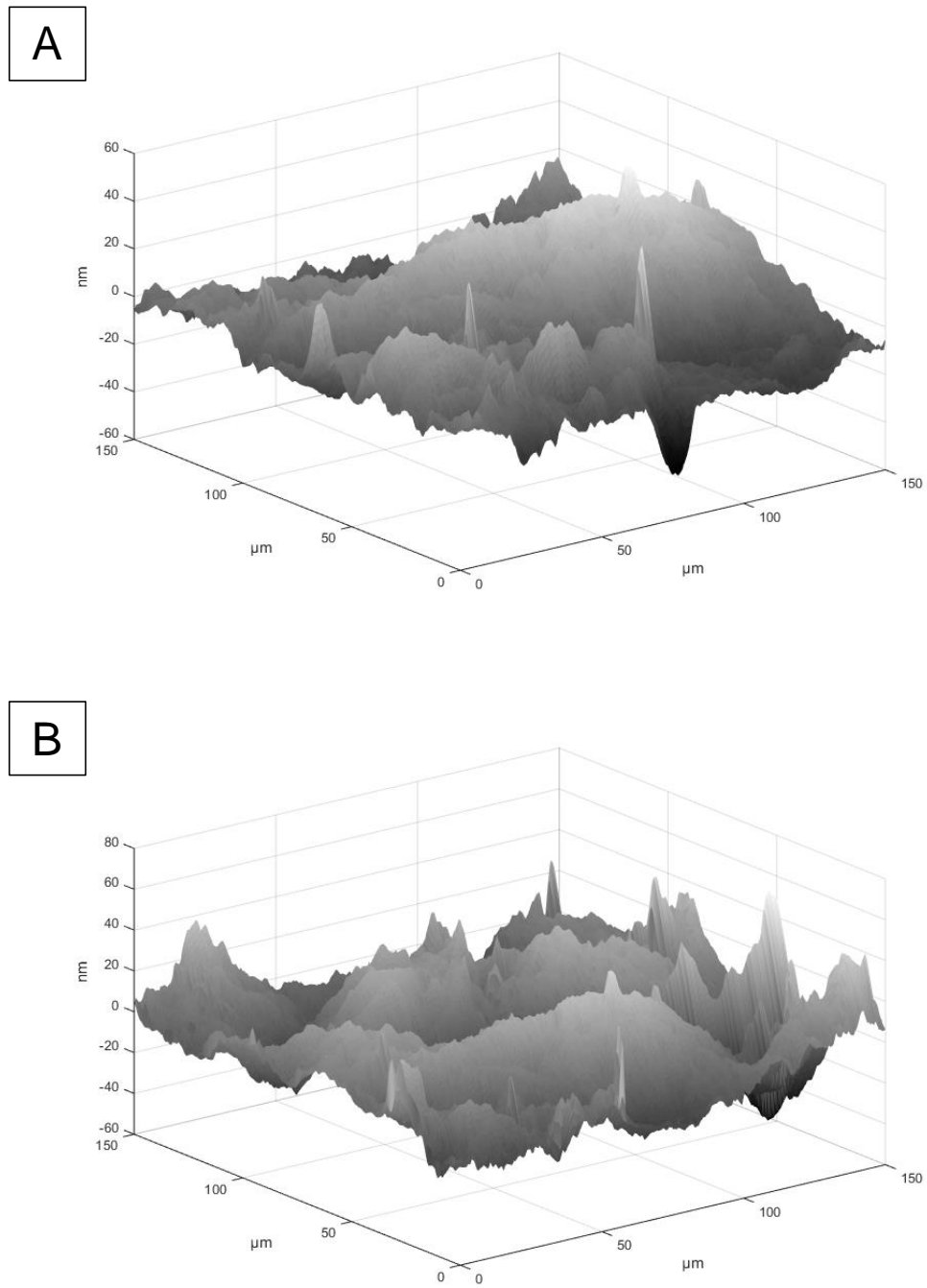
Figure 18. AFM images of (A) native and (B) modified PCL surfaces.

Table 2. Surface root mean square roughness (RMSR) for unmodified and modified PCL.

Substrate Type	Surface Root Mean Square Roughness
Native	43±5
Modified	52±8

3.3.3   X-Ray Photoelectron Spectroscopy (XPS) Analysis

X-ray photoelectron spectroscopy (XPS) from Centralized Research Facilities of Drexel University were used to analyze the surface chemistry change, especially surface chemical composition and functional group introduction. Two survey XPS spectra were presented to show the major chemical elements on the surfaces of both unmodified and modified (plasma-treated) samples (Figure 19). The surface atomic concentrations of atomic carbon, oxygen, and silicon are presented in Table 3.
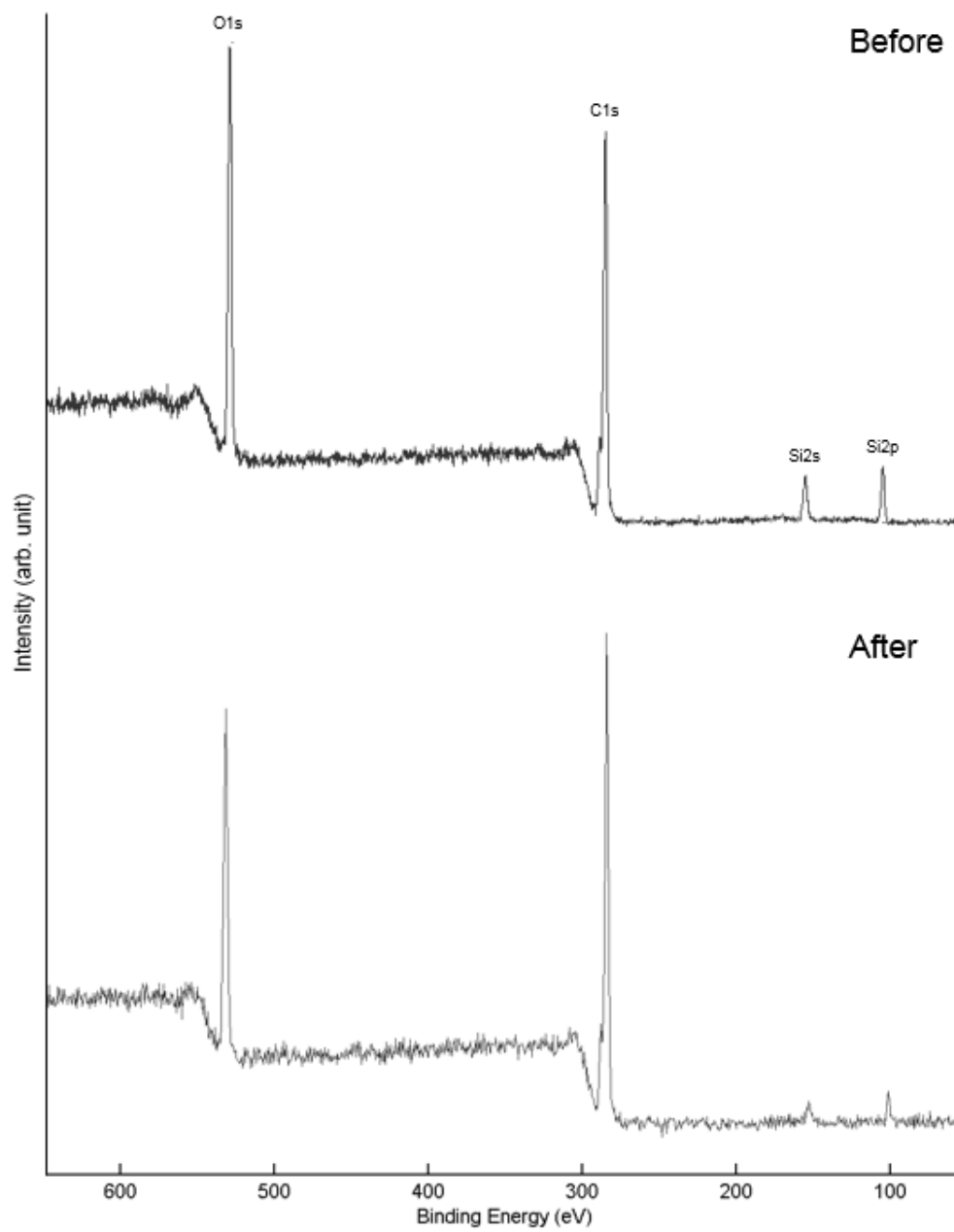
Figure 19. Survey XPS spectra of PCL before and after plasma treatment.

Table 3. Surface atomic concentrations of native and modified PCL surfaces.

Substrate Type	Atomic Concentration (%)		
	C	O	Si
Native	63.1	30.4	6.5
Modified	78.3	27.8	1.9

Certain concentrations of silicon were found in the PCL sample; it may be due to the fabrication process with glass mold and/or the preparation step for XPS analysis. After microplasma treatment, there was a significant decline in silicon concentrations, which could be a result of increased carbon and oxygen functional groups on the surface, introduced by plasma treatment.

To further investigate the functional group change on the PCL surface, high-resolution XPS spectra of carbon were acquired. Deconvolution of C1s peak was conducted by a non-linear least square curve-fitting program MultiPak (Physical Electronics, Chanhassen, MN) along with comparison to literature data [170]. The fractions of carbon-based functional groups are tabulated in Table 4.

Table 4. Fractions of functional groups of native and modified PCL surfaces.

Substrate Type	Fraction of functional groups (%)			
	Graphitic C-C, C-H 283.9 eV; (C1)	Hydroxyl C-OH 285.3 eV; (C2)	Carboxyl -O-C=O-COOH 288.0 eV; (C3)	Carbonyl C=O 286.1 eV; (C4)
Native	74.85	17.01	8.14	NA
Modified	77.77	11.39	8.15	2.68

Figure 20 shows high-resolution XPS spectrum of carbon on unmodified and modified (plasma-treated) PCL surfaces. Before microplasma modification, graphitic (C1), hydroxyl (C2), and carboxyl (C3) groups are found in the XPS spectrum, with a peak at 283.9 eV, 285.3 eV, and 288.0 eV, respectively. A new functional group, a carbonyl group with a peak at 286.1 eV, was observed in the XPS spectrum of the plasma functionalized sample surface. This suggests that plasma-induced reactions occurred on the surface of PCL, which changed the surface morphology (as observed before) and the surface chemistry.
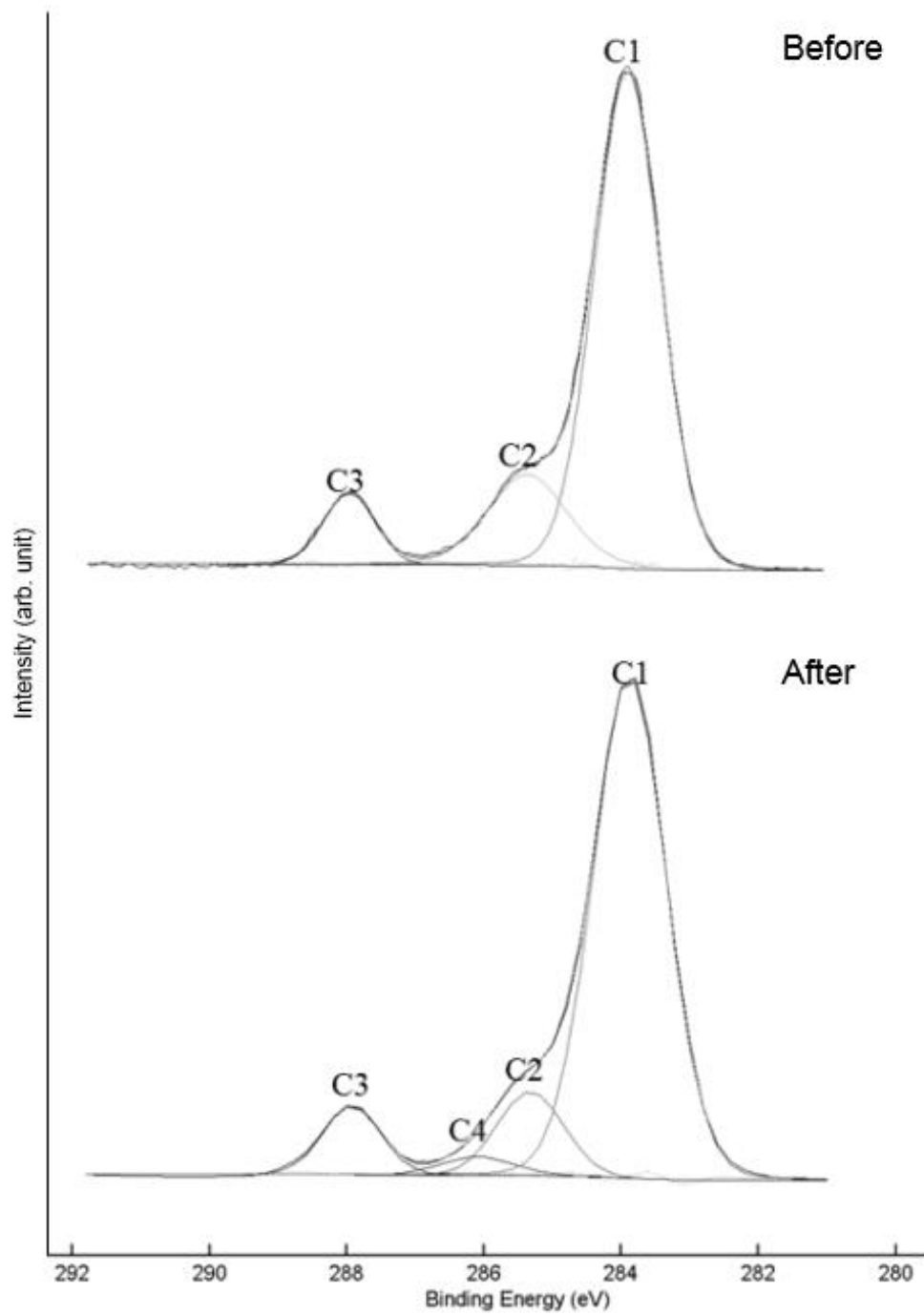
Figure 20. High-resolution C1s XPS spectra of PCL before and after plasma treatment.

3.4 Biological Investigations

7F2 cells are acquired from American Type Culture Collection (ATCC, Manassas, VA). The cells were cultured in 90% alpha minimum essential medium with 2 mM l-glutamine and 1 mM sodium pyruvate (Sigma-Aldrich, St. Louis, MO), and with 10% fetal bovine serum (Gibco, Grand Island, NY). Cells were maintained in incubator equilibrated with 5% carbon dioxide (CO_2) at 37 °C. At confluency, cells were trypsinized, counted and re-suspended to a cell density of 1×10^6 cells/mL. Culture medium was changed every 2 to 3 days.

A MarkerGene™ Live:Dead/Cytoxicity assay kit was used to analyze cell viability and cytotoxicity. A Live:Dead solution was created using propidium iodide with carboxyfluorescein diacetate according to the manufacturer's protocols. The damaged cells were marked fluorescently red and the intact cells were marked green by carboxyfluorescein dye. Red fluorescence could be observed with excitation and emission at 493 nm and 630 nm, respectively. Green fluorescence could be observed with excitation and emission at 475 nm and 517 nm, respectively. An alamarBlue® Kit (AbD Serotec, Raleigh, NC) was used to determine cell proliferation rates. The excitation and emission wavelengths for alamarBlue® assay were 535 and 590 nm, respectively. Quantitative data for cell viability and proliferation were collected using the microplate reader (GENios, Tecan Systems, San Jose, CA).

The studies of cellular response aim to identify the effects of a microplasma-

functionalized area on cell activities including attachment, proliferation, and differentiation. After being microplasma patterned, the functionalized area of the biopolymer was seeded with cells. AlamarBlue® assay, which incorporates a fluorometric indicator directly based on proportional relationship between fluorescence intensity and cell viability, was used to quantify cell proliferation. Live:Dead assay was used to measure the metabolic activity of cells. The morphology of cells attached to a PCL sample surface was examined by SEM.

In previous studies, [54] the results indicated that 1% O_2 (He at 0.5 slpm, O_2 at 5 sccm) was the optimal gas composition of plasma treatment for cell studies. A line pattern microplasma treatment was performed on each PCL sample using the working parameters in Table 1. The 7F2 cells were later seeded on both treated and native PCL samples following standard cell culture protocol described previously. Figure 21 shows that the microplasma treatment improved both cell viability and proliferation at 6 hour, 12 hour, 18 hour, and 24 hour time points (n = 3). The peak of fluorescence intensity for both plasma treated and control group appears at 24 hour time point, with the former being 1.5 times as large as the latter. Fluorescent images were taken 24 hours to observe cellular activity. Figure 22 shows a high density of cells on functionalized PCL sample surface in comparison to a low cell density on native PCL sample surface (n = 3). This further validates that cells selectively adhered to the plasma patterned area. Microplasma treatment on the PCL surfaces resulted in oxygen-related functional groups such as C-O, C=O, and O=C-O, which could improve the attachment of cells. Compared to the

microplasma pattern in Figure 22, the cells were observed to occupy a wider area, which could be a result of cell spreading and migration over time.
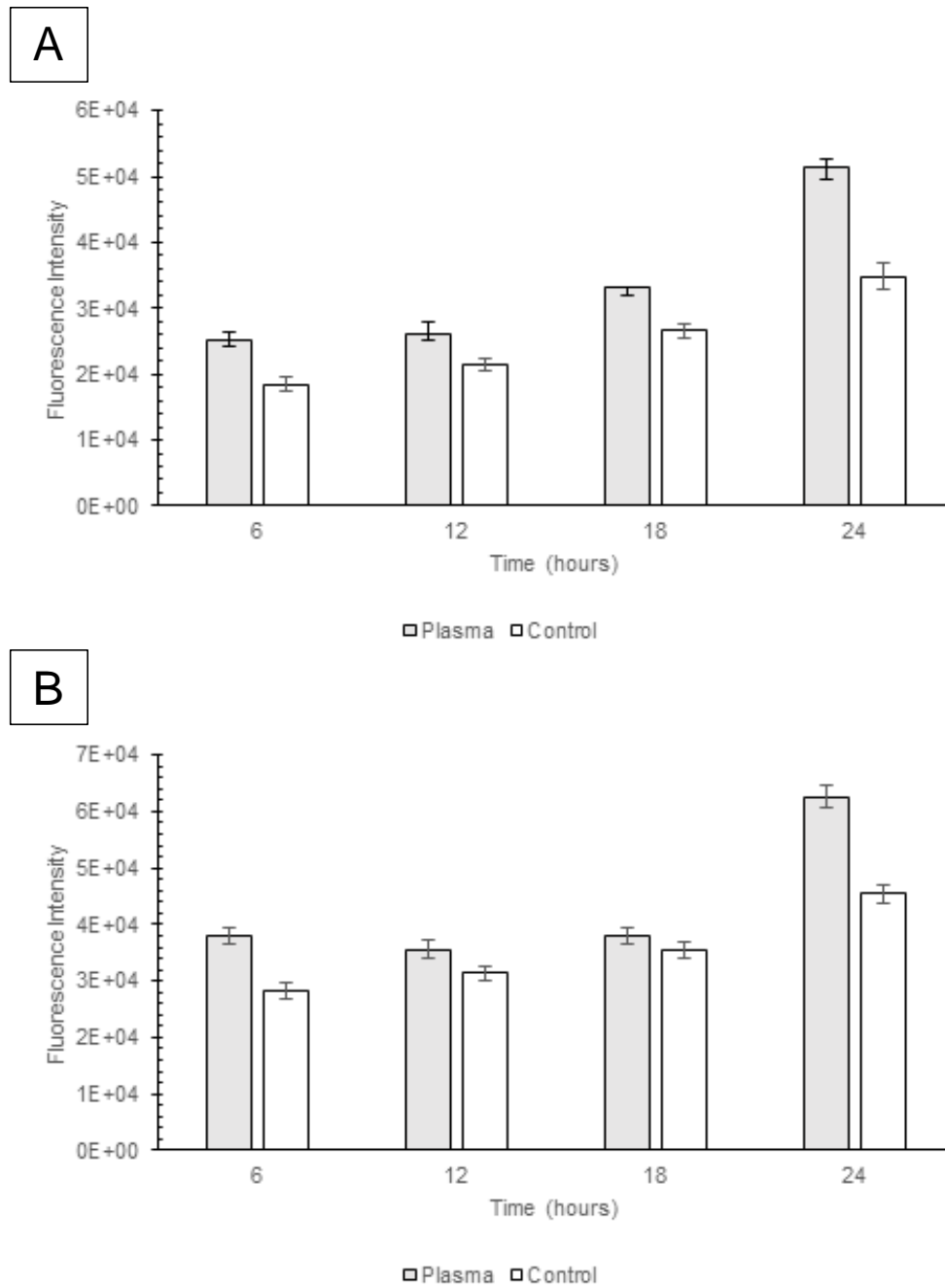
Figure 21. 7F2 cell viability and proliferation on PCL samples (A: cell viability results from

Live:Dead assays; B: cell proliferation results from alamarBlue® assays; sample size: n=3).
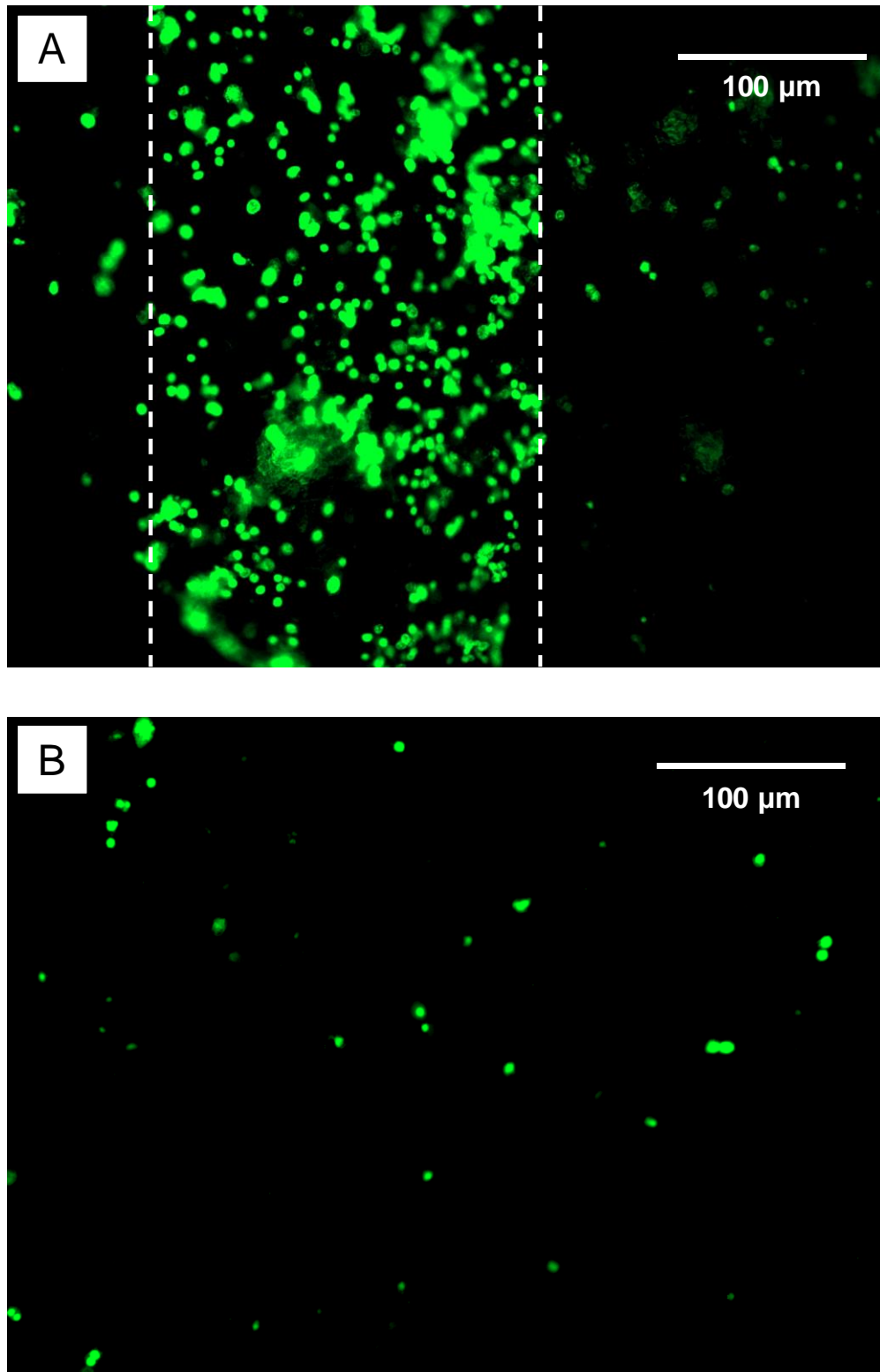
Figure 22. Fluorescent images of 7F2 cells on PCL samples after 24 hours (top: cells on microplasma patterned surface; bottom: cells on native surface; magnification: 10X).

SEM images were taken after 24 hours of incubation to better visualize the morphology of cells. Figure 23 presents a close-up SEM image of 7F2 cells well spread and attached to the functionalized surface on PCL sample. An elongated, rather than round cell, morphology was also observed in this image. These studies indicate that the localized microplasma treatment improved surface morphology and chemistry, caused an increase in hydrophilicity, and thus improved cell viability and proliferation. It was reported that oxygen functional groups were able to minimize the free energy of the interface between polymer surface and the surrounding medium [171]. Also, oxygen-based plasma discharge generates oxygen radicals which polarize the surface and surface becomes negatively charged. The negative charge attracts proteins (supplemented with serum) from the media as adhesion factors [172]. This localized microplasma treatment has the potential to pioneer bioactive PCL scaffolds with selective surface functionalization for applications in bone tissue engineering, etc.
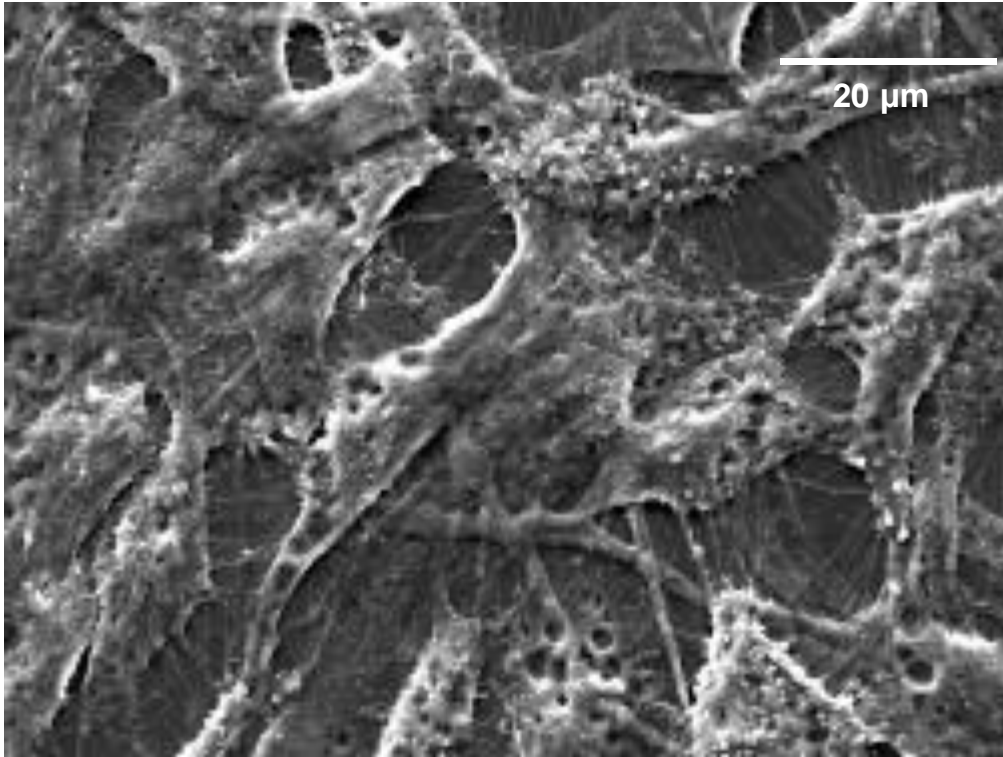
Figure 23. Scanning electron microscopy (SEM) images of cells on a microplasma patterned area of PCL sample after 24 hours (magnification: 1000X).

CHAPTER 4: MODELING OF A DIELECTRIC BARRIER DISCHARGE (DBD) MICROPLASMA JET

4.1   Plasma Modeling in General

Through optimized biomaterial selection, fabrication methods, physical, chemical, and biological surface modification techniques, researchers are able to control cellular functions of their tissue/cell platform's environment [173]. However, identifying the appropriate surface modification parameters and cues through experimental studies might be time consuming and costly. Researchers have been developing numerous models to predict the degree of surface functionalization from plasma modification and changes in surface physical and chemical properties [174]. Some early attempts were made by Graves and Humbird to simulate plasma etching of silicon using a molecular dynamics model [1]. In a highly cited journal article, Sakiyama and Graves presented a RF (13.56 MHz) two-dimensional axisymmetric numerical model of a plasma needle in helium to observe the expansion of charged species [2]. Bhoj and Kushner created a two-dimensional plasma hydrodynamics-surface kinetics model of Helium/Oxygen/Water plasma to investigate species accumulation on polypropylene [3]. In a review article, Schwaederle et al. summarized modeling plasma and plasma-surface interactions with several techniques, including fluid modeling, Monte Carlo (MC) simulations, Particle-in-Cell-Monte Carlo Collisions (PIC-MCC) simulations, hybrid Monte Carlo-Fluid Modeling Network, and molecular dynamics simulations [4]. Most models mentioned in these studies are case-specific and cannot be applied to other

systems. Therefore, a specific model need to be developed to predict the degree of surface functionalization, while reducing the input of extensive experiment data.

4.2 Plasma Kinetics Model Overview

In a typical dielectric barrier discharge (DBD) setting, there is a small gap filled with a feeding gas in between a high voltage electrode and a grounded dielectric barrier. The gap is typically several millimeters. In this chapter a 2D axisymmetric cylindrical model is development to capture the characteristics of DBD with He/O_2 mixture. In the cylindrical model, a sinusoidal voltage is applied on the inner electrode while the outer electrode is grounded. The geometry for a typical dielectric barrier discharge is shown in Figure 1.
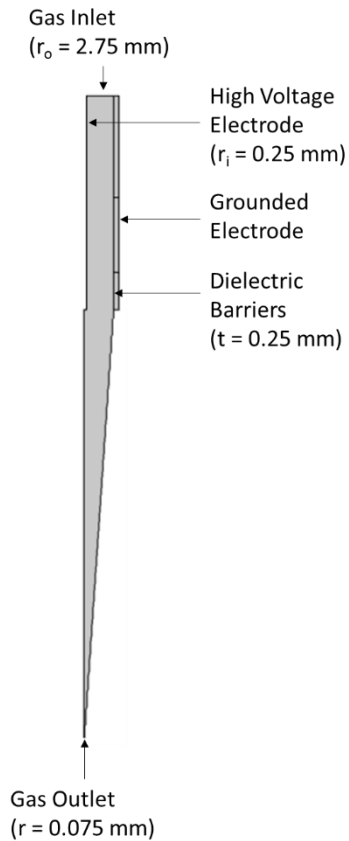
Figure 24. Graphic illustration of the cylindrical dielectric barrier discharge model; maximum height = 60 mm.

As the voltage applied to the center electrode increases, a stronger electric field forms in the gap between the electrodes. Any free electrons in the gap will be accelerated and if the electric field is strong enough they may acquire enough energy to cause ionization. This can lead to a cascade effect where the number of electrons in the gap increases exponentially on a nanosecond timescale. Electrons created via electron impact ionization rush towards dielectric barrier, in the opposite direction to the electric field. An equal number of ions are also generated

during electron impact ionization (electrons and ions must be created in equal pairs to preserve the overall charge balance). As a result, surface charge with opposite sign accumulates on the dielectric barrier. This causes the electric field to become shielded from the gas filled gap. In fact, the electric field across the gap cannot exceed the breakdown electric field, which is highly dependent on the gas. The breakdown electric field is also a function of the surface properties of the dielectric material. Surface charge accumulation temporarily terminates the discharge until the field reverses direction and the process repeats in the opposing direction.

Modeling dielectric barrier discharges in more than one dimension is possible, but the results can be difficult to interpret due to the amount of competing physics in the problem. In this chapter the problem is reduced to a 2D axisymmetric cylindrical model. It allows us to quickly gain some insight into the characteristics of the discharge without excessive computation time.

4.2.1   Domain Equations

Most of the following domain and boundary equations come from the commercial finite element software COMSOL Multiphysics (Burlington, MA).

Electron density n_e and mean electron energy n_ε are solved from a pair of drift-diffusion equations (convection of electrons due to fluid motion is neglected):

$$\frac{\partial(n_e)}{\partial t} + \nabla \cdot [-n_e(\mu_e \cdot E) - D_e \cdot \nabla n_e] = R_e \quad (Eq.\ 1)$$

$$\frac{\partial(n_\varepsilon)}{\partial t} + \nabla \cdot [-n_\varepsilon(\mu_\varepsilon \cdot E) - D_\varepsilon \cdot \nabla n_\varepsilon] = R_\varepsilon \quad (Eq.\ 2)$$

where n_e is electron density, n_ε is mean electron energy, μ_e is electron mobility, μ_ε is energy mobility, D_e is electron diffusivity, D_ϵ is energy diffusivity, R_e is electron source, and R_ε is energy loss due to inelastic collisions.

The electron diffusivity D_e, energy mobility μ_ε, and energy diffusivity D_ϵ can be calculated from the electron mobility μ_e and electron temperature T_e using the following equations:

$$D_e = \mu_e T_e, \mu_\varepsilon = \left(\frac{5}{3}\right)\mu_e, D_\epsilon = \mu_\varepsilon T_e \quad (Eq.\ 3)$$

where D_e is electron diffusivity, μ_ε is energy mobility, D_ϵ is energy diffusivity, μ_e is electron mobility, and T_e is electron temperature

Electron source R_e is defined as:

$$R_e = \sum_{j=1}^{M} x_j k_j N_n n_e \quad (Eq.\ 4)$$

where x_j is mole fraction of target species for reaction j, k_j is the rate coefficient for reaction j, N_n is the total neutral number density, and n_e is electron density.

Electron energy loss R_ε is defined as:

$$R_\varepsilon = \sum_{j=1}^{M} x_j k_j N_n n_\varepsilon \Delta\varepsilon_j \quad (Eq.\ 5)$$

where x_j is mole fraction of the target species for reaction j, k_j is the rate coefficient for reaction j, N_n is the total neutral number density, and n_ε is mean electron energy, $\Delta\varepsilon_j$ is the energy loss from reaction j. The rate coefficients were found in literature (see 4.2.3).

For each non-electron species k, mass fraction w_k is solved from:

$$\rho\frac{\partial(w_k)}{\partial t} + \rho(u \cdot \nabla)w_k = \nabla \cdot j_k + R_k \quad (Eq.\ 6)$$

where w_k is mass fraction for species k , u is mass average velocity field, j_k is diffusive flux vector, and R_k is the rate expression for species k.

Electrostatic field V is solved from:

$$-\nabla \cdot \varepsilon_0\,\varepsilon_r\,\nabla V = \rho \quad (Eq.\ 7)$$

where ε_0 is vacuum permittivity, ε_r is relative permittivity, and ρ is space charge density.

Space charge density ρ is solved from:

$$\rho = q\left(\sum_{k=1}^{N} z_k n_k - n_e\right) \quad (Eq.\ 8)$$

where ρ is space charge density, z_k is charge of species k, and n_e is electron density.

4.2.2 Boundary Conditions and Initial Conditions

Surface charge accumulation is applied to the dielectric barrier that is next to the grounded electrode,:

$$n \cdot (D_1 - D_2) = \rho_s \quad (Eq.\ 9)$$

where D_k is diffusion coefficient, ρ_s is surface charge density.

ρ_s is solved from following equation on the surfaces:

$$\frac{d\rho_s}{dt} = n \cdot J_i + n \cdot J_e \quad (Eq.\ 10)$$

where $n \cdot J_i$ is the normal component of the total ion current density at the wall, and $n \cdot J_e$ is the normal component of the total electron current density at the wall.

The discharge is driven by a sinusoidal electric potential applied to the exterior boundary of one of the dielectric tube:

$$V = 0.5V_0 sin(\omega t) \quad (Eq.\ 11)$$

$$\omega = 2\pi f \quad (Eq.\ 12)$$

where V_0 is the applied peak-peak voltage V_0, f is the voltage frequency, and ω is the angular frequency that equals $2\pi f$.

The exterior boundary of the other dielectric barrier is partially grounded. The relative permittivity of borosilicate shell was set to be 4.8. The initial number neutral species and electrons were set to be 10^8 and 10^9 respectively to mimic an insulated environment. The densities of neutral species of helium, argon, and oxygen molecules are fixed at the initial values given by the fraction at the

atmospheric pressure. The gas temperature was fixed at room temperature, 300 K, as the gas heating due to the collisions among species was trivial as observed in experiments.

4.2.3 Plasma Reactions

This He/O₂ DBD plasma model employs 14 species including electrons e, helium atoms He, helium ions He^+, excited helium atoms He^*, helium dimer ions He_2^+, excited helium dimers He_2^*, ground-state oxygen atoms $O(\,^3P)$, positive oxygen ions O^+, negative oxygen ions O^-, positive oxygen molecule ions O_2^+, excited oxygen atoms $O(\,^1D)$, oxygen molecules O_2, excited oxygen molecules $O_2^*(\,^1\Delta_g)$, and ozone O_3. Table 5, T_e and T are expressed in volts and Kelvins, respectively; $O(\,^3P), O(\,^1D), O_2^*(\,^1\Delta_g)$ are indicated by O, O^*, O_2^*, respectively. A total of 49 reactions were considered in this model (Table 5).

Table 5. Chemical reactions assumed in He/O2 mixture.

No.	Chemical Reaction	Rate Constant (cm³·s⁻¹)
--- Helium Reaction (HR) ---		
HR1	$e + He \rightarrow He^* + e$	$4.2E^{-9}T_e^{0.31}e^{-\frac{19.8}{T_e}}$
HR2	$e + He^* \rightarrow He + e$	$2E^{-10}$
HR3	$e + He \rightarrow He^+ + 2e$	$1.5E^{-9}T_e^{0.68}e^{-\frac{24.6}{T_e}}$
HR4	$e + He^* \rightarrow He^+ + 2e$	$1.28E^{-7}T_e^{0.6}e^{-\frac{4.78}{T_e}}$
HR5	$e + He_2^* \rightarrow He_2^+ + e$	$9.75E^{-10}T_e^{0.71}e^{-\frac{3.4}{T_e}}$

HR6	$e + He_2^+ \rightarrow He^* + e$	$5E^{-9}T_e^{-0.5}$
HR7	$e + He_2^+ \rightarrow 2He$	$1E^{-8}$
HR8	$e + He_2^+ + He \rightarrow 3He$	$2E^{-27}$
HR9	$2e + He_2^+ \rightarrow 2He + e$	$5E^{-27}T_e^{-4.5}$
HR10	$2He^* \rightarrow He^+ + He + e$	$2.7E^{-10}$
HR11	$He^* + 2He \rightarrow He_2^* + He$	$1.3E^{-33}$
HR12	$He^+ + 2He \rightarrow He_2^+ + He$	$1E^{-31}$
	--- Oxygen Reaction (OR) ---	
OR1	$e + O_2 \rightarrow O_2 + e$	$4.7E^{-8}T_e^{0.5}$
OR2	$e + O_2 \rightarrow O_2^* + e$	$1.7E^{-9}e^{-\frac{3.1}{T_e}}$
OR3	$e + O_2^* \rightarrow O_2 + e$	$5.6E^{-9}e^{-\frac{2.2}{T_e}}$
OR4	$e + O_2 \rightarrow O + O^* + e$	$5.0E^{-8}e^{-\frac{8.4}{T_e}}$
OR5	$e + O \rightarrow O^* + e$	$4.2E^{-9}e^{-\frac{2.25}{T_e}}$
OR6	$e + O^* \rightarrow O + e$	$8E-9$
OR7	$e + O^* \rightarrow O^+ + 2e$	$9E^{-9}T_e^{0.7}e^{-\frac{11.6}{T_e}}$
OR8	$e + O_2 \rightarrow O^- + O$	$8.8E^{-11}e^{-\frac{4.4}{T_e}}$
OR9	$e + O_2 \rightarrow 2O + e$	$4.2E^{-9}e^{-\frac{5.6}{T_e}}$
OR10	$e + O_2 \rightarrow O_2^+ + 2e$	$9E^{-10}T_e^{0.5}e^{-\frac{12.6}{T_e}}$
OR11	$e + O^- \rightarrow O + 2e$	$2E^{-7}e^{-\frac{5.5}{T_e}}$
OR12	$e + O_2^+ \rightarrow 2O$	$2.2E^{-8}T_e^{-0.5}$
OR13	$e + O_2 \rightarrow O^- + O^+ + e$	$7.1E^{-11}T_e^{0.5}e^{-\frac{17}{T_e}}$
OR14	$e + O_2 \rightarrow O + O^+ + 2e$	$5.3E^{-10}T_e^{0.9}e^{-\frac{20}{T_e}}$
OR15	$e + O \rightarrow O^+ + 2e$	$9E^{-9}T_e^{0.7}e^{-\frac{13.6}{T_e}}$

OR16	$e + O_3 \rightarrow O_2^- + O$	$1E^{-9}$
OR17	$O^- + O_2^+ \rightarrow O + O_2$	$2E^{-7}\left(\dfrac{200}{T}\right)^{0.5}$
OR18	$O^- + O \rightarrow O_2 + e$	$5E^{-10}$
OR19	$O^- + O_2^+ \rightarrow 3O$	$1E^{-7}$
OR20	$O^- + O^+ \rightarrow 2O$	$2E^{-7}\left(\dfrac{300}{T}\right)^{0.5}$
OR21	$O^+ + O_2 \rightarrow O + O_2^+$	$2E^{-11}\left(\dfrac{300}{T}\right)^{0.5}$
OR22	$O_2^* + O_2 \rightarrow 2O_2$	$2.2E^{-18}\left(\dfrac{300}{T}\right)0.8$
OR23	$O_2^* + O \rightarrow O + O_2$	$7E^{-16}$
OR24	$O^* + O \rightarrow 2O$	$8E^{-12}$
OR25	$O^* + O_2 \rightarrow O + O_2$	$7E^{-12}e^{\frac{67}{T}}$
OR26	$O^* + O_2 \rightarrow O + O_2^*$	$1E^{-12}$
OR27	$O^- + O_2 \rightarrow O_3 + e$	$5E^{-15}$
OR28	$O^- + O_2^* \rightarrow O_3 + e$	$3E^{-10}$
OR29	$O^- + O_2^* \rightarrow O_2^- + O$	$1E^{-10}$
OR30	$O_3 + O_2 \rightarrow 2O_2 + O$	$7.3E^{-10}e^{-\frac{11400}{T}}$
OR31	$O_3 + O \rightarrow 2O_2$	$1.8E^{-11}e^{-\frac{2300}{T}}$
OR32	$2O + O_2 \rightarrow 2O_2$	$2.5E^{-31}T^{-0.63}$
OR33	$O + 2O_2 \rightarrow O_3 + O_2$	$6.9E^{-34}\left(\dfrac{300}{T}\right)^{1.25}$
OR34	$O_2^* + O_3 \rightarrow 2O_2 + O$	$6.0E^{-11}e^{-\frac{2853}{T}}$
	--- Helium-Oxygen Reaction (HOR) ---	
HOR1	$e + O_2 + He \rightarrow O_2^- + He$	$1E^{-31}$
HOR2	$2O + He \rightarrow O_2 + He$	$1.3E^{-33}\left(\dfrac{3000}{T}\right)e^{-\frac{170}{T}}$

HOR3	$O_2^* + He \rightarrow O_2 + He$	$8E^{-21}$

4.3   Plasma Structure

The plasma model is solved for applied voltage of 4kV and 6kV, and for helium/oxygen (1%) flows of 400 and 600 sccm, until the average power deposited reaches a steady state (t $\sim$ 8 µs) corresponding to convergence in reactive neutral species production. A basic stationary laminar flow model was first solved to provide live pressure and velocity field; it was then coupled with a time-dependent plasma discharge model. The outputs results such as the steady-state solution for charged particle density, electron temperature and electric field have been calculated with the use of COMSOL. A He/O_2 plasma discharge with density$\sim 10^{19}$ cm^{-3} forms around the inner electrode tip, but this rapidly decreases to $\sim 10^{16}$ cm^{-3} in the downstream region. A thin sheath structure is formed extending from the electrode tip along the sides (Figure 25). As shown in Figure 26, the electron density reaches a maximum value of 2.59×10^{11} m^{-3} at about 0.06 m from the cathode. The results were generally in line with similar studies reported in other journals [175], [176]. In the results discussed here, the densities of oxygen atom (O) reached a steady state over a few ms (Figure 27). The extent of surface functionalization was investigated as a function of oxygen number density (Figure 28).
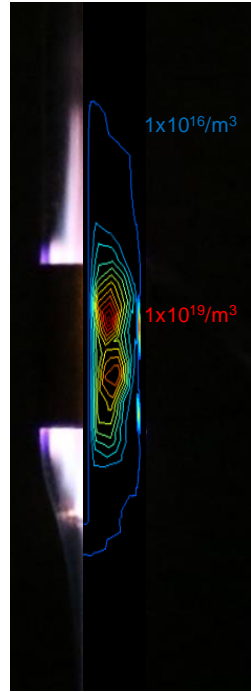
Figure 25. Solved He* number density in comparison with photograph
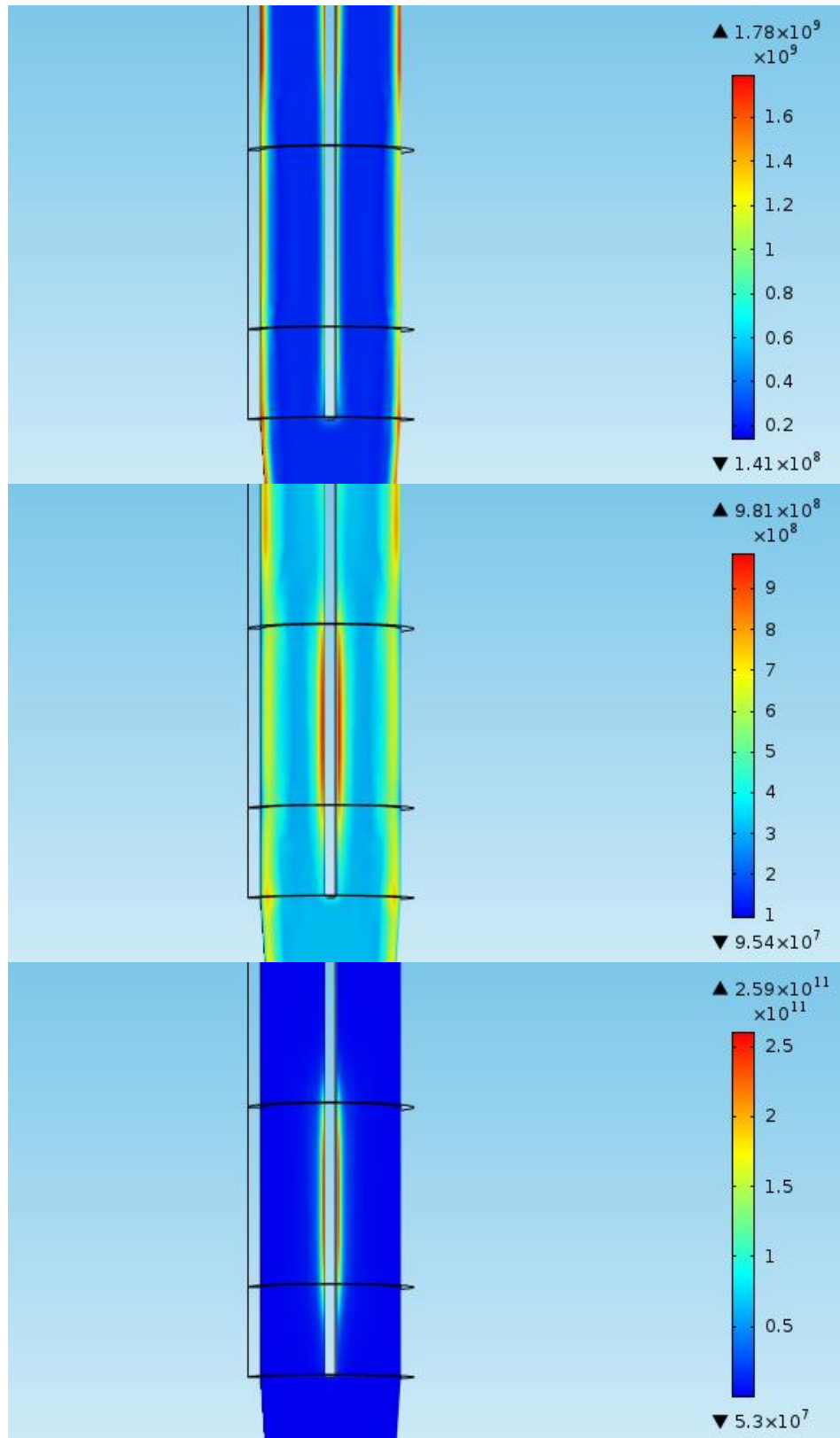
Figure 26. Electron density distribution in plasma jet at 50 ns, 100 ns, and 1 µs (top to bottom).
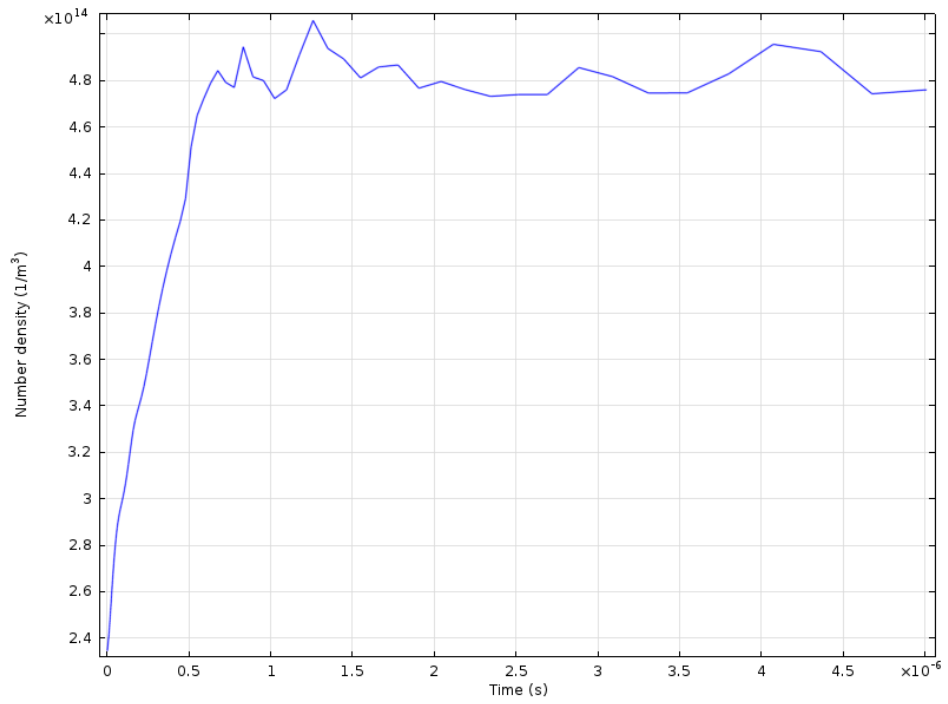
Figure 27. Average oxygen atom (O) density at tip of plasma jet.
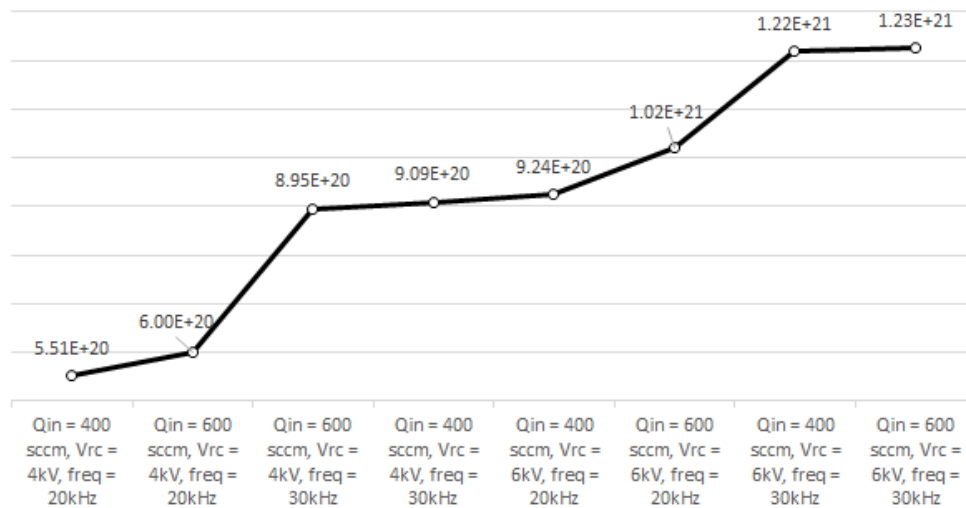
Figure 28. Average oxygen atom and ozone number density under different flow rate (Qin), peak-peak voltage (Vrc), and power frequency (freq).

4.4 Orthogonal Experiment Analysis

An orthogonal experimental design and analysis method was applied to study the effects of some parameters not included in, or derived from the kinetics model for DBD microplasma treatment of PCL. In this trial case, three DBD plasma system parameters involved in , namely nozzle moving speed (v), distance from nozzle tip to substrate (d), and average oxygen number density at scale of 10^{12} (o) were investigated.

Table 6. System parameters with contact angle results.

	v (z1), mm/s	d (z2), mm	o (z3), 10^{12}	Contact Angle, °
1	1	1	6	55.954
2	1	3	9	57.377
3	1	5	12	58.429
4	3	1	12	57.382
5	3	3	6	57.387
6	3	5	9	67.769
7	5	1	9	67.067
8	5	3	12	68.196
9	5	5	6	73.042
Control				79.589

Table 7. A 3x3 orthogonal experimental design plan.

Investigated parameters	v (z1), mm/s	d (z2), mm	o(z3), 10^{12}
Zero level: 0	3	3	9
High level: +1	5	5	12
Lower level: -1	1	1	6
Level space	2	2	3

To calculate the regression coefficients of normalized parameters, the original states were normalized to generate new variables, varying within the range of [-1, 1]. The following equation set including zero levels and level spaces was used in data processing:

$$X_1(z_1) = \frac{z_1 - \bar{z}_1}{\Delta_1} = \frac{z_1 - 3}{2} \quad (Eq.\ 13)$$

$$X_1(z_2) = \frac{z_2 - \bar{z}_2}{\Delta_2} = \frac{z_2 - 3}{2} \quad (Eq.\ 14)$$

$$X_1(z_3) = \frac{z_3 - \bar{z}_3}{\Delta_3} = \frac{z_3 - 9}{3} \quad (Eq.\ 15)$$

$$X_2(z_1) = 2\left[\left(\frac{z_1 - 3}{2}\right)^2 - \frac{2}{3}\right] \ (Eq.\ 16)$$

$$X_2(z_2) = 2\left[\left(\frac{z_2 - 3}{2}\right)^2 - \frac{2}{3}\right] \ (Eq.\ 17)$$

$$X_2(z_3) = 2\left[\left(\frac{z_3 - 9}{3}\right)^2 - \frac{2}{3}\right] \ (Eq.\ 18)$$

X_1, X_2 are first and second order of normalized system parameters respectively.

The rest of the regression coefficients D, B and b can be calculated as follows:

$$D_{mk} = \sum_{i=1}^{9}\left(X_m{}^2(z_k)\right)_i \ (Eq.\ 19)$$

$$B_{mk} = \sum_{i=1}^{9}(X_m(z_k) \cdot y)_i \ (Eq.\ 20)$$

$$b_{mk} = B_{mk}/D_{mk} \ (Eq.\ 21)$$

Table 8. Calculation results of coefficients.

	Φ	X1 (z1)	X2 (z1)	X1 (z2)	X2 (z2)	X1 (z3)	X2 (z3)	y
1	1	-1	1	-1	1	-1	1	55.954
2	1	-1	1	0	-2	0	-2	57.377
3	1	-1	1	1	1	1	1	58.429
4	1	0	-2	-1	1	1	1	57.382
5	1	0	-2	0	-2	-1	1	57.387
6	1	0	-2	1	1	0	-2	67.769
7	1	1	1	-1	1	0	-2	67.067
8	1	1	1	0	-2	1	1	68.196
9	1	1	1	1	1	-1	1	73.042
D	9	6	18	6	18	6	18	
Bj	562.603	36.545	14.989	18.837	13.723	-2.376	-14.036	
bj	62.511	6.091	0.833	3.140	0.762	-0.396	-0.780	

Y is the test results of water contact angles from labeled experiments previously, while m and k are the operational parameters in the array. The quantitative model between the water contact angle results and given system parameters can be expressed as:

$$y^* = \sum_{k=1}^{3} \sum_{m=1}^{2} b_{mk} X_m(z_k) \ (Eq. \ 22)$$

The calculated expression is as follows:

$$\theta = 62.511 + 6.091 X_1(z_1) + 0.833 X_2(z_1) + 3.140 X_1(z_2) + 0.762 X_2(z_2)$$
$$- 0.396 X_1(z_3) - 0.780 X_2(z_3) \ (Eq. \ 23)$$

After simplification using the relations from the first set of equations:

$$\theta = 0.4165 v^2 + 0.5465 v + 0.3810 d^2 - 0.6880 d - 0.1733 o^2 + 2.9880 o$$
$$+ 41.9033 \ (Eq. \ 24)$$

Equation 24 unified average oxygen number density, which is derived from the previous computational model, as well as the nozzle moving speed and distance from nozzle tip to substrate, which only exist in the dynamic treatment mode of localized microplasma process. Errors of computed contact angles are within 5% when compared to experimental results.

CHAPTER 5: DEVELOPMENT OF A CANCER CELL-ON-A-CHIP

DEVICE WITH LOCALIZED MICROPLASMA SURFACE

FUNCTIONALIZATION

One part of this work appeared in [1] and was done in collaboration with Zhenyu

Tang, Yu Zhao, Rui Yao, Lingsong Li, and Wei Sun.

Another part of this work appeared in [177] *and was done in collaboration with*

Qudus Hamid, Jessica Snyder, Shannon Williams, Yigong Liu, and Wei Sun.

5.1   Cell Printing for Cancer Models

Cell printing is based on bio-additive manufacturing technology, directly assembly cells with delivery medium to build 3D tissue constructs layer by layer [178]. This approach allows the assembly of heterogeneous tissue structure to mimic *in vivo* physiological tumor model, as well as the possibility of fabricating 3D *in vitro* tumor model with large-scale, high throughput and high cell density. Cell printing has provided a promising biofabrication technique to produce reliable 3D *in vitro* models. Pepper et al. designed a 2D inkjet system to deposit multiple cell types like murine mammary tumor cells (4T07) and murine mesenchymal stem cells (D1) in predefined patterns, powered by HP26 series print cartridge [179]. From 2D to 3D cell printing, Moon, S. developed a layer by layer 3D tissue droplet bioprinter to print bladder smooth muscle cells encapsulated within high viscosity collagen [180]. Xu et al. printed a 3D co-culture cancer model by a dual ejector setup with ovarian cancer cells (OVCAR-5) and fibroblasts (MRC-5) to a Matrigel substrate. Acini formation and cell viability were tested but no results about functional characterization of the cancer model were gained [181]. Kessel et al.

applied ejection technical to eject OVCAR-5 and MRC-5 cells separately and formed 3D co-culture cancer models for studying breast cancer initiation and progression [182]. These cancer models were used as quantitative therapeutic response platforms for ovarian cancer (OvCa) micrometastases, through which they demonstrated that BPD-PDT treatment of OvCa 3D micronodules substantially improves the efficacy of a clinically relevant dose [182].

Matsusaki et al. combined the rapid and automatic inkjet cell printing to fabricate micro-arrays of simplified human 3D-tissue structures with different cellular distributions [183]. This work reported hundreds of multilayered micro-tissues integrated into one micro-array and declared to reproduce 3D cell-cell interactions similar to actual tissue. Although HepG2 cells and HUVEC were co-cultured in chips, the cancer biological properties were not assessed in this work. Laura developed a micropatterned system using sequential microcontact printing of hyaluronic acid (HA) with ECM protein fibronectin [184]. Breast cancer cells laden HA micromolded hydrogels were spatially organized using this system, and analysis of the spatial and temporal mechanisms regulating tumor angiogenesis was declared to be available with this method. Zhao reported a controlled cell assembly for 3D tumor model using printing method with gelatin, alginate and Hela cells [185]. The Hela cells were successfully assembled to a construct and about 80% cells were alive after cell assembly, according to staining analysis. This demonstrated tumor cell assembly with the advantage of mimic ECM, large-scale

and high throughput had potential to build a biomimetic tumor model with 3D microenvironmental characteristics *in vivo* [185].

5.2 Development of a Multifunctional Biofabrication System

The integrated multifunctional cell printing system integrates several critical fabrication components utilized in the fabrication process of many biological arrays and platforms. These components include: 3D spatial control, material deposition, the ability to perform photolithographic processes, and plasma treatment systems. The 3D spatial control houses all the fabrication components on the z motion arm with connectivity to an x and y arm for complete 3D motion. The material deposition component houses the biological nozzle and the photo-polymer nozzle. The biologics head is a cell-friendly deposition nozzle on the motion arm that is used for the spatial deposition and orientation of cells and/or biologics into the micro-channels. The final nozzle of the material delivery component is a piston style nozzle which is used to drive material of higher viscosity, such as photo-polymers. The photolithographic head has a LED ultra-violet (UV) fiber optic head that is mounted on the motion arm. Photolithographic component is used for the crosslinking of the photoresist immediately after deposition. Prior to cell deposition, the plasma treatment head will treat the channels with a composition of helium and oxygen based plasma.
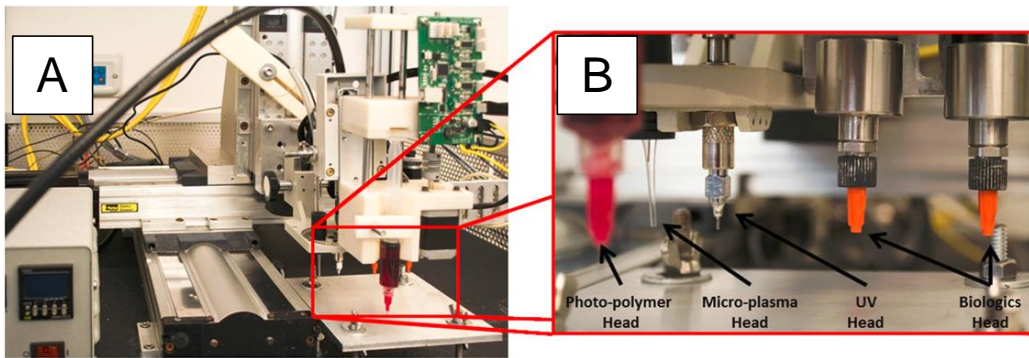
Figure 29. (A) An image of the integrated fabrication system; (B) close-up of the four fabrication heads respectively labeled.

The 3D spatial control component is integrated with all the components (UV, plasma, and material delivery nozzles) and functions independent of each component. Each component of this proposed system has a specific function; if a function or component is not needed, the scripts (program code) can be written to function as desired. All nozzles/print head are independent of each other and only one head is utilized at a single time. All print heads are housed on the third (Z- axis) motion arms. All nozzles utilize the spatial controllers in sequential order to develop and enhance the fabricated arrays while depositing biologics into the channels. The motion system is controlled by a proportional—integral—derivative controller, that allows for tuning of the entire system to function adequately with any given fabrication task.

Photosensitive polymer such as SU-8 requires direct exposure to UV light for the development of microchannels. The freeform UV micro-nozzle has a base LED UV lamp where a fiber optic cable is fed to the motion head. The fiber optic

cable is placed into the print head which is specifically designed to filter the light through an inter-changeable micro-nozzle. This component emits a peak UV light of 485 nm through 50–500 μm nozzles with a manufacturer's list maximum exposure of 15 W cm^{-2}. The freeform UV micro-nozzle is coupled with the photo-polymer head which allows for immediate crosslinking of the photo-resist upon deposition.

The photo-polymer head is specifically designed to work with high viscous material. Due to space limitations, the piston style design of this head enables the author to drive a small amount of material without requiring a lot of room. This head features a syringe–pump style deposition system that utilizes standard syringes with inter-changeable nozzles. The utilization of standard everyday products allows the end-users to work effectively with tissue culture products. The head is controlled with an Audrino micro-processor which is embedded into the motion software. The photo-polymer head is coupled with the freeform UV micro-nozzle. This placement allows for immediate cross- linking of the photo-resist upon deposition which retains structural integrity. Figure 3(B) shows an image of the photo-polymer head with its major components.

The biologics component is inspired by rapid proto-typing technology and is built on a CAD/CAM plat- form, which integrates with the 3D spatial control component. The biologics printer operates at room temperature and low pressure, necessary cell-friendly conditions. Coupled with the spatial control component, the

biologics printer can deposit multiple cell types and bioactive factors in controlled amounts with precise spatial positioning. The printer utilizes a micro-valve nozzle which enables the printer to deposit numerous solutions with a wide range of material and biological properties. This component eliminates human errors and provides the end users with precise biologics control during fabrication procedures. The biologics deposition component is capable of depositing heterogeneous materials, cell types, and biological factors in a controlled and reproducible manner [53–55]. Cell printing is considered to be an effective biofabrication tool to assemble biologics and will be used as such in this chapter.

The generation of plasma is done by changing the gas types, flow composition, and applied electric field within the nozzle along with the corresponding process parameter for generating the desired ignition. Plasma generation is the excitation of ions that bombard the substrate's surface to manipulate its topology, surface chemistry and functional groups. In this system, the micro-plasma is delivered through the dielectric barrier discharge (DBD) technique. DBDs are non-equilibrium plasmas operated under atmospheric pressure [168]. Due to a non-equilibrium nature, DBD plasmas can generate high energy electrons at cool background gas temperatures (heavy particles). This unique character (selective high electron temperature, and low background temperature) enables rich plasma chemistry in many plasma chemical processes [166]. The micro-plasma component consists of a power supply and the plasma electrode components. Micro-plasma will be generated by a pulsed power supply

with variable frequency. Connected to the power supply will be the plasma electrode system with a high voltage electrode coaxially inserted in a dielectric (borosilicate glass or quartz) tube and a ground electrode wrapped around the tube from the outside. The process gas (or gas mixture) will be purged through the annular gap between the coaxial electrode and the dielectric tube. When the high voltage electrode is powered, plasma ignites between the electrodes and a micron-scale glow-like plasma will appear at the tip of the nozzle. Once the micro-plasma contacts the surface of biopolymer, it will change the topography and chemistry of the plasma-exposed area. Depending on the micro-plasma operation parameters such as plasma power, gas flow rate, gas composition, and nozzle tip diameter, the users can control the surface chemistry and topological features of the exposed photo-polymer.

5.3   Fabrication of a Cancer Cell-on-a-chip Device

Limited nutrient and metabolic waste transport is an essential concern in spheroid constructs due to a large and dense ECM structure. Therefore, a call for microfluidic systems, which are known for compact size and accurate flow control, to be applied in *in vitro* cancer models is reasonable. Soft photolithography is the typical method to fabricate mold of the lab-on-chip device and Polydimethylsiloxane (PDMS) is widely used during the manufacturing process, for its biocompatibility and oxygen permeability. The PDMS molds are covered by glass coverslip with the edges fully sealed which allows microscopic observation of cells and tissues without involving exterior contamination [186].

Recent work focused on the combination of microfluidics and cell culture systems to improve the physiological significance and the reproducibility of cell-based assays [187]. A transparent microchannel array enables observation of spatial and temporal controls on the transition of breast cancer invasion [188]. The design of channels in a microfluidic device is often crucial to regulate cell behaviors, further to mimic tumor development and metastasis. Hsiao et al. developed a two-layer microfluidic system to co-culture spheroids of metastatic prostate cancer cells (PC-3), osteoblasts and endothelial cells; all of the cells were fluorescently labeled for separation, imaging and tracking. Their results demonstrated a large decrease in the proliferation rate of PC-3 cells with maintained viability, which recapitulate the growth behavior of malignant cancer cells within native *in vivo* microenvironment [82]. Moreover, Zervantonakis et al. engineered a microfluidic assay to reconstruct the 3D ECM of tumor-vascular interface; the results showed that the endothelium stalled tumor cell intravasation via microenvironment factors [189]. Generally, microfluidic system allows for analysis of cell kinetics and diffusion effects in growing cell populations which is distinctive among all models.

The cell-on-a-chip presented in this chapter was fabricated in two parts. The first part of the chip is referred to as the enclosure and the second part of the chip is the fabrication of the internal architecture. The enclosure is fabricated with an aluminum mold which produces a base enclosure and a lid. The base enclosure has a rectangular slot that is later utilized by the fabrication system to print, treat, and

deposit cells in the desired micro-architecture. The lid is flat and houses the inlet and outlet ports which are utilized for perfusion throughout the chips during the incubation period. The enclosure is made primarily out of polydimethylsiloxane (PDMS) (Dow Corning, Michigan, USA) and the inlet and outlet ports are nylon based luer-lock connectors (McMaster-Carr, Robbinsville, NJ, USA). PDMS is mixed at a 1:15 ratio, de-gassed and cured in an aluminum mold at 130 °C for 10 min. Cured PDMS is cooled and removed from the aluminum mold. This process is repeated for the lid where the luer-lock ports are placed into position prior to being cured on the hot plate. Figure 30(B) illustrates a model of the PDMS enclosure. Prior to the fabrication of the internal features of the chip, the enclosure goes through a dry heat sterilization process of 150 °C for 2 h.

The second part of the chip is the fabrication of the internal architecture which sits in the slot of the base enclosure. The internal micro-architecture of the chip is fabricated with the integrated system using SU-8 2100 (MicroChem Corp., Newton, MA, USA) as the building material. SU-8 is housed in the photo- polymer print head. The localized micro-plasma head uses a gas composition of 5% oxygen and 95% helium for plasma treatment [59, 60]. Cells used in studies presented in this chapter are MDA-MB-231 (breast cancer cells) and HepG2 (liver cancer cells) (American Type Culture Collection, Virginia, USA). Prior to printing, cells are harvested from a 75 cm^2 tissue culture flask and counted then re-suspended at a cell density of 1×10^6 cells/ml (50% MDA-MB-231, 50% HepG2) in culture medium (50/50, MDA-MB-231 culture medium/HepG2 culture medium) and placed in the

biologics head. The freeform UV micro-nozzle is set at 100% intensity with a 500 µm nozzle.

The fabrication of the internal architecture is done in a sequential series of steps:

Step 1: The first step is the photo-polymer head moving into the slot of the enclosure base, then depositing the SU-8 forming a line filament height of 0.5 mm.

Step 2: Once the first filament is printed, the UV head activates and follow the same toolpath and exposes the printed SU-8. This process is repeated until the desired 'layer' is printed and exposed (UV). The fabrication method utilized by this 3D printer is layer-by-layer fabrication.

Step 3: (Optional): Since the chip has only one layer, the fabrication of a second layer would be identical to the first (process-wise).

Step 4: Once the microchannels have been created, the plasma head will activate and move over the path of the printed microchannels, treating them.

Step 5: Once the plasma treatment is completed, the biologics head will follow the path of the micro- channels and print cells directly into channels.

Step 6: To seal the chip, the plasma head will activate once more and treat the PDMS on the enclosure. The plasma treatment allows for a seal on PDMS–PDMS contact between the lid and the base of the enclosure.

Step 7: After treatment, the lid is placed onto the base enclosure then incubated.

Figure 30(A) is schematic illustrating the fabrication steps of developing the cell-on-a-chip device. Figure 30(C) shows an image of the fabricated microchannels within the slot of the PDMS enclosure and Figure 30(D) shows an image of the completed cell- laden microfluidic chip with the lid and its inlet and outlet ports. Figure 31 presents a flow chart illustrating the fabrication processes of the integrated system to develop a biological microfluidic chip.
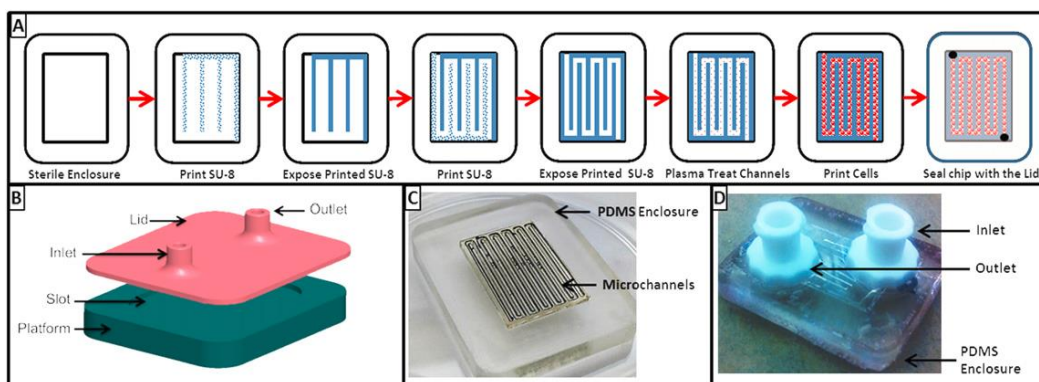
Figure 30. (A) A schematic illustrating the fabrication steps of developing the cell-laden microfluidic chip, (B) a model of the PDMS enclosure, (C) an image of the fabricated microchannels within the slot of the PDMS enclosure, (D) an image of the completed cell-laden microfluidic chip with the lid and its inlet and outlet ports.
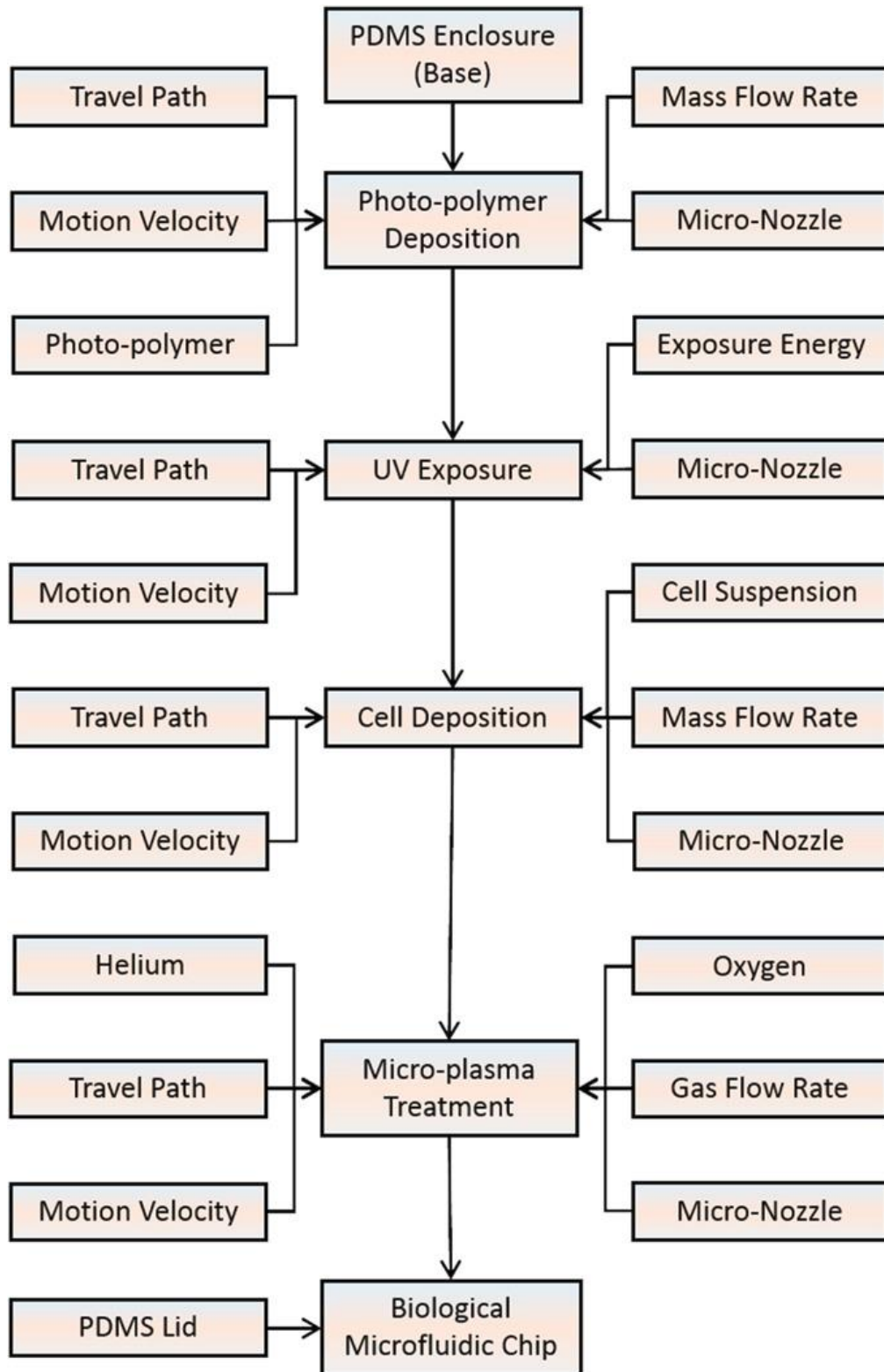
Figure 31. Flow chart illustrating the fabrication process of a biological microfluidic chip using the integrative fabrication process.

5.3.1   Internal Architecture Validation

The morphology of the cells within the microchannels was visualized by confocal microscopy and scanning electron microscopy (SEM). Cell morphology and the internal micro-architecture were evaluated using an FEI/Philips XL-30 field emission environmental scanning electron microscope. The images obtained from the SEM were taken using a beam intensity of 2 kV and gaseous secondary electron detectors of 1.3 Torr. Prior to SEM investigation of the micro-architecture and cell morphology, the lid of the chips was sectioned using a sharp straight razor. After sectioning, the chip was then prepared by first fixing the cells in 2% glutaraldehyde for 2 h followed by a dehydration process of submerging the sample in 50%, 60%, 70%, 80%, 90%, and 100% ethanol in series for 10 min. Samples were stored in a 4 °C refrigerator overnight, then splutter-coated with platinum (approximately 10 nm thick) for visualization. All biological investigation data are expressed as the mean ± standard deviation for sample size of 4 (n = 4).

Utilizing the above process parameters with a 250 μm nozzle on the biologics head and a 500 μm nozzle on the photo-polymer head, UV head, and plasma head; a sinusoidal microfluidic chip with a channel width and height of 500 μm each was fabricated. Since the biologics head prints inside of the microchannels, the nozzle diameter has to be smaller than the width of the channel. The 250 μm nozzle allowed for spatial control of the printed cells inside of the 500 μm microchannels. To check for structural integrity of the fabricated microchannels,

and SEM characterization was conducted after the SU-8 was exposed with the UV head. Figure 32 shows the results of this investigation. Figure 32(A) shows the uniformity of the channels while Figure 32(B) shows the end of the microchannel in which the direction changes from a horizontal channel to a vertical channel then back to a horizontal channel. Both SEM images prove that the chip is of the specified dimensions.
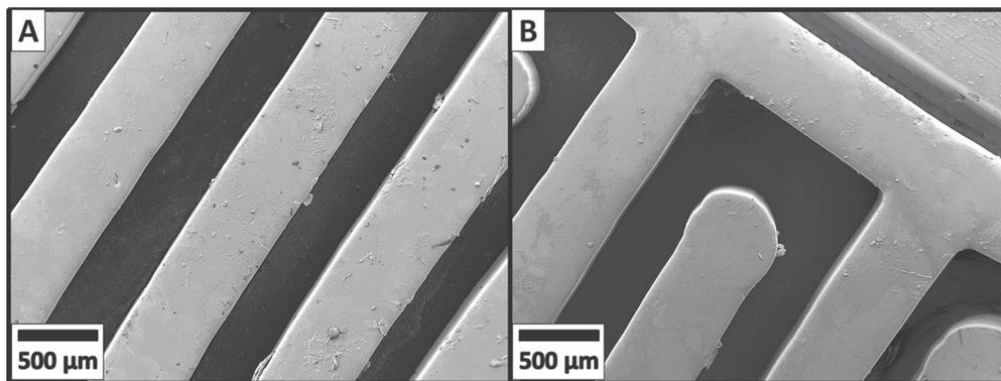
Figure 32. (A) SEM image showing the uniformity of the fabricated microchannels, (B) SEM image showing the end of the microchannel in which the direction changes from a horizontal channel to a vertical channel then back to a horizontal channel.

5.4   Cell Integration, Attachment, Proliferation, and Tracking

Cells are labeled with Qtracker® cell labeling kit to track cells in co-cultures within the microfluidics. Qtracker® cell labeling kits are designed for loading cells grown in cultures with highly fluorescent Qdot® nanocrystals. Once inside the cells, Qtracker® labels provide intense, stable fluorescence that can be traced through several generations, and are not transferred to adjacent cells in a population. Qtracker® 525 and 625 are used to label the HepG2 and MDA-MB-231 cell lines, respectively. Qtracker® 525 emission is 525 nm and excitation is 405–485 nm.

Qtracker® 625 emission is 625 nm and excitation is 405–585 nm. Prior to investigation, the working solutions were made by preparing 10 nM labeling solution, pre-mix 1 μL each of Qtracker® component A and component B in a 1.5 mL micro-centrifuge tube. Incubate for 5 min at room temperature then add 0.2 mL of fresh complete growth medium to the tube and vortex for 30 s to complete the working solution. This protocol was followed for both cell labeling kits for its correspond- ing cell type. Prior to the cells being loaded into the biologics head, each cell type was suspended in its corresponding cell labeling working solution for an incubation period of 45–60 min. After incubation, cells were washed twice with complete growth medium then re-suspended and loaded into the biologics head for printing. A fluorescence microscope and micro-plate reader (GENios, TECAN, North Carolina, USA) were used for characterization.

The Qtracker® kits allowed for tracking each cell type under a fluorescence micro- scope and the quantitative characterization of each cell type with the use of a microplate reader. Since both cell lines were mixed together and printed into the microchannels, it is expected that both cell lines integrate with each other, attach and proliferate together. Figure 33(A) is a merged fluorescence image taken through a 525 and 625 nm filter showing the MDA-MB-231 cell line in red and the HepG2 cell line in green. This image proves that both cell lines are integrated with each other. Figure 33(B) is a phase-contrast image coupled with Figure 33(A) to illustrate the cell distribution within the microchannels. Both images were taken at day 7 during the investigation. Cell distribution and active proliferation throughout

the 21 day study was collected and analyzed and is showed in Figure 33(C). As seen in Figure 33(C), both cell types have an even cell distribution throughout the chip. Also, over the 21 days, there is an increase in fluorescence intensity which demonstrates an up- regulation in cell proliferation for both cell lines.
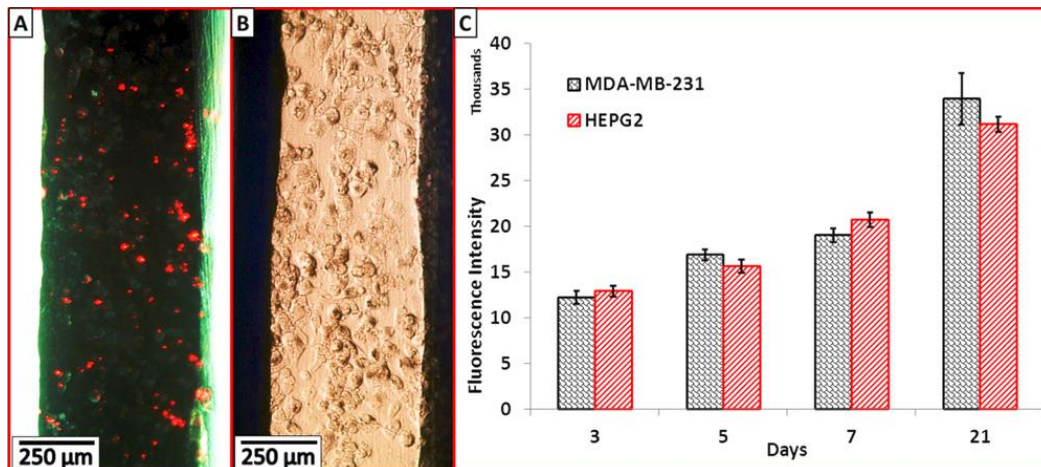
Figure 33. (A) Fluorescence image showing cell distribution and integration of the MDA-MD-231 cells (red, Qtracker® 625) and the HepG2 cells (green, Qtracker® 525) within the microchannels, (B) a phase-contrast image of the cells in the microchannel, (C) quantitative results of the cell distribution of the MDA-MB-231 and HepG2 cell lines within the microfluidic chip.

5.4.1 Evaluation of Cell Viability and Metabolic Activity

Cell viability and metabolic activity is investigated to assess the changes in function of the cells within the microchannels. The topological and chemical modification provided by microplasma may induce structural and functional changes in cellular function. A fluorometric investigation was conducted with the use of AbD SeroTEC's Alamar Blue (Ab). The cell-on-a-chip devices were washed with 1x phosphate buffered saline (PBS) by pumping the PBS through the chips

with a syringe pump at a flow rate of 30 μLh 1. 10% Ab was mixed with the co-culture medium and was pumped through the chips at 30 μL/hr until the chips were filled with the reagent. The chips were then disconnected from the syringe pump and were placed in the incubator for 4 h. After 4 h, the resulting reagent within the chips was removed from the chips and characterized with a microplate reader whose excitation and emission wavelengths were 535 and 590 nm respectively.

Ab was used as a secondary proliferation characterization method. This will further confirm the results from the Qtracker® kits. This proliferation study characterizes the total cell growth within the entire chip but does not differentiate between cells. For comparative data, two control chips were investigated where one chip was seeded with only MDA-MB-231 cells and the other was seeded with HepG2 cells. This study shows the cell proliferation within the chips and comparatively shows the effects of co-culturing these two cells in a microfluidic environment. Figure 34 shows the results of this study. The data shows that over a 21 day period under the same microfluidic environment, the MDA-MB-231 cells proliferated the fastest while the HepG2 cells had the slower proliferation rate. The chip with both cell lines started with a slow proliferation rate; however, at the end of the 21 day study, the co- culture chip had higher fluorescence intensity than the chip with the HepG2 cells. This trend demonstrates that when the two cells are coupled together, it takes a little longer for them to generate and that the environment in which both cell lines are in can thrived in. After about seven days, the proliferation trend suggests that the extra-cellular matrix created by both cell

lines allowed for an up-regulated cell proliferation trend. The results from the cell proliferation and cell tracking/cell integration investigation suggest that the co-culturing of two cell lines in a microfluidic chip with enhanced surface treatment is feasible.
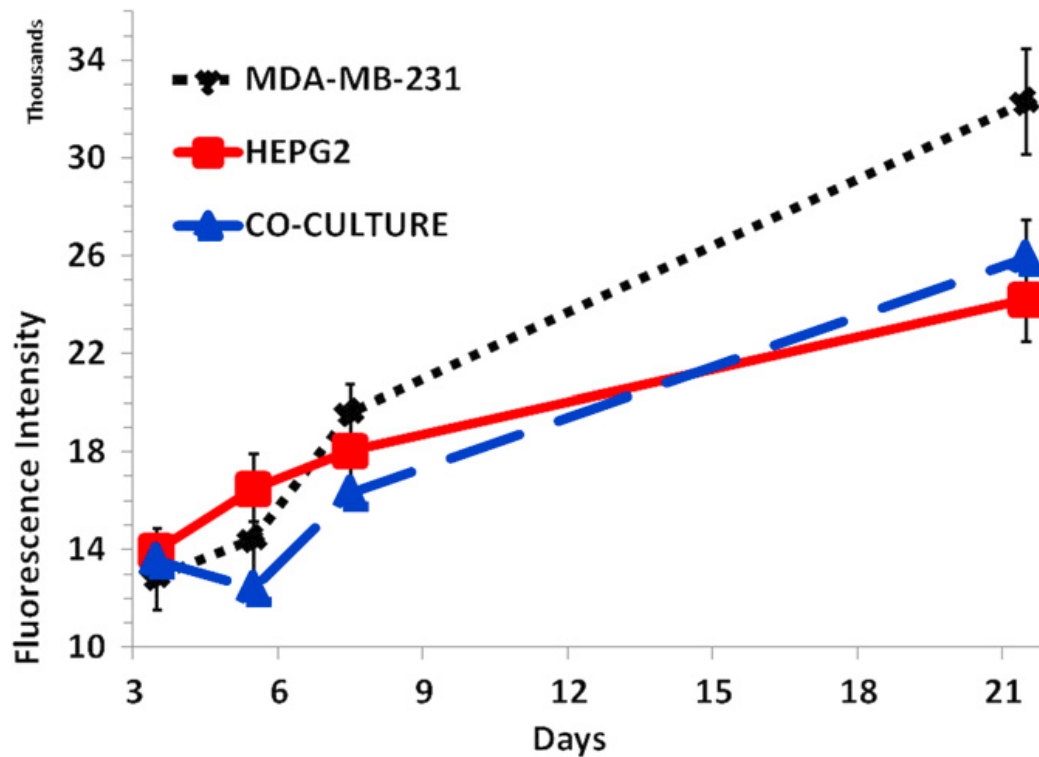
Figure 34. Results of the 21 days cell proliferation study of the MDA-MB-231 cell-laden chip (control 1), HepG2 (control 2) cell-laden chip, and the co-culture (both MDA-MB-231 and HepG2 cell lines) cell-laden chip.

5.4.2 Cell Morphology

SEM characterization provides an in-depth look of the cell morphology within the microchannels. This characterization allows for visualization of cell integration within the microchannels by their morphologies and confirms that cells

are integrated and are growing within the channels. Figure 35 shows a set of SEM images presenting an overview of the cells within the microchannels (Figure 35(A)), a close-up of the integrated cells (Figure 35(B)), and the corresponding morphologies of each cell types (Figure 35(C) and (D)). As seen in Figure 35(A) there is a uniform distribution of cells throughout the microchannels. This is the same throughout the entire chip. This image demonstrates the capabilities of the biological deposition component of the integrated system to precisely print cells in a controlled pattern. Utilizing the morphologies of the MDA-MB-231 (Figure 35(C)) and HepG2 (Figure 35(D)) cells lines with the close-up view of the cells in the microchannel (Figure 35(B)), it is clear that the two cell lines are indeed integrated throughout the chip.
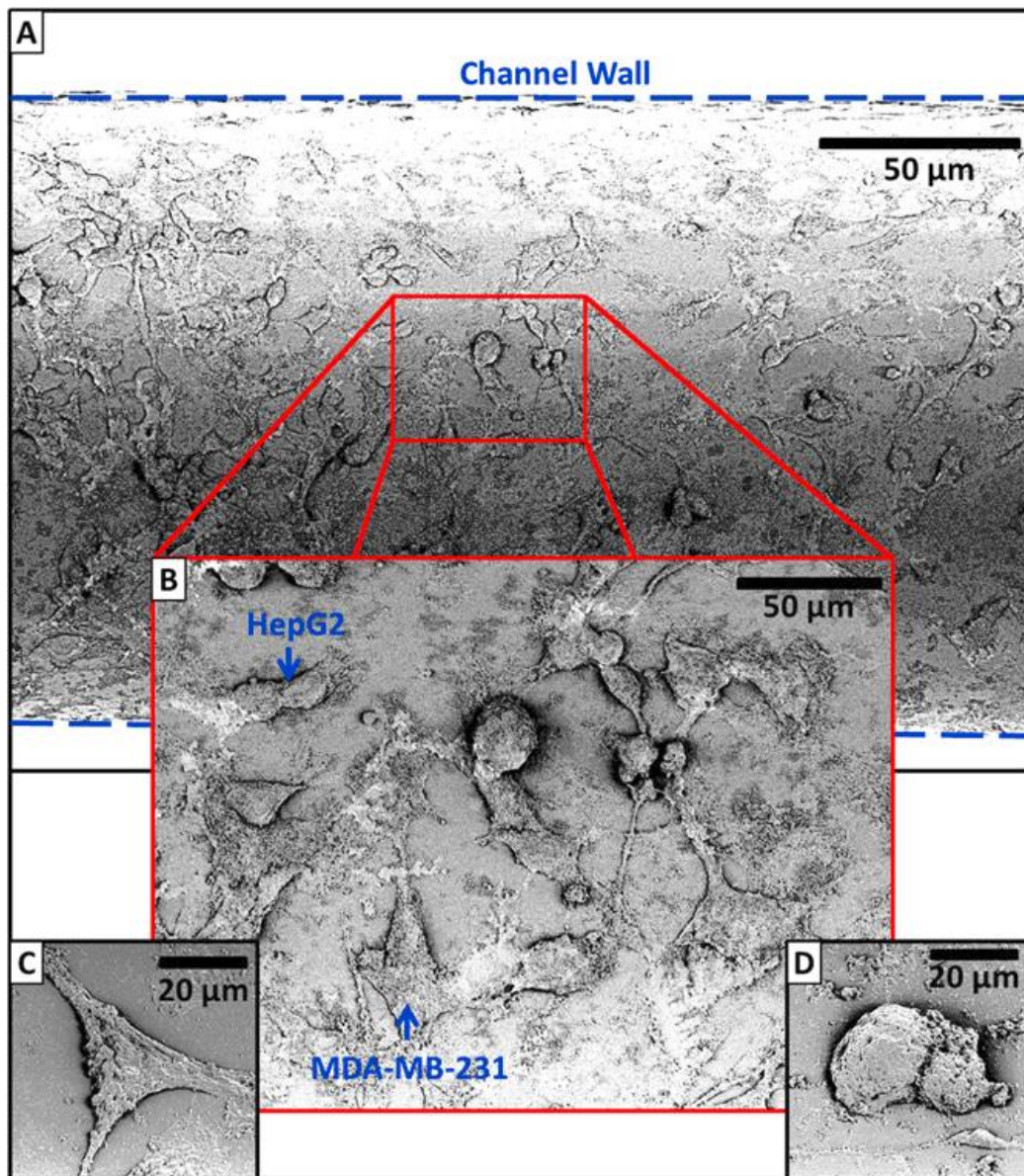
Figure 35. (A) SEM image showing an overview of the cell distribution within the microchannel, (B) SEM image showing a close-up of the cells within the microchannel, the MDA-MB-231 and HepG2 cells are labeled, (C) SEM image showing the morphology of a MDA-MB-231 cell, (D) SEM image showing the morphology of a HepG2 cell.

5.5   Limitations and other Techniques for Creating Cancer Models

The fabrication method presented in this chapter is unique and advantageous. While it allows for the fabrication of biological microfluidics without the use of harsh chemicals, it does have some limitations. The fabrication process is only utilizing one print head at a time and the microscopic nozzles only allow for the development of micro-systems only. This device cannot develop systems on the macro scale. It does have the ability to fabricate a series of micro-structures that can be summed into the macro scale; however, fabricating systems such as these can lead to prolonged fabrication time. If the systems are fabricated without cells, the lengthy fabrication time is not an issue. However, if the system has cells, the lengthy fabrication time will decrease the cell viability. As demonstrated in this chapter, the fabrication of one layer does not affect the cell viability at the end of the fabrication process. However, the introduction of a second layer will decrease the cell viability due to the use of the UV print head. Fabricating an additional layer will not lead to the demise of all the cells in the layers below, only a small fraction. The localized treatment of the UV print head is specifically developed to minimize cell death during the fabrication process such that the fabrication of advanced micro-structure. In addition to fabrication limitations, there are characterization limitations. Since the micro-systems are enclosed in PDMS, depending on the enclosure thickness and microscopy instrument, it may be difficult to qualitative characterize what's happening inside of the chip. Characterization techniques should be considered during the development of advanced micro-systems.

5.5.1 Spheroids in Suspension

Cellular spheroids are small tightly bounded cellular spheres with size ranged from 20 µm to 1 mm. These cellular aggregates are often obtained through the spontaneous tendency by buoyancy or stirring, and exogenous scaffold or matrix is usually not needed during the spheroid formation. In breast cancer study, researchers showed that human breast carcinoma cell (MDA-MB-435) would spontaneously assemble during cell aggregation [190]. Buoyancy was exploited in the "hanging-drop" technique: droplets of culture medium containing cells were suspended from microtiter plates. After several days of growth, large spheroids were obtained. Alternatively, rotational stirrers were employed for spheroids formation [191].

Besides hanging drop method, typical methods also include continuous agitation of suspension culture in a rotary cell culture vessel or a spinner flask [76], [192], culturing on cell repulsive substrates [193], and entrapment within biologically inert 3D hydrogel matrices [194]. Spinner flasks are used for culturing cells as a dynamic suspension placed in liquid media. Cells deposited in stirred-tank bioreactors were mixed by impeller to maintain a state of suspension. During the formation of spheroids, the gyratory rotation increases the fluid transport of both nutrients and waste. This technique is suitable for culturing large populations of spheroids under controlled exterior parameters with regard to oxygen, nutrient supply, and pH. To grow sensitive cells and form larger spheroid-like structures,

microcarrier beads were often used along with gyratory and spinner flasks. NASA further developed a rotating-wall vessel to stimulate microgravity which minimizes fluid turbulence and shear forces compared to the spinner flask. The fluid shear force can be an influential stimulus to certain type of cells, e.g., osteoblasts [195]. The low shear environment was a great advantage for mitigating the negative effect of fluid turbulence, which was known to damage fragile cells by inducing membrane breakage and affecting metabolism [196].

Spheroids are commonly used in clinical research, especially as models of small solid tumors. Pioneer studies on growth of mammalian tumor spheroids dated back from 1980s [197], [198]. Since the tumor-stromal interactions in 3D co-culture spheroids provide important clues to the behavior of capillaries in tumor, multicellular spheroids mixing immortalized cells and various types of stromal cells provided better mimicry of natural physiology than monocellular spheroids. The symmetrical spherical geometry benefits modeling and analysis of dynamic processes, and automation in fabrication of spheroid aggregation. Besides, there was no need for bioactive scaffolds, as a result cellular spheroids-based assays have a great potential to be scaled up to rapid, high-throughput analysis [6]. These limitations includes; the inability to capture the interactions that occur *in vivo*, for example, host immune reactions and angiogenesis; and challenges in controlling the size of spheroid [199]. With current advances in microscopy imaging like light sheet fluorescence microscopy [200], cellular spheroids regain the importance as an *in vitro* cancer model, especially for preclinical anti-cancer drug screening.

5.5.2 Gel Embedding

Biological gels, which are traditionally used to encapsulate a small tumor explant with a gel matrix, are developed as substrate to better mimic *in vivo* microenvironment since they can provide rich network of ECM signals. Contrary to some traditional spheroids which lack adhesion to a surface, gels embedded cells have both cell-cell and cell-matrix attachments [87]. Gel embedding could help promote cancer cell proliferation rate [201], wound tissue expansion, and angiogenesis (with fibroblast embedded) [202]. Moreover, it could also change cancer cell migration modes with certain *in vivo* fidelity [203].

Collagen, alginate and Matrigel are most commonly used gel materials in constructing 3D cellular models. Researchers often mix two or three different gels to form composite gel matrix to manipulate gel concentration, composition and mechanical properties, which would further influence tumor cell attachment and migratory capabilities. Comparison of gel embedding protocols was discussed for breast cell analysis [204]. Krause et al. developed a co-culture system of human epithelial cells and fibroblast cells in type I collagen and Matrigel-collagen matrix, respectively, to resemble the mammary gland structures found *in vivo*. These results illustrate the contribution of fibroblasts to the formation of ductal structures [40]. Other combination such as a mix of hyaluronic acid derivatives with cells was successful in evaluating the efficacy of anti-cancer drugs [77].

Additionally, gel embedding method can be associated with microfluidic device to create multicellular co-culture system to eliminate the transport limitations as seen in traditional spheroid culture. For example, Jeon et al. reported a novel microfluidic device consisting of a set of parallel channels separated by an array of posts which allow selective filling (collagen, fibrin, Matrigel) of individual channels for co-culture. Macrophage cells (RAW 264.1) were found to permeate into neighboring gels containing (MDA-MB-231) metastatic breast cancer cells, which demonstrated the potential of gel embedding combined with microfluidic technology for 3D cancer model establishment [205]. Still, environmental signals like substrate morphology (2D vs 3D) and pH would account for change in cellular behaviors [206].

5.5.3   Scaffold Based Models

Engineered scaffolds have been employed as a biomaterial-based approach for simulating the extracellular matrix and providing physical/structural support. These structures constructed from biocompatible synthetic polymers can be used as a support matrix for *in vitro* cell culture as well as *in vivo* tissue regeneration [207]. The application of microfabrication techniques to novel biomaterials provides a well-controlled approach to develop functional microvasculature that mimic native organ and tissues [79]. Freeform fabrication is a rapid manufacturing technique to fabricate 3D porous bioactive scaffolds with complex architectural structures and well-defined material properties using Computer-Aided-Design (CAD) models. Dhiman et al. constructed a 3D chitosan scaffold and seeded with human breast

cancer cell line (MCF-7). Results showed that more lactate and glucose were produced from cells grown on chitosan scaffold than cells grown on 2D culture plate [38], [39]. Based on previous work, Zhang et al. constructed a 3D chitosan-alginate (CA) scaffold to promote the conversion of cultured glioma cells to a more malignant in vivo-like phenotype, with results indicating that human glioma cells (U-87 MG and U-118 MG) showed remarkably higher malignancy when cultured in CA scaffolds [208].

Another technique to fabricate porous 3D scaffolds is electrospinning, which creates non-woven mats volume as ECM analogue scaffolds. By applying high voltage on flowing polymer solution, polarity is increased inside the polymer. While polymer solution is extruded from a capillary nozzle, a collector with an opposite polarity rotates for polymer deposition. On the fabricated electrospun fibers, cells are broadly seeded thanks to a high surface area to volume feature. The fibers have micrometer to submicrometer diameters ranging from 100 to 5000 nm due to different settings of processing parameters, which include applied voltage, flow rate, and capillary-collector distance [209]. One major advantage of electrospinning is the cost efficiency for using very small quantities of polymers. A second advantage is that additional components such as co-polymers and growth factors can be added to the polymer solution in the preparation process and then be incorporated into the electrospun fibers [79]. A coaxial nozzle was designed to mix the living cells with Poly(ethylene oxide) (PEO) and Glutaraldehyde (GTA) during electrospinning process while still maintaining certain cell viability. [210]. This

type of scaffold was widely used in drug screening research, thanks to its inherent high porosity. A set of nanofiber scaffolds composed of Poly(3-hydroxybutyrate-co-3-hydroxyvalerate) (PHBV) with collagen peptide, were fabricated to test the sensitivity of cancer cells to anticancer drugs, ; as a result, higher concentrations of anticancer drugs were required to achieve a comparable cytotoxic effect in 3D nanofiber scaffolds [211]. In another study, a 3D electrospun PCL scaffold cultured with Ewing sarcoma cells succeeded in reproducing several presumed mechanisms of drug resistance, in accordance with the clinical data. Apart from organic biopolymers, recent research on organic-inorganic hybrid bioceramics showed that growth factors could be strongly grafted to these materials instead of traditional coating [212]. This indicates a potential application for cancer scaffold models. Therefore the scaffold based models is a valuable tool to investigate anti-cancer drug mechanisms.

CHAPTER 6: CONCLUSION

6.1   Research Summary

This study focus on developing experimental techniques, and computational tools that allow for the design surface properties of engineered three-dimensional structures to manipulate and control the cellular functions. A novel freeform microplasma generated maskless surface patterning process was developed to create spatially defined topological and chemical features on biopolymer surface. Specifically, in this study, global and localized plasma functionalization were applied on polycaprolactone (PCL) samples to introduce biophysical, biochemical, biological and structural cues to enhance cellular response including attachment, proliferation and differentiation. In addition, a plasma computational-statistical model was developed to predict the changes in biopolymer surface physicochemical properties following the oxygen based plasma surface functionalization. Furthermore, an integrated system including localized plasma functionalization is specifically designed for the development of biologically inspired cell-on-a-chip devices. The capabilities, benefits, and challenges of the integrated multifunctional biofabrication system to develop cell-on-a-chip device is also illustrated.

6.2   Research Contributions

The research contributions are summarized as follows:

1. The effect of oxygen-based global plasma surface modification of polycaprolactone (PCL) samples on cellular functions was investigated

as a primer to develop a localized plasma treatment system. This study illustrated the manufacturing and oxygen-based plasma modification processes of PCL samples. The methods in surface and biological characterization of plasma modified PCL sample were described in details. Changes in surface physicochemical properties by oxygen-based plasma modification improved cell-surface interaction. An atmospheric-pressure microplasma jet based on dielectric barrier discharge (DBD) was integrated to a patented cell printing system which allows biologics deposition in the x-y-z directions at various trajectory presets. Several characterization and biological studies indicate that the localized microplasma treatment improved surface morphology and chemistry, caused an increase in hydrophilicity. Improved cell viability and proliferation were observed only on selective regions, as compared to global plasma treatment.

2. A novel atmospheric-pressure microplasma jet based on dielectric barrier discharge (DBD) was integrated to a patented cell printing system. The integrated system allows not only biologics printing but also plasma deposition in the x-y-z directions at various trajectory presets. Several characterization and biological studies indicate that the localized microplasma treatment improved surface morphology and chemistry, caused an increase in hydrophilicity, which was in line with the results from global plasma treatment studies. Improved cell viability and proliferation were observed only on selective regions, as compared

to global plasma treatment. This unique system enables researchers to produce surface patterning without using costly and hazardous chemical masks for cell printing applications.

3. A two-dimensional (2D) plasma computational-statistical model of the atmospheric-pressure microplasma jet was developed to predict surface condition after localized plasma treatment using aforementioned system. The effect of mass species transport to polymer surface was investigated by coupling an incompressible fluid dynamics model to a plasma kinetics model. The modeling results involve tracking the different physical processes during microplasma discharge, such as discharge breakdown, radical chemistry, and surface kinetics. Oxygen production rate was computed from this model to link with water contact angle changes, and further to predict surface condition with input of different system parameters.

4. Four independent biofabrication techniques were integrated in a novel automation system to develop cell-on-a-chip devices. This study also illustrated the capabilities, benefits, and challenges of the integrated multifunctional biofabrication system. Several biological investigations were presented to demonstrate the system's capabilities to produce advance functional cancer cell-on-a-chip device. The novel integrated multifunctional fabrication system eliminates the limitations of conventional photo-lithography and provides researchers with the

capabilities to develop advantageous cell-on-a-chip and organ-on-a-chip devices on a single platform.

6.3   Future Work

The localized microplasma surface functionalization system succeeded in creating maskless patterns for various cell printing applications. It is also possible to generate gradient polymer surfaces by adjusting nozzle moving speed and height, contrary to a common method as applying a specially designed mask [213]. Preliminary study results showed gradient distribution of water contact angles along microplasma treated lines on PCL surfaces. This part of work has been presented at International Conference on Biofabrication 2014 in Korea, but an intensive study has yet to be conducted.

LIST OF REFERENCES

[1]   C. Wang, Z. Tang, Y. Zhao, R. Yao, L. Li, and W. Sun, "Three-dimensional in vitro cancer models: a short review.," *Biofabrication*, vol. 6, p. 22001, 2014.

[2]   P. Issues and I. O. The, "Why Do So Many Phase 3 Clinical Trials Fail ?," *Pharm. Res.*, pp. 1–46, 2009.

[3]   M. L. Shuler, A. Ghanem, D. Quick, M. C. Wong, and P. Miller, "A self-regulating cell culture analog device to mimic animal and human toxicological responses," in *Biotechnology and Bioengineering*, 1996, vol. 52, no. 1, pp. 45–60.

[4]   M. J. Powers, K. Domansky, M. R. Kaazempur-Mofrad, A. Kalezi, A. Capitano, A. Upadhyaya, P. Kurzawski, K. E. Wack, D. B. Stolz, R. Kamm, and L. G. Griffith, "A microfabricated array bioreactor for perfused 3D liver culture," *Biotechnol. Bioeng.*, vol. 78, no. 3, pp. 257–269, 2002.

[5]   P. A. Kenny and M. J. Bissell, "Targeting TACE-dependent EGFR ligand shedding in breast cancer," *J. Clin. Invest.*, vol. 117, no. 2, pp. 337–345, 2007.

[6]   F. Pampaloni, E. H. K. Stelzer, S. Leicht, and M. Marcello, "Madin-Darby canine kidney cells are increased in aerobic glycolysis when cultured on flat and stiff collagen-coated surfaces rather than in physiological 3-D cultures," *Proteomics*, vol. 10, no. 19, pp. 3394–3413, 2010.

[7]   J. Bin Kim, "Three-dimensional tissue culture models in cancer biology," *Semin. Cancer Biol.*, vol. 15, no. 5, pp. 365–377, Oct. 2005.

[8]   K. Mostov, T. Su, and M. ter Beest, "Polarized epithelial membrane traffic: conservation and plasticity.," *Nat. Cell Biol.*, vol. 5, no. 4, pp. 287–293, 2003.

[9]   F. Pampaloni, E. G. Reynaud, and E. H. K. Stelzer, "The third dimension bridges the gap between cell culture and live tissue," *Nat. Rev. Mol. Cell Biol.*, vol. 8, no. 10, pp. 839–845, Oct. 2007.

[10]   J. Yang, J. Bei, and S. Wang, "Enhanced cell affinity of poly (D,L-lactide) by combining plasma treatment with collagen anchorage.," *Biomaterials*, vol. 23, no. 12, pp. 2607–14, Jun. 2002.

[11]   J. H. Lee, J. W. Lee, G. Khang, and H. B. Lee, "Interaction of cells on chargeable functional group gradient surfaces.," *Biomaterials*, vol. 18, no. 4, pp. 351–8, Feb. 1997.

[12]   E. D. Yildirim, D. Pappas, S. Güçeri, and W. Sun, "Enhanced cellular functions on polycaprolactone tissue scaffolds by o 2 plasma surface modification," *Plasma Process. Polym.*, vol. 8, no. 3, pp. 256–267, 2011.

[13]   N. Huang, Y. X. Leng, P. Yang, J. Y. Chen, H. Sun, G. J. Wan, J. Wang, P. K. Chu, and I. G. Brown, "Plasma surface modification of biomaterials applied for cardiovascular devices," *30th Int. Conf. Plasma Sci. 2003. ICOPS 2003. IEEE Conf. Rec. - Abstr.*, vol. 36, p. 439, 2002.

[14]   C. Oldham, "Applications of atmospheric plasmas," 2009.

[15]   C.-M. Chan, T.-M. Ko, and H. Hiraoka, "Polymer surface modification by plasmas and photons," *Surf. Sci. Rep.*, vol. 24, no. 1–2, pp. 1–54, May 1996.

[16]   P. Rajasekaran, "Atmospheric-pressure dielectric barrier discharge (DBD) in air: Plasma characterisation for skin therapy," 2011.

[17]   E. D. Yildirim, H. Ayan, V. N. Vasilets, A. Fridman, S. Guceri, and W. Sun, "Effect of Dielectric Barrier Discharge Plasma on the Attachment and Proliferation of Osteoblasts Cultured over Poly(ε-caprolactone) Scaffolds," *Plasma Process. Polym.*, vol. 5, no. 1, pp. 58–66, Jan. 2008.

[18]   B. Held, "Analytic calculations of ozone concentration in an oxygen-fed DBD cylindrical ozonizer," *Eur. Phys. J. Appl. Phys.*, 2000.

[19]   C. Soria, F. Pontiga, and a Castellanos, "Plasma chemical and electrical modelling of a negative DC corona in pure oxygen," *Plasma Sources Sci. Technol.*, vol. 13, no. 1, pp. 95–107, Feb. 2004.

[20]   Y. Golubovskii and V. Maiorov, "Modelling of the homogeneous barrier discharge in helium at atmospheric pressure," *J. Phys. D …*, vol. 39, 2003.

[21]   Y. V Yurgelenas and H.-E. Wagner, "A computational model of a barrier discharge in air at atmospheric pressure: the role of residual surface charges in microdischarge formation," *J. Phys. D. Appl. Phys.*, vol. 39, no. 18, pp. 4031–4043, Sep. 2006.

[22]   D. X. Liu, P. Bruggeman, F. Iza, M. Z. Rong, and M. G. Kong, "Global model of low-temperature atmospheric-pressure He + H 2 O plasmas," *Plasma Sources Sci. Technol.*, vol. 19, no. 2, p. 25018, Apr. 2010.

[23]   Q. Wang, D. J. Economou, and V. M. Donnelly, "Simulation of a direct current microplasma discharge in helium at atmospheric pressure," *J. Appl. Phys.*, vol. 100, no. 2, p. 23301, 2006.

[24]   J. He and Y. T. Zhang, "Modeling study on the generation of reactive oxygen species in atmospheric radio-frequency helium-oxygen discharges," *Plasma*

Process. Polym., vol. 9, no. 9, pp. 919–928, 2012.

[25] A. N. Bhoj, "Multiscale simulation of atmospheric pressure pulsed discharges used in polymer surface functionalization," University of Illinois at Urbana-Champaign, 2006.

[26] World-Health-Organization, "QUICK CANCER FACTS," 2011. [Online]. Available: http://www.who.int/cancer/en/.

[27] T. Vargo-Gogola and J. M. Rosen, "Modelling breast cancer: one size does not fit all," *Nat Rev Cancer*, vol. 7, no. 9, pp. 659–672, Sep. 2007.

[28] J. Bin Kim, R. Stein, and M. J. O'Hare, "Three-dimensional in vitro tissue culture models of breast cancer - a review," *Breast Cancer Res. Treat.*, vol. 85, no. 3, pp. 281–291, Jun. 2004.

[29] S. L. Schor, A. M. Grey, M. Picardo, A. M. Schor, A. Howell, I. Ellis, and G. Rushton, "Heterogeneity amongst fibroblasts in the production of Migration Stimulating Factor (MSF) - implications for cancer pathogenesis," *Cell Motil. Factors*, vol. 59, pp. 127–146, 1991.

[30] V. Dangles, P. Validire, M. Wertheimer, S. Richon, C. Bovin, D. Zeliszewski, G. Vallancien, and D. Bellet, "Impact of human bladder cancer cell architecture on autologous T-lymphocyte activation," *Int. J. Cancer*, vol. 98, no. 1, pp. 51–56, 2002.

[31] C. Lottner, R. Knuechel, G. Bernhardt, and H. Brunner, "Distribution and subcellular localization of a water-soluble hematoporphyrin-platinum(II) complex in human bladder cancer cells," *Cancer Lett.*, vol. 215, no. 2, pp. 167–177, 2004.

[32] H. J. Boxberger and T. F. Meyer, "A new method for the 3-d in-vitro growth of human rt112 bladder-carcinoma cells using the alginate culture technique," *Biol. Cell*, vol. 82, no. 2–3, pp. 109–119, 1994.

[33] J. P. Burgues, L. Gomez, J. L. Pontones, C. D. Vera, J. F. Jimenez-Cruz, and M. Ozonas, "A chemosensitivity test for superficial bladder cancer based on three-dimensional culture of tumour spheroids," *Eur. Urol.*, vol. 51, no. 4, pp. 962–970, 2007.

[34] A. Schaaf, T. McNealy, A. Steidler, P. Alken, and M. S. Michel, "A new ex-vivo 3D bladder matrix model for standardised evaluation of urothelial transfection methods," *Aktuelle Urol.*, vol. 34, no. 3, pp. 172–175, 2003.

[35] T. E. Wiese, L. A. Polin, E. Palomino, and S. C. Brooks, "Induction of the estrogen specific mitogenic response of MCF-7 cells by selected analogues of estradiol-17 beta: A 3D QSAR study," *J. Med. Chem.*, vol. 40, no. 22, pp.

3659–3669, 1997.

[36] M. Anders, R. Hansen, R. X. Ding, K. A. Rauen, M. J. Bissell, and W. M. Korn, "Disruption of 3D tissue integrity facilitates adenovirus infection by deregulating the coxsackievirus and adenovirus receptor," *Proc. Natl. Acad. Sci. U. S. A.*, vol. 100, no. 4, pp. 1943–1948, 2003.

[37] L. J. Wilmes, M. G. Pallavicini, L. M. Fleming, J. Gibbs, D. H. Wang, K. L. Li, S. C. Partridge, R. G. Henry, D. R. Shalinsky, D. Hu-Lowe, J. W. Park, T. M. McShane, Y. Lu, R. C. Brasch, and N. M. Hylton, "AG-013736, a novel inhibitor of VEGF receptor tyrosine kinases, inhibits breast cancer growth and decreases vascular permeability as detected by dynamic contrast-enhanced magnetic resonance imaging," *Magn. Reson. Imaging*, vol. 25, no. 3, pp. 319–327, 2007.

[38] H. K. H. K. Dhiman, a R. A. R. Ray, and A. K. A. K. Panda, "Characterization and evaluation of chitosan matrix for in vitro growth of MCF-7 breast cancer cell lines," *Biomaterials*, vol. 25, no. 21, pp. 5147–5154, Sep. 2004.

[39] H. K. Dhiman, A. R. Ray, and A. K. Panda, "Three-dimensional chitosan scaffold-based MCF-7 cell culture for the determination of the cytotoxicity of tamoxifen," *Biomaterials*, vol. 26, no. 9, pp. 979–986, Mar. 2005.

[40] S. Krause, M. V Maffini, A. M. Soto, and C. Sonnenschein, "A novel 3D in vitro culture model to study stromal-epithelial interactions in the mammary gland," *Tissue Eng. Part C-Methods*, vol. 14, no. 3, pp. 261–271, Sep. 2008.

[41] K. J. Martin, D. R. Patrick, M. J. Bissell, and M. V Fournier, "Prognostic Breast Cancer Signature Identified from 3D Culture Model Accurately Predicts Clinical Outcome across Independent Datasets," *PLoS One*, vol. 3, no. 8, p. e2994, 2008.

[42] Q. W. Li, A. B. Chow, and R. R. Mattingly, "Three-Dimensional Overlay Culture Models of Human Breast Cancer Reveal a Critical Sensitivity to Mitogen-Activated Protein Kinase Kinase Inhibitors," *J. Pharmacol. Exp. Ther.*, vol. 332, no. 3, pp. 821–828, 2010.

[43] M. Pickl and C. H. Ries, "Comparison of 3D and 2D tumor models reveals enhanced HER2 activation in 3D associated with an increased response to trastuzumab," *Oncogene*, vol. 28, no. 3, pp. 461–468, 2009.

[44] S. J. Sequeira, A. C. Ranganathan, A. P. Adam, B. V Iglesias, E. F. Farias, and J. A. Aguirre-Ghiso, "Inhibition of Proliferation by PERK Regulates Mammary Acinar Morphogenesis and Tumor Formation," *PLoS One*, vol. 2, no. 7, p. e615, 2007.

[45] M. Takeda, H. Tada, H. Higuchi, Y. Kobayashi, M. Kobayashi, Y. Sakurai, T. Ishida, and N. Ohuchi, "In vivo single molecular imaging and sentinel node navigation by nanotechnology for molecular targeting drug-delivery systems and tailor-made medicine," *Breast Cancer*, vol. 15, no. 2, pp. 145–152, 2008.

[46] H. J. Zhang, G. Liu, M. Dziubinski, Z. Q. Yang, S. P. Ethier, and G. J. Wu, "Comprehensive analysis of oncogenic effects of PIK3CA mutations in human mammary epithelial cells," *Breast Cancer Res. Treat.*, vol. 112, no. 2, pp. 217–227, 2008.

[47] N. Shimony, I. Avrahami, R. Gorodetsky, G. Elkin, K. Tzukert, L. Zangi, L. Levdansky, L. Krasny, and Y. S. Haviv, "A 3D rotary renal and mesenchymal stem cell culture model unveils cell death mechanisms induced by matrix deficiency and low shear stress," *Nephrol. Dial. Transplant.*, vol. 23, no. 6, pp. 2071–2080, 2008.

[48] S. H. J. Kim, S. Park, K. Mostov, J. Debnath, and C. A. Hunt, "Computational investigation of epithelial cell dynamic phenotype in vitro," *Theor. Biol. Med. Model.*, vol. 6, p. 8, Jan. 2009.

[49] G. J. Steyer, D. Roy, O. Salvado, M. E. Stone, and D. L. Wilson, "Removal of Out-of-Plane Fluorescence for Single Cell Visualization and Quantification in Cryo-Imaging," *Ann. Biomed. Eng.*, vol. 37, no. 8, pp. 1613–1628, 2009.

[50] M. B. Vaughan, R. D. Ramirez, W. E. Wright, J. D. Minna, and J. W. Shay, "A three-dimensional model of differentiation of immortalized human bronchial epithelial cells," *Differentiation*, vol. 74, no. 4, pp. 141–148, 2006.

[51] J. Jakubowicz-Gil, R. Paduch, A. Gawron, and M. Kandefer-Szerszen, "The effect of heat shock, cisplatin, etoposide and quercetin on Hsp27 expression in human normal and tumour cells," *Folia Histochem. Cytobiol.*, vol. 40, no. 1, pp. 31–35, 2002.

[52] M. D. Martin, B. Fingleton, C. C. Lynch, S. Wells, J. O. McIntyre, D. W. Piston, and L. M. Matrisian, "Establishment and quantitative imaging of a 3D lung organotypic model of mammary tumor outgrowth," *Clin. Exp. Metastasis*, vol. 25, no. 8, pp. 877–885, 2008.

[53] Z. H. Wang, C. M. Birch, J. Sagotsky, and T. S. Deisboeck, "Cross-scale, cross-pathway evaluation using an agent-based non-small cell lung cancer model," *Bioinformatics*, vol. 25, no. 18, pp. 2389–2396, 2009.

[54] Y. Zhao, N. Guo, L. G. Lou, Y. W. Cong, L. Y. Peng, and Q. S. Zhao, "Synthesis, cytotoxic activity, and SAR analysis of the derivatives of taxchinin A and brevifoliol," *Bioorg. Med. Chem.*, vol. 16, no. 9, pp. 4860–

4871, 2008.

[55] X. Y. Xu, G. H. Yang, H. L. Zhang, and G. D. Prestwich, "Evaluating dual activity LPA receptor pan-antagonist/autotaxin inhibitors as anti-cancer agents in vivo using engineered human tumors," *Prostaglandins Other Lipid Mediat.*, vol. 89, no. 3–4, pp. 140–146, 2009.

[56] X. Y. Xu and G. D. Prestwich, "Inhibition of Tumor Growth and Angiogenesis by a Lysophosphatidic Acid Antagonist in an Engineered Three-Dimensional Lung Cancer Xenograft Model," *Cancer*, vol. 116, no. 7, pp. 1739–1750, Apr. 2010.

[57] S. Hehlgans, I. Lange, I. Eke, and N. Cordes, "3D cell cultures of human head and neck squamous cell carcinoma cells are radiosensitized by the focal adhesion kinase inhibitor TAE226," *Radiother. Oncol.*, vol. 92, no. 3, Sp. Iss. SI, pp. 371–378, Sep. 2009.

[58] H. A. Kenny, T. Krausz, S. D. Yamada, and E. Lengyel, "Use of a novel 3D culture model to elucidate the role of mesothelial cells, fibroblasts and extra-cellular matrices on adhesion and invasion of ovarian cancer cells to the omentum," *Int. J. Cancer*, vol. 121, no. 7, pp. 1463–1472, 2007.

[59] H. A. Kenny, S. Kaur, L. M. Coussens, and E. Lengyel, "The initial steps of ovarian cancer cell metastasis are mediated by MMP-2 cleavage of vitronectin and fibronectin," *J. Clin. Invest.*, vol. 118, no. 4, pp. 1367–1379, 2008.

[60] M. Zietarska, C. M. M. Maugard, A. Filali-Mouhim, M. Alam-Fahmy, P. N. N. Tonin, D. M. M. Provencher, and A. M. M. Mes-Masson, "Molecular description of a 3D in vitro model for the study of epithelial ovarian cancer (EOC)," *Mol. Carcinog.*, vol. 46, no. 10, pp. 872–885, 2007.

[61] H. A. Kenny and E. Lengyel, "MMP-2 functions as an early response protein in ovarian cancer metastasis," *Cell Cycle*, vol. 8, no. 5, pp. 683–688, 2009.

[62] B. A. Benayoun, S. Caburet, A. Dipietromaria, A. Georges, B. D'Haene, P. J. E. Pandaranayaka, D. L'Hote, A. L. Todeschini, S. Krishnaswamy, M. Fellous, E. De Baere, and R. A. Veitia, "Functional Exploration of the Adult Ovarian Granulosa Cell Tumor-Associated Somatic FOXL2 Mutation p.Cys134Trp (c.402C > G)," *PLoS One*, vol. 5, no. 1, p. e8789, 2010.

[63] A. Shikanov, M. Xu, T. K. Woodruff, and L. D. Shea, "Interpenetrating fibrin-alginate matrices for in vitro ovarian follicle development," *Biomaterials*, vol. 30, no. 29, pp. 5476–5485, Oct. 2009.

[64] D. Loessner, K. S. Stok, M. P. Lutolf, D. W. Hutmacher, J. a Clements, and S. C. Rizzi, "Bioengineered 3D platform to explore cell-ECM interactions

and drug resistance of epithelial ovarian cancer cells," *Biomaterials*, vol. 31, no. 32, pp. 8494–8506, Nov. 2010.

[65] M. V Barbolina, B. P. Adley, L. D. Shea, and M. S. Stack, "Wilms tumor gene protein 1 is associated with ovarian cancer metastasis and modulates cell invasion," *Cancer*, vol. 112, no. 7, pp. 1632–1641, 2008.

[66] A. Abu-Yousif, I. Rizvi, C. Evans, J. Celli, and T. Hasan, "PuraMatrix Encapsulation of Cancer Cells," *J Vis Exp*, no. 34, p. 1692, 2009.

[67] S. Seibold, C. Rudroff, M. Weber, J. Galle, C. Wanner, and M. Marx, "Identification of a new tumor suppressor gene located at chromosome 8p21.3-22," *Faseb J.*, vol. 17, no. 6, pp. 1180–1182, 2003.

[68] J. J. Grzesiak and M. Bouvet, "Determination of the ligand-binding specificities of the alpha(2)beta(1) and alpha(1)beta(1) integrins in a novel 3-dimensional in vitro model of pancreatic cancer," *Pancreas*, vol. 34, no. 2, pp. 220–228, 2007.

[69] G. O. Ceyhan, I. E. Demir, B. Altintas, U. Rauch, G. Thiel, M. W. Muller, N. A. Giese, H. Friess, and K. H. Schafer, "Neural invasion in pancreatic cancer: A mutual tropism between neurons and cancer cells," *Biochem. Biophys. Res. Commun.*, vol. 374, no. 3, pp. 442–447, 2008.

[70] S. Hehlgans, I. Eke, K. Storch, M. Haase, G. B. Baretton, and N. Cordes, "Caveolin-1 mediated radioresistance of 3D grown pancreatic cancer cells," *Radiother. Oncol.*, vol. 92, no. 3, Sp. Iss. SI, pp. 362–370, 2009.

[71] D. Bello-Deocampo, H. K. Kleinman, N. D. Deocampo, and M. M. Webber, "Laminin-1 and alpha 6 beta 1 integrin regulate acinar morphogenesis of normal and malignant human prostate epithelial cells," *Prostate*, vol. 46, no. 2, pp. 142–153, 2001.

[72] F. S. Jin, Z. H. Xie, C. J. Kuo, L. W. K. Chung, and C. L. Hsieh, "Cotargeting tumor and tumor endothelium effectively inhibits the growth of human prostate cancer in adenovirus-mediated antiangiogenesis and oncolysis combination therapy," *Cancer Gene Ther.*, vol. 12, no. 3, pp. 257–267, 2005.

[73] F. Leenders, K. Mopert, A. Schmiedeknecht, A. Santel, F. Czauderna, M. Aleku, S. Penschuck, S. Dames, M. Sternberger, T. Rohl, A. Wellmann, W. Arnold, K. Giese, J. Kaufmann, and A. Klippel, "PKN3 is required for malignant prostate cell growth downstream of activated PI 3-kinase," *Embo J.*, vol. 23, no. 16, pp. 3303–3313, 2004.

[74] S. Clejan, K. O'Connor, and N. Rosensweig, "Tri-dimensional prostate cell cultures in simulated microgravity and induced changes in lipid second messengers and signal transduction," *J. Cell. Mol. Med.*, vol. 5, no. 1, pp.

60–73, 2001.

[75] C. Yates, C. R. Shepard, G. Papworth, A. Dash, D. B. Stolz, S. Tannenbaum, L. Griffith, and A. Wells, "Novel three-dimensional organotypic liver bioreactor to directly visualize early events in metastatic progression," *Adv. Cancer Res. Vol 97*, vol. 97, p. 225–+, 2007.

[76] H. Song, O. David, S. Clejan, C. L. Giordano, H. Pappas-Lebeau, L. Xu, and K. C. O'Connor, "Spatial composition of prostate cancer spheroids in mixed and static cultures," *Tissue Eng.*, vol. 10, no. 7–8, pp. 1266–1276, 2004.

[77] L. A. Gurski, A. K. Jha, C. Zhang, X. Q. Jia, and M. C. Farach-Carson, "Hyaluronic acid-based hydrogels as 3D matrices for in vitro evaluation of chemotherapeutic drugs using poorly adherent prostate cancer cells," *Biomaterials*, vol. 30, no. 30, pp. 6076–6085, 2009.

[78] T. Tsunoda, B. Furusato, Y. Takashima, S. Ravulapalli, A. Dobi, S. Srivastava, D. G. McLeod, I. A. Sesterhenn, D. K. Ornstein, and S. Shirasawa, "The Increased Expression of Periostin During Early Stages of Prostate Cancer and Advanced Stages of Cancer Stroma," *Prostate*, vol. 69, no. 13, pp. 1398–1403, 2009.

[79] O. Hartman, C. Zhang, E. L. Adams, M. C. Farach-Carson, N. J. Petrelli, B. D. Chase, and J. F. Rabolt, "Microfabricated Electrospun Collagen Membranes for 3-D Cancer Models and Drug Screening Applications," *Biomacromolecules*, vol. 10, no. 8, pp. 2019–2032, Aug. 2009.

[80] J. H. Chu, S. Yu, S. W. Hayward, and F. L. Chan, "Development of a Three-Dimensional Culture Model of Prostatic Epithelial Cells and Its Use for the Study of Epithelial-Mesenchymal Transition and Inhibition of PI3K Pathway in Prostate Cancer," *Prostate*, vol. 69, no. 4, pp. 428–442, 2009.

[81] R. A. Rowehl, H. Crawford, A. Dufour, J. Ju, and G. I. Botchkina, "Genomic Analysis of Prostate Cancer Stem Cells Isolated from a Highly Metastatic Cell Line," *Cancer Genomics Proteomics*, vol. 5, no. 6, pp. 301–310, 2008.

[82] A. Y. Hsiao, Y. Torisawa, Y.-C. Tung, S. Sud, R. S. Taichman, K. J. Pienta, and S. Takayama, "Microfluidic system for formation of PC-3 prostate cancer co-culture spheroids," *Biomaterials*, vol. 30, no. 16, pp. 3020–3027, 2009.

[83] E. Sahai, "Mechanisms of cancer cell invasion," *Curr. Opin. Genet. Dev.*, vol. 15, no. 1, pp. 87–96, Feb. 2005.

[84] N. Zahir and V. M. Weaver, "Death in the third dimension: apoptosis regulation and tissue architecture," *Curr. Opin. Genet. Dev.*, vol. 14, no. 1, pp. 71–80, Feb. 2004.

[85] A. Sivaraman, J. K. Leach, S. Townsend, T. Iida, B. J. Hogan, D. B. Stolz, R. Fry, L. D. Samson, S. R. Tannenbaum, and L. G. Griffith, "A microscale in vitro physiological model of the liver: Predictive screens for drug metabolism and enzyme induction," *Curr. Drug Metab.*, vol. 6, no. 6, pp. 569–591, 2005.

[86] A. Nyga, U. Cheema, and M. Loizidou, "3D tumour models: novel in vitro approaches to cancer studies.," *J. Cell Commun. Signal.*, vol. 5, no. 3, pp. 239–48, Aug. 2011.

[87] E. Burdett, F. K. Kasper, A. G. Mikos, and J. A. Ludwig, "Engineering Tumors: A Tissue Engineering Perspective in Cancer Biology," *Tissue Eng. Part B-Reviews*, vol. 16, no. 3, pp. 351–359, Jun. 2010.

[88] P. DelNero, Y. H. Song, and C. Fischbach, "Microengineered tumor models: insights & opportunities from a physical sciences-oncology perspective.," *Biomed. Microdevices*, vol. 15, no. 4, pp. 583–93, Aug. 2013.

[89] K. M. Yamada and E. Cukierman, "Modeling tissue morphogenesis and cancer in 3D.," *Cell*, vol. 130, no. 4, pp. 601–10, Aug. 2007.

[90] D. W. Hutmacher, D. Loessner, S. Rizzi, D. L. Kaplan, D. J. Mooney, and J. a Clements, "Can tissue engineering concepts advance tumor biology research?," *Trends Biotechnol.*, vol. 28, no. 3, pp. 125–33, Mar. 2010.

[91] D. W. Hutmacher, R. E. Horch, D. Loessner, S. Rizzi, S. Sieh, J. C. Reichert, J. A. Clements, J. P. Beier, A. Arkudas, O. Bleiziffer, and U. Kneser, "Translating tissue engineering technology platforms into cancer research," *J. Cell. Mol. Med.*, vol. 13, no. 8A, pp. 1417–1427, 2009.

[92] C. Ricci, L. Moroni, and S. Danti, "Cancer tissue engineering — new perspectives in understanding the biology of solid tumours — a critical review," *OA Tissue Eng.*, vol. 1, no. 1, pp. 1–7, 2013.

[93] J. O. Drife, "Breast Development in Puberty," *Ann. N. Y. Acad. Sci.*, vol. 464, no. 1, pp. 58–65, 1986.

[94] T. W. Ridky, J. M. Chow, D. J. Wong, and P. A. Khavari, "Invasive three-dimensional organotypic neoplasia from multiple normal human epithelia," *Nat. Med.*, vol. 16, no. 12, pp. 1450-U137, 2010.

[95] C. L. Li, T. Tian, K. J. Nan, N. Zhao, Y. H. Guo, J. Cui, J. Wang, and W. G. Zhang, "Survival advantages of multicellular spheroids vs. monolayers of HepG2 cells in vitro," *Oncol. Rep.*, vol. 20, no. 6, pp. 1465–1471, 2008.

[96] V. Chopra, T. V Dinh, and E. V Hannigan, "Three-dimensional endothelial-tumor epithelial cell interactions in human cervical cancers," *Vitr. Cell. Dev.*

Biol., vol. 33, no. 6, pp. 432–442, 1997.

[97]   L. A. Morford, E. R. Boghaert, W. H. Brooks, and T. L. Roszman, "Insulin-like growth factors (IGF) enhance three-dimensional (3D) growth of human glioblastomas," *Cancer Lett.*, vol. 115, no. 1, pp. 81–90, May 1997.

[98]   S. Bellusci, G. Moens, and G. Gaudino, "Creation of an hepatocyte growth factor/scatter factor autocrine loop in carcinoma cells induces invasive properties associated with increased tumorigenicity.," *Oncogene*, vol. 9, no. 4, pp. 1091–9, Apr. 1994.

[99]   S. Ghosh, G. C. Spagnoli, I. Martin, S. Ploegert, P. Demougin, M. Heberer, and A. Reschner, "Three-dimensional culture of melanoma cells profoundly affects gene expression profile: A high density oligonucleotide array study," *J. Cell. Physiol.*, vol. 204, no. 2, pp. 522–531, 2005.

[100] A. L. Kung, "Practices and pitfalls of mouse cancer models in drug discovery," in *Advances in Cancer Research, Vol 96*, vol. 96, San Diego: Elsevier Academic Press Inc, 2007, pp. 191–212.

[101] F. Balkwill, K. A. Charles, and A. Mantovani, "Smoldering and polarized inflammation in the initiation and promotion of malignant disease," *Cancer Cell*, vol. 7, no. 3, pp. 211–217, 2005.

[102] M. Kawamura, M. Gika, T. Abiko, Y. Inoue, T. Oyama, Y. Izumi, H. Kobayashi, and K. Kobayashi, "Clinical evaluation of chemosensitivity testing for patients with unresectable non-small cell lung cancer (NSCLC) using collagen gel droplet embedded culture drug sensitivity test (CD-DST)," *Cancer Chemother. Pharmacol.*, vol. 59, no. 4, pp. 507–513, 2007.

[103] H. G. Kang, J. M. Jenabi, J. S. Zhang, N. Keshelava, H. Shimada, W. A. May, T. Ng, C. P. Reynolds, T. J. Triche, and P. H. B. Sorensen, "E-cadherin cell-cell adhesion in Ewing tumor cells mediates suppression of anoikis through activation of the ErbB4 tyrosine kinase," *Cancer Res.*, vol. 67, no. 7, pp. 3094–3105, 2007.

[104] L. R. Kelland, "'Of mice and men': values and liabilities of the athymic nude mouse model in anticancer drug development," *Eur. J. Cancer*, vol. 40, no. 6, pp. 827–836, 2004.

[105] T. Kubota, N. Sasano, O. Abe, I. Nakao, E. Kawamura, T. Saito, M. Endo, K. Kimura, H. Demura, H. Sasano, H. Nagura, N. Ogawa, and R. M. Hoffman, "Potential of the histoculture drug-response assay to contribute to cancer patient survival," *Clin. Cancer Res.*, vol. 1, no. 12, pp. 1537–1543, 1995.

[106] P. A. Khavari, "Modelling cancer in human skin tissue," *Nat. Rev. Cancer*,

vol. 6, no. 4, pp. 270–280, Apr. 2006.

[107] M.-J. Zheng, J. Wang, Y.-W. Chen, L. Xu, D.-D. Xue, W. Fu, Y.-F. Zhang, Q. Du, Y. Zhao, L.-J. Ling, Q. Ding, X.-A. Liu, X.-M. Zha, W. Zheng, T.-S. Xia, and S. Wang, "A novel mouse model of gastric cancer with human gastric microenvironment," *Cancer Lett.*, vol. 325, no. 1, pp. 108–115, Dec. 2012.

[108] C. J. Olsen, J. Moreira, E. M. Lukanidin, and N. S. Ambartsumian, "Human mammary fibroblasts stimulate invasion of breast cancer cells in a three-dimensional culture and increase stroma development in mouse xenografts.," *BMC Cancer*, vol. 10, p. 444, Jan. 2010.

[109] P. Reichen, A. Sonnenfeld, and P. Rudolf von Rohr, "Remote Plasma Device for Surface Modification at Atmospheric Pressure," *Plasma Process. Polym.*, vol. 6, no. S1, pp. S382–S386, Jun. 2009.

[110] R. a D'Sa, G. a Burke, and B. J. Meenan, "Lens epithelial cell response to atmospheric pressure plasma modified poly(methylmethacrylate) surfaces.," *J. Mater. Sci. Mater. Med.*, vol. 21, no. 5, pp. 1703–12, May 2010.

[111] K. H. Becker, K. H. Schoenbach, and J. G. Eden, "Microplasmas and applications," *J. Phys. D. Appl. Phys.*, vol. 39, no. 3, pp. R55–R70, Feb. 2006.

[112] V. Nehra, A. Kumar, and H. K. Dwivedi, "Atmospheric non-thermal plasma sources," *Int. J. Eng.*, vol. 2, no. 1, pp. 53–68, 2008.

[113] T. Ichiki, Y. Sugiyama, R. Taura, T. Koidesawa, and Y. Horiike, "Plasma applications for biochip technology," *Thin Solid Films*, vol. 435, no. 1–2, pp. 62–68, 2003.

[114] U. Kogelschatz, "Dielectric-barrier discharges: their history, discharge physics, and industrial applications," *Plasma Chem. plasma Process.*, vol. 23, no. 1, pp. 1–46, 2003.

[115] A. F. Stalder, G. Kulik, D. Sage, L. Barbieri, and P. Hoffmann, "A snake-based approach to accurate determination of both contact points and contact angles," *Colloids Surfaces A Physicochem. Eng. Asp.*, vol. 286, no. 1–3, pp. 92–103, 2006.

[116] C. Wang, Q. Hamid, J. Snyder, H. Ayan, and W. Sun, "Localized Surface Functionalization of Polycaprolactone with Atmospheric-Pressure Microplasma Jet," *Biomed. Phys. Eng. Express*, vol. 1, no. 2, p. 25002, 2015.

[117] R. Singhvi, a Kumar, G. P. Lopez, G. N. Stephanopoulos, D. I. Wang, G. M. Whitesides, and D. E. Ingber, "Engineering cell shape and function.," *Science*, vol. 264, no. 5159, pp. 696–698, 1994.

[118] D. F. Williams, "On the nature of biomaterials," *Biomaterials*, vol. 30, no. 30, pp. 5897–5909, 2009.

[119] A. Curtis and P. Clark, "The effects of topographic and mechanical properties of materials on cell behavior," *Crit. Rev. Biocompat.*, vol. 5, no. 4, pp. 343–362, 1990.

[120] K. Anselme, "Osteoblast adhesion on biomaterials," *Biomaterials*, vol. 21, no. 7. pp. 667–681, 2000.

[121] C. S. Chen, M. Mrksich, S. Huang, G. M. Whitesides, and D. E. Ingber, "Geometric control of cell life and death.," *Science*, vol. 276, no. 5317, pp. 1425–1428, 1997.

[122] M. M. Stevens and J. H. George, "Exploring and engineering the cell surface interface.," *Science*, vol. 310, no. 5751, pp. 1135–1138, 2005.

[123] L. Lu, K. Nyalakonda, L. Kam, R. Bizios, A. Göpferich, and A. G. Mikos, "Retinal pigment epithelial cell adhesion on novel micropatterned surfaces fabricated from synthetic biodegradable polymers," *Biomaterials*, vol. 22, no. 3, pp. 291–297, 2001.

[124] R. Michel, J. W. Lussi, G. Csucs, I. Reviakine, G. Danuser, B. Ketterer, J. a. Hubbell, M. Textor, and N. D. Spencer, "Selective molecular assembly patterning: A new approach to micro- and nanochemical patterning of surfaces for biological applications," *Langmuir*, vol. 18, no. 8, pp. 3281–3287, 2002.

[125] S. Britland, P. Clark, P. Connolly, and G. Moores, "Micropatterned substratum adhesiveness: a model for morphogenetic cues controlling cell behavior.," *Exp. Cell Res.*, vol. 198, no. 1, pp. 124–129, 1992.

[126] S. Ber, G. Torun Köse, and V. Hasirci, "Bone tissue engineering on patterned collagen films: An in vitro study," *Biomaterials*, vol. 26, no. 14, pp. 1977–1986, 2005.

[127] N. Patrito, C. McCague, P. R. Norton, and N. O. Petersen, "Spatially controlled cell adhesion via micropatterned surface modification of poly(dimethiylsiloxane)," *Langmuir*, vol. 23, no. 2, pp. 715–719, 2007.

[128] F. L. Yap and Y. Zhang, "Assembly of polystyrene microspheres and its application in cell micropatterning," *Biomaterials*, vol. 28, no. 14, pp. 2328–2338, 2007.

[129] J. L. Dewez, J. B. Lhoest, E. Detrait, V. Berger, C. C. Dupont-Gillain, L. M. Vincent, Y. J. Schneider, P. Bertrand, and P. G. Rouxhet, "Adhesion of mammalian cells to polymer surfaces: From physical chemistry of surfaces

to selective adhesion on defined patterns," in *Biomaterials*, 1998, vol. 19, no. 16, pp. 1441–1445.

[130] G. M. Whitesides, E. Ostuni, S. Takayama, X. Jiang, and D. E. Ingber, "Soft lithography in biology and biochemistry.," *Annu. Rev. Biomed. Eng.*, vol. 3, pp. 335–373, 2001.

[131] J. S. Miller, M. I. Béthencourt, M. Hahn, T. R. Lee, and J. L. West, "Laser-scanning lithography (LSL) for the soft lithographic patterning of cell-adhesive self-assembled monolayers," *Biotechnol. Bioeng.*, vol. 93, no. 6, pp. 1060–1068, 2006.

[132] R. J. Jackman, J. L. Wilbur, and G. M. Whitesides, "Fabrication of submicrometer features on curved substrates by microcontact printing.," *Science*, vol. 269, no. 5224, pp. 664–666, 1995.

[133] A. Offenhäusser, S. Böcker-Meffert, T. Decker, R. Helpenstein, P. Gasteier, J. Groll, M. M?ller, A. Reska, S. Sch?fer, P. Schulte, and A. Vogt-Eisele, "Microcontact printing of proteins for neuronal cell guidance," *Soft Matter*, vol. 3, no. 3, p. 290, 2007.

[134] E. Ostuni, R. G. Chapman, M. N. Liang, G. Meluleni, G. Pier, D. E. Ingber, and G. M. Whitesides, "Self-assembled monolayers that resist the adsorption of proteins and the adhesion of bacterial and mammalian cells," *Langmuir*, vol. 17, no. 20, pp. 6336–6343, 2001.

[135] C. Staii, C. Viesselmann, J. Ballweg, L. Shi, G. Y. Liu, J. C. Williams, E. W. Dent, S. N. Coppersmith, and M. a. Eriksson, "Positioning and guidance of neurons on gold surfaces by directed assembly of proteins using Atomic Force Microscopy," *Biomaterials*, vol. 30, no. 20, pp. 3397–3404, 2009.

[136] S. Choi and W. L. Murphy, "Multifunctional mixed SAMs that promote both cell adhesion and noncovalent DNA immobilization," *Langmuir*, vol. 24, no. 13, pp. 6873–6880, 2008.

[137] D. J. Odde and M. J. Renn, "Laser-guided direct writing for applications in biotechnology," *Trends Biotechnol.*, vol. 17, no. 10, pp. 385–389, 1999.

[138] P. Li, U. Bakowsky, F. Yu, C. Loehbach, F. Muecklich, and C. M. Lehr, "Laser ablation patterning by interference induces directional cell growth," *IEEE Trans. Nanobioscience*, vol. 2, no. 3, pp. 138–145, 2003.

[139] G. J. Bakeine, J. Ban, G. Grenci, A. Pozzato, S. D. Zilio, M. Prasciolu, L. Businaro, M. Tormen, and M. E. Ruaro, "Design, fabrication and evaluation of nanoscale surface topography as a tool in directing differentiation and organisation of embryonic stem-cell-derived neural precursors," *Microelectron. Eng.*, vol. 86, no. 4–6, pp. 1435–1438, 2009.

[140] L. Altomare and S. Fare', "Cells response to topographic and chemical micropatterns.," *J. Appl. Biomater. Biomech.*, vol. 6, no. 3, pp. 132–143, 2008.

[141] D. Falconnet, G. Csucs, H. Michelle Grandin, and M. Textor, "Surface engineering approaches to micropattern surfaces for cell-based assays," *Biomaterials*, vol. 27, no. 16. pp. 3044–3063, 2006.

[142] H. Hwang, G. Kang, J. H. Yeon, Y. Nam, and J.-K. Park, "Direct rapid prototyping of PDMS from a photomask film for micropatterning of biomolecules and cells.," *Lab Chip*, vol. 9, no. 1, pp. 167–170, 2009.

[143] D. Falconnet, A. Koenig, F. Assi, and M. Textor, "A combined photolithographic and molecular-assembly approach to produce functional micropatterns for applications in the biosciences," *Adv. Funct. Mater.*, vol. 14, no. 8, pp. 749–756, 2004.

[144] H.-W. Chien, T.-Y. Chang, and W.-B. Tsai, "Spatial control of cellular adhesion using photo-crosslinked micropatterned polyelectrolyte multilayer films.," *Biomaterials*, vol. 30, no. 12, pp. 2209–2218, 2009.

[145] A. Khademhosseini, G. Eng, J. Yeh, P. a. Kucharczyk, R. Langer, G. Vunjak-Novakovic, and M. Radisic, "Microfluidic patterning for fabrication of contractile cardiac organoids," *Biomed. Microdevices*, vol. 9, no. 2, pp. 149–157, 2007.

[146] K. Itoga, M. Yamato, J. Kobayashi, A. Kikuchi, and T. Okano, "Cell micropatterning using photopolymerization with a liquid crystal device commercial projector," *Biomaterials*, vol. 25, no. 11, pp. 2047–2053, 2004.

[147] S. Alom Ruiz and C. S. Chen, "Microcontact printing: A tool to pattern," *Soft Matter*, vol. 3, no. 2. p. 168, 2007.

[148] K. B. Lee, Y. Kim, and I. S. Choi, "Pattern Generation of Cells on a Polymeric Surface Using Surface Functionalization and Microcontact Printing," *Bull. Korean Chem. Soc.*, vol. 24, no. 2, pp. 161–162, Feb. 2003.

[149] I. Beaulieu, M. Geissler, and J. Mauzeroll, "Oxygen plasma treatment of polystyrene and zeonor: Substrates for adhesion of patterned cells," *Langmuir*, vol. 25, no. 12, pp. 7169–7176, 2009.

[150] Q. Cheng, S. Li, and K. Komvopoulos, "Plasma-assisted surface chemical patterning for single-cell culture," *Biomaterials*, vol. 30, no. 25, pp. 4203–4210, 2009.

[151] M. Morra and C. Cassinelli, "Cell Adhesion Micropatterning by Plasma Treatment of Alginate Coated Surfaces," *Plasmas Polym.*, vol. 7, no. 2, pp.

89–101, Jun. 2002.

[152] J. P. Frimat, H. Menne, A. Michels, S. Kittel, R. Kettler, S. Borgmann, J. Franzke, and J. West, "Plasma stencilling methods for cell patterning," *Anal. Bioanal. Chem.*, vol. 395, no. 3, pp. 601–609, 2009.

[153] a. Koutsospyros, S. M. Yin, C. Christodoulatos, and K. Becker, "Destruction of hydrocarbons in non-thermal, ambient-pressure, capillary discharge plasmas," *Int. J. Mass Spectrom.*, vol. 233, no. 1–3, pp. 305–315, 2004.

[154] M. Miclea, K. Kunze, and J. Franzke, "Decomposition of Halogenated Molecules in a Micro-structured Electrode Glow Discharge at Atmospheric Pressure," *Proc. 8th Int. Symp. High Press. Low Temp. Plasma Chem.*, pp. 2–5, 2002.

[155] F. Brétagnol, O. Kylián, M. Hasiwa, L. Ceriotti, H. Rauscher, G. Ceccone, D. Gilliland, P. Colpo, and F. Rossi, "Micro-patterned surfaces based on plasma modification of PEO-like coating for biological applications," *Sensors Actuators, B Chem.*, vol. 123, no. 1, pp. 283–292, 2007.

[156] F.-Z. Cui, Y.-P. Jiao, and I.-S. Lee, "Functionalization of Polymer Surface for Nerve Repair," *J. Photopolym. Sci. Technol.*, vol. 21, no. 2, pp. 231–244, 2008.

[157] S.-J. Park, C. J. Wagner, C. M. Herring, and J. G. Eden, "Flexible microdischarge arrays: Metal/polymer devices," *Appl. Phys. Lett.*, vol. 77, no. 2, p. 199, Jul. 2000.

[158] D. Staack, B. Farouk, A. Gutsol, and A. Fridman, "Characterization of a dc atmospheric pressure normal glow discharge," *Plasma Sources Science and Technology*, vol. 14, no. 4. pp. 700–711, 2005.

[159] Z. Yang, H. Shirai, T. Kobayashi, and Y. Hasegawa, "Synthesis of Si nanocones using rf microplasma at atmospheric pressure," *Thin Solid Films*, vol. 515, no. 9, pp. 4153–4158, 2007.

[160] M. Miclea, K. Kunze, J. Franzke, and K. Niemax, "Plasmas for lab-on-the-chip applications," *Spectrochim. Acta - Part B At. Spectrosc.*, vol. 57, no. 10, pp. 1585–1592, Oct. 2002.

[161] M. Laroussi and X. Lu, "Room-temperature atmospheric pressure plasma plume for biomedical applications," *Appl. Phys. Lett.*, vol. 87, no. 11, p. 3pp, 2005.

[162] Y. C. Hong and H. S. Uhm, "Microplasma jet at atmospheric pressure," *Appl. Phys. Lett.*, vol. 89, no. 22, p. 221504, 2006.

[163] E. Stoffels, a J. Flikweert, W. W. Stoffels, and G. M. W. Kroesen, "Plasma needle: a non-destructive atmospheric plasma source for fine surface treatment of (bio)materials," *Plasma Sources Science and Technology*, vol. 11, no. 4. pp. 383–388, 2002.

[164] X. Lu and M. Laroussi, "Dynamics of an atmospheric pressure plasma plume generated by submicrosecond voltage pulses," *J. Appl. Phys.*, vol. 100, no. 6, p. 63302, 2006.

[165] Multi-agency tissue engineering science interagency working group, "Advancing tissue science and engineering: a foundation for the future. A multi-agency strategic plan.," *Tissue Eng.*, vol. 13, no. 12, pp. 2825–2826, Dec. 2007.

[166] H. Ayan, G. Fridman, Y. Mukhin, a. Starikovskii, a. Fridman, G. Friedman, D. Staack, and a. Gutsol, "Application of nanosecond-pulsed dielectric barrier discharge on topographically non-uniform surfaces for biomedical treatment," *IEEE Int. Conf. Plasma Sci.*, 2009.

[167] H. Ayan, G. Fridman, A. F. Gutsol, V. N. Vasilets, A. Fridman, and G. Friedman, "Nanosecond-pulsed uniform dielectric-barrier discharge," *IEEE Trans. Plasma Sci.*, vol. 36, no. 2 PART 2, pp. 504–508, 2008.

[168] H. Ayan, E. D. Yildirim, D. D. Pappas, and W. Sun, "Development of a cold atmospheric pressure microplasma jet for freeform cell printing," *Appl. Phys. Lett.*, vol. 99, no. 11, p. 111502, 2011.

[169] C. Liu, "Effects of DBD plasma operating parameters on the polymer surface modification," *Surf. Coatings Technol.*, vol. 185, no. 2–3, pp. 311–320, Jul. 2004.

[170] V. Jokinen, P. Suvanto, and S. Franssila, "Oxygen and nitrogen plasma hydrophilization and hydrophobic recovery of polymers.," *Biomicrofluidics*, vol. 6, no. 1, pp. 16501–1650110, Mar. 2012.

[171] T. Murakami, S. Kuroda, and Z. Osawa, "Dynamics of Polymeric Solid Surfaces Treated with Oxygen Plasma: Effect of Aging Media after Plasma Treatment," *J. Colloid Interface Sci.*, vol. 202, no. 1, pp. 37–44, 1998.

[172] J. A. Ryan, "Evolution of Cell Culture Surfaces," *BioFiles*, pp. 8–11, 2008.

[173] L. Shor, S. Guceri, X. J. Wen, M. Gandhi, and W. Sun, "Fabrication of three-dimensional polycaprolactone/hydroxyapatite tissue scaffolds and osteoblast-scaffold interactions in vitro," *Biomaterials*, vol. 28, no. 35, pp. 5291–5297, 2007.

[174] F. Iza, S. H. Lee, and J. K. Lee, "Computer modeling of low-temperature

plasmas," in *Gas Discharges - Fundamentals & Applications*, vol. 661, no. 2, 2007, pp. 1–31.

[175] G. Park, H. Lee, G. Kim, and J. K. Lee, "Global model of He/O2 and Ar/O2 atmospheric pressure glow discharges," *Plasma Process. Polym.*, vol. 5, no. 6, pp. 569–576, 2008.

[176] G. Y. Park, Y. J. Hong, H. W. Lee, J. Y. Sim, and J. K. Lee, "A global model for the identification of the dominant reactions for atomic Oxygen in he/o2 atmospheric-pressure plasmas," *Plasma Process. Polym.*, vol. 7, no. 3–4, pp. 281–287, 2010.

[177] Q. Hamid, C. Wang, J. Snyder, S. Williams, Y. Liu, and W. Sun, "Maskless fabrication of cell-laden microfluidic chips with localized surface functionalization for the co-culture of cancer cells," *Biofabrication*, vol. 7, no. 1, p. 15012, 2015.

[178] T. Boland, T. Xu, B. Damon, and X. Cui, "Application of inkjet printing to tissue engineering," *Biotechnol J*, vol. 1, no. 9, pp. 910–917, 2006.

[179] M. E. Pepper, C. a Parzel, T. Burg, T. Boland, K. J. L. Burg, and R. E. Groff, "Design and implementation of a two-dimensional inkjet bioprinter," *Conf Proc IEEE Eng Med Biol Soc*, vol. 2009, pp. 6001–6005, Jan. 2009.

[180] S. Moon, S. K. Hasan, Y. S. Song, F. Xu, H. O. Keles, F. Manzur, S. Mikkilineni, J. W. Hong, J. Nagatomi, E. Haeggstrom, A. Khademhosseini, and U. Demirci, "Layer by layer three-dimensional tissue epitaxy by cell-laden hydrogel droplets," *Tissue Eng Part C Methods*, vol. 16, no. 1, pp. 157–166, 2010.

[181] F. Xu, J. Celli, I. Rizvi, S. Moon, T. Hasan, and U. Demirci, "A three-dimensional in vitro ovarian cancer coculture model using a high-throughput cell patterning platform," *Biotechnol J*, vol. 6, no. 2, pp. 204–212, 2011.

[182] I. Rizvi, J. Celli, and F. Xu, "Biologically relevant 3D tumor arrays: treatment response and the importance of stromal partners," in *SPIE …*, 2011, vol. 7886, pp. 788609–788614.

[183] M. Matsusaki, K. Sakaue, K. Kadowaki, and M. Akashi, "Three-Dimensional Human Tissue Chips Fabricated by Rapid and Automatic Inkjet Cell Printing," *Adv Heal. Mater*, 2012.

[184] L. E. Dickinson, C. Lutgebaucks, D. M. Lewis, and S. Gerecht, "Patterning microscale extracellular matrices to study endothelial and cancer cell interactions in vitro," *Lab Chip*, vol. 12, no. 21, pp. 4244–4248, 2012.

[185] Y. Zhao, T. Zhang, F. Lin, and W. Sun, "Controlled Cell Assembly for 3D

Tumor Model – A Preliminary Study," in *9th World Biomaterials Congress*, 2012, p. 1473.

[186] U. Haessler, Y. Kalinin, M. A. Swartz, and M. Wu, "An agarose-based microfluidic platform with a gradient buffer for 3D chemotaxis studies," *Biomed Microdevices*, vol. 11, no. 4, pp. 827–835, 2009.

[187] D. Kloss, M. Fischer, A. Rothermel, J. C. Simon, and A. a Robitzki, "Drug testing on 3D in vitro tissues trapped on a microcavity chip," *Lab Chip*, vol. 8, no. 6, pp. 879–884, Jun. 2008.

[188] K. E. Sung, N. Yang, C. Pehlke, P. J. Keely, K. W. Eliceiri, A. Friedl, and D. J. Beebe, "Transition to invasion in breast cancer: a microfluidic in vitro model enables examination of spatial and temporal effects.," *Integr. Biol. (Camb).*, vol. 3, no. 4, pp. 439–50, Apr. 2011.

[189] I. K. Zervantonakis, S. K. Hughes-Alford, J. L. Charest, J. S. Condeelis, F. B. Gertler, and R. D. Kamm, "Three-dimensional microfluidic model for tumor cell intravasation and endothelial barrier function," *Proc. Natl. Acad. Sci. U. S. A.*, vol. 109, no. 34, pp. 13515–13520, Aug. 2012.

[190] V. V Glinsky, M. E. Huflejt, G. V Glinsky, S. L. Deutscher, and T. P. Quinn, "Effects of Thomsen-Friedenreich antigen-specific peptide P-30 on beta-galactoside-mediated homotypic aggregation and adhesion to the endothelium of MDA-MB-435 human breast carcinoma cells," *Cancer Res*, vol. 60, no. 10, pp. 2584–2588, 2000.

[191] J. M. Kelm, N. E. Timmins, C. J. Brown, M. Fussenegger, and L. K. Nielsen, "Method for generation of homogeneous multicellular tumor spheroids applicable to a wide variety of cell types," *Biotechnol. Bioeng.*, vol. 83, no. 2, pp. 173–180, Jul. 2003.

[192] F. J. Wu, J. R. Friend, C. C. Hsiao, M. J. Zilliox, W. J. Ko, F. B. Cerra, and W. S. Hu, "Efficient assembly of rat hepatocyte spheroids for tissue engineering applications," *Biotechnol. Bioeng.*, vol. 50, no. 4, pp. 404–415, 1996.

[193] N. Koide, K. Sakaguchi, Y. Koide, K. Asano, M. Kawaguchi, H. Matsushima, T. Takenami, T. Shinji, M. Mori, and T. Tsuji, "Formation of multicellular spheroids composed of adult-rat hepatocytes in dishes with positively charged surfaces and under other nonadherent environments," *Exp. Cell Res.*, vol. 186, no. 2, pp. 227–235, 1990.

[194] G. H. Underhill, A. A. Chen, D. R. Albrecht, and S. N. Bhatia, "Assessment of hepatocellular function within PEG hydrogels," *Biomaterials*, vol. 28, pp. 256–270, 2007.

[195] C. Zilkens, T. Logters, B. Bittersohl, R. Krauspe, S. Lensing-Hohn, and M. Jager, "Spinning around or Stagnation - What Do Osteoblasts and Chondroblasts Really Like?," *Eur. J. Med. Res.*, vol. 15, no. 1, pp. 35–43, 2010.

[196] T. J. Goodwin, T. L. Prewett, D. A. Wolf, and G. F. Spaulding, "Reduced shear stress: a major component in the ability of mammalian tissues to form three-dimensional assemblies in simulated microgravity," *J Cell Biochem*, vol. 51, no. 3, pp. 301–311, 1993.

[197] A. D. Conger and M. C. Ziskin, "Growth of Mammalian Multicellular Tumor Spheroids," *Cancer Res.*, vol. 43, no. 2, pp. 556–560, 1983.

[198] J. Landry, J. P. Freyer, and R. M. Sutherland, "A Model for the Growth of Multicellular Spheroids," *Cell Tissue Kinet.*, vol. 15, no. 6, pp. 585–594, 1982.

[199] B. A. Teicher, "Acute and chronic in vivo therapeutic resistance," *Biochem Pharmacol*, vol. 77, no. 11, pp. 1665–1673, 2009.

[200] F. Hirschhaeuser, H. Menne, C. Dittfeld, J. West, W. Mueller-Klieser, and L. A. Kunz-Schughart, "Multicellular tumor spheroids: An underestimated tool is catching up again," *J. Biotechnol.*, vol. 148, no. 1, pp. 3–15, Jul. 2010.

[201] K. Hotary, E. Allen, P. Brooks, and N. Datta, "Membrane type I matrix metalloproteinase usurps tumor growth control imposed by the three-dimensional extracellular matrix," *Cell*, vol. 114, no. 1, pp. 33–45, Jul. 2003.

[202] W. Jiang and K. Harding, "Enhancement of wound tissue expansion and angiogenesis by matrix-embedded fibroblast (dermagraft), a role of hepatocyte growth factor/scatter factor.," *Int. J. Mol. Med.*, vol. 2, no. 2, pp. 203–210, Aug. 1998.

[203] K. Wolf, S. Alexander, V. Schacht, L. M. Coussens, U. H. von Andrian, J. van Rheenen, E. Deryugina, and P. Friedl, "Collagen-based cell migration models in vitro and in vivo.," *Semin. Cell Dev. Biol.*, vol. 20, no. 8, pp. 931–41, Oct. 2009.

[204] M. A. Wozniak and P. J. Keely, "Use of three-dimensional collagen gels to study mechanotransduction in T47D breast epithelial cells.," *Biol. Proced. Online*, vol. 7, pp. 144–61, Jan. 2005.

[205] N. L. Jeon, C. P. Huang, J. Lu, H. Seon, A. P. Lee, L. A. Flanagan, H. Y. Kim, and A. J. Putnam, "Engineering microscale cellular niches for three-dimensional multicellular co-cultures," *Lab Chip*, vol. 9, no. 12, pp. 1740–1748, 2009.

[206] K. E. Sung, G. Su, C. Pehlke, S. M. Trier, K. W. Eliceiri, P. J. Keely, A. Friedl, and D. J. Beebe, "Control of 3-dimensional collagen matrix polymerization for reproducible human mammary fibroblast cell culture in microfluidic devices," *Biomaterials*, vol. 30, no. 27, pp. 4833–4841, 2009.

[207] J. W. Nichol and A. Khademhosseini, "Modular tissue engineering: engineering biological tissues from the bottom up," *Soft Matter*, vol. 5, no. 7, pp. 1312–1319, 2009.

[208] M. Q. Zhang, F. M. Kievit, S. J. Florczyk, M. C. Leung, O. Veiseh, J. O. Park, and M. L. Disis, "Chitosan-alginate 3D scaffolds as a mimic of the glioma tumor microenvironment," *Biomaterials*, vol. 31, no. 22, pp. 5903–5910, Aug. 2010.

[209] T. J. Sill and H. A. von Recum, "Electrospinning: applications in drug delivery and tissue engineering," *Biomaterials*, vol. 29, no. 13, pp. 1989–2006, 2008.

[210] Q. Hamid and W. Sun, "Coaxial Electrospinning Biopolymer With Living Cells," in *ASME 2010 First Global Congress on NanoEngineering for Medicine and Biology*, 2010, pp. 167–172.

[211] Y. J. Kim, H. I. Bae, O. K. Kwon, and M. S. Choi, "Three-dimensional gastric cancer cell culture using nanofiber scaffold for chemosensitivity test," *Int. J. Biol. Macromol.*, vol. 45, no. 1, pp. 65–71, 2009.

[212] M. Vallet-Regí, M. Colilla, and B. González, "Medical applications of organic-inorganic hybrid materials within the field of silica-based bioceramics.," *Chem. Soc. Rev.*, vol. 40, no. 2, pp. 596–607, Feb. 2011.

[213] D. Mangindaan, W.-H. Kuo, Y.-L. Wang, and M.-J. Wang, "Experimental and Numerical Modeling of the Controllable Wettability Gradient on Poly(propylene) Created by SF6 Plasma," *Plasma Process. Polym.*, vol. 7, no. 9–10, pp. 754–765, Oct. 2010.

VITA

EDUCATION

Doctor of Philosophy   2016
Department of Mechanical Engineering and Mechanics, Drexel University, Philadelphia, PA, USA

Master of Science   2013
Department of Mechanical Engineering and Mechanics, Drexel University, Philadelphia, PA, USA

Bachelor of Engineering   2009
Department of Fine Chemical Engineering, Dalian University of Technology, Dalian, Liaoning, China

HONORS AND AWARDS

Dean's Fellowship   2009, 2010
College of Engineering, Drexel University, Philadelphia, PA, USA

Mechanical Engineering Award   2011
Department of Mechanical Engineering and Mechanics, Drexel University, Philadelphia, PA, USA

PUBLICATIONS

Patent
W. Sun, Q. Hamid, and **C. Wang**, "Methods of generating ultraviolet radiation, plasma- and ultraviolet - generating nozzles, printing systems, method of generating a substrate, and substrates fabricated according to the same," 2014, status: pending.

Book Chapter
Q. Hamid, **C. Wang**, J. Snyder, and Y. Zhao, "A Digital Microfabrication-Based System for the Fabrication of Cancerous Tissue Models," in Biofabrication: Micro- and Nano-fabrication, Printing, Patterning and Assemblies, Elsevier, 2013, pp. 167–182.

Indexed Journal and Conference Publications (selected 6 of 16)
C. Wang, Q. Hamid, J. Snyder, H. Ayan, and W. Sun, "Localized Surface Functionalization of Polycaprolactone with Atmospheric-Pressure Microplasma Jet", Biomedical Physics & Engineering Express, vol. 1, no. 2, p. 025002, 2015.

Q. Hamid, **C. Wang**, J. Snyder, S. Williams, Y. Liu, and W. Sun, "Maskless fabrication of cell-laden microfluidic chips with localized surface functionalization for the co-culture of cancer cells," Biofabrication, vol. 7, no. 1, p. 015012, 2015.

Q. Hamid, **C. Wang**, Y. Zhao, J. Snyder, and W. Sun, "A three-dimensional cell-laden microfluidic chip for in vitro drug metabolism detection," Biofabrication, vol. 6, p. 025008, 2014.

C. Wang, Z. Tang, Y. Zhao, R. Yao, L. Li, and W. Sun, "Three-dimensional in vitro cancer models: a short review," Biofabrication, vol. 6, p. 022001, 2014.

C. Wang, Q. Hamid, J. Snyder, H. Ayan, and W. Sun, "A novel automation system for microplasma surface patterning and biologics printing," in ASME/ISCIE 2012 International Symposium on Flexible Automation, 2012, p. 67.

C. Wang, Q. Hamid, and J. Snyder, "Development of a maskless microplasma surface patterning system for biologics printing," in Bioengineering Conference (NEBEC), 2012 38th Annual Northeast, 2012, pp. 111–112.